2013

Optical Investigation of Structural Phase Transitions in the Oxide Perovskites {KT}a$_{(1-x)}${N}b$_x${O}$_3$ and ({N}a$_{0.5}${B}i$_{0.5}$){T}i{O}$_3$}

Daniel Keith Jackson
Lehigh University

Optical Investigation of Structural Phase Transitions in the Oxide Perovskites $KTa_{(1-x)}Nb_xO_3$ and $(Na_{0.5}Bi_{0.5})TiO_3$

by

Daniel K. Jackson

A Dissertation
Presented to the Graduate Committee
of Lehigh University
in Candidacy for the Degree of
Doctor of Philosophy
in
Physics

Lehigh University
September, 2013

Approved and recommended for acceptance as a dissertation in partial fulfillment of the requirements for the degree of Doctor of Philosophy.

Daniel K. Jackson
Optical Investigation of Structural Phase Transitions in the Oxide Perovskites $KTa_{(1-x)}Nb_xO_3$ and $(Na_{0.5}Bi_{0.5})TiO_3$

Date

Prof. Jean Toulouse, Dissertation Director, Chair

Accepted Date

Committee Members

Prof. Volkmar Dierolf

Prof. Slava V. Rotkin

Prof. Ivan Biaggio

Prof. Matthew Dawber

0.1 Acknowledgements

I would like to thank my advisor, Dr. Jean Toulouse, for his thoughtfulness, patience and understanding as I progressed through this graduate experience. Without his essential advice to stick to the simple physical principals, I would have gotten lost in the forest. I am grateful for the financial support provided from Dr. Dwight Viehland through the National Science Foundations World Materials Network Grant. I am very grateful to Dr. Radha Pattnaik for his invaluable advice and assistence in setting up my experiments and helping to explain the many vagarities of perovskite world. My many conversations with Drs. M.J. Stavola, W.B. Fowler, I. Biaggio, and S.V. Rotkin have been most helpful and greatly appreciated. I wish to thank Drs. L.A. Boatner, A.J. Agranat and H. Luo for providing the various crystal samples. I also wish to thank the DOE and the National Science Foundation for their funding at various points in these projects.

I am grateful to all of the graduate students who have made my time a Lehigh a great adventure. Ling Cai has been particularly helpful in the many discussions we have had about relaxor ferroelectrics. I am grateful to Dr. John McElhenny for his useful discussions, taste in music, superior demonstrations of quality research, and above all his timely sense of humor. Drs. Ruth Malenda and Jon Poplowski were instrumental as study partners during the qualifiers. I cannot thank you two enough! I am also grateful to Dr. Francis Ndi, Massooma Pirbai, Corey Lafontaine, Josh Jones, Joe Zelinski, Rich White, and Wayne Ferencin for their many conversations that helped keep me sane.

This would not have been possible without the fantastic undergraduate experience I had at the University of Buffalo. I am indebted to Drs. A. Markelz, F. M. Gasparini, J. Cerne, J. Ho, B.A. Weinstein, B. McCombe, and S. Sen who taught me the joy of physics. I am also very grateful to all the other undergraduate students who shared the journey with me: K. Kirshenbaum, Caleb Carswell, Matt Dininno, and Cheryl Bell. In particular, I would like to thank my REU advisor, Dr. James Gole of Georgia Tech, for his invaluable lesson that when all is said and done, you just have to laugh about it. And if no one is laughing, try another joke.

I would like to thank my family for their love and support. My sisters, Erica and Ianthe, I love you both so much and I thank you for your support and encouragement. From my extended family, I am so grateful to Aunt Ev and Uncle Hugh, Aunt Lil, Uncle Andy, Uncle Larry and Aunt Blanche, you have all shown me such support and respect that I will never forget. Joe, you taught me preserverence, patience and the good that can be found in every person and situation. Mom, I owe you everything.

Lastly I would like to thank my dearest Francisca Donato. With you I am not alone, and my soul is whole.

Contents

List of Tables

List of Figures

Abstract

This thesis studies static and dynamic optical effects through the phase transitions of two perovskite materials, potassium tantalate niobate (KTN) and sodium bismuth titanate (NBT). Multiple experimental techniques are utilized to more thoroughly understand the nature of the phase transitions and determine the various contributions to the transitions.

In the first part, the temperature dependence of the birefringence of three different potassium tantalate niobate, or KTN, crystals is examined upon approaching the phase transition from cubic to tetragonal. This birefringence, which is in violation of crystalline symmetry conditions, is caused by the strain originating from the difference in unit cell size of the end materials, $KNbO_3$ and $KTaO_3$. This strain is either a gradient or a modulation due to the growth striations in the material, and diffraction is observed from the volume phase gratings via the difference in refractive indices. Upon approaching the phase transition, the birefringence displays rapid temperature dependence due to the formation of polar nano-domains which are preferentially oriented due to interaction with the striations. The variation of the birefringence with temperature is reported and discussed in the context of the existing literature. A sample of $K_{0.977}Li_{0.003}Ta_{0.845}Nb_{0.155}O_3$ or KLTN15.5 with well defined striations, $KTa_{0.73}Nb_{0.27}O_3$or KTN27) with no well defined striations and a sample of KLTN36 doped with copper and vanadium and diffuse striations are examined with respect to their optical behaviors in the cubic paraelectric phase.

In the second part, Raman spectroscopic measurements of sodium bismuth titanate ($Na_{0.5}Bi_{0.5}TiO_3$ or NBT) were carried out upon cooling from 1000 K to 80 K to study its two phase transitions. Full spectral deconvolution was performed, comparing the results from several fitting models, with a particular emphasis on the evolution of the central peak and low frequency phonon modes. The central intensity profile is found to be composed of two well-defined Lorentzian peaks, the temperature dependence of which suggests the presence of fluctuations in M-point and R-point rotations of the oxygen octahedra as well as fluctuations in cation displacements related to polar nano-domains. The temperature behavior of both

central peaks is discussed in relation to the (tilting or shifting) transition behavior in similar perovskite systems. The four observed low frequency phonon modes indicate a different symmetry assignment than the commonly assigned R3c for the low temperature phase.

Chapter 1

Background and general properties

1.1 Perovskite structure and doping

The perovskite structure is a label applied to materials with the same chemical structure as $CaTiO_3$ and are named in honor of the Russian mineralogist Count Lev Alekseevich Perovski[7]. The basic perovskite chemical formula shown in figures 1.1(a) and 1.1(b) is ABX_3, where X represents the anion on the faces of the cubic unit cell, A is a cation at the corners of the cell, and B is a cation at the center of the unit cell. Typical simple perovskites include the end materials of potassium tantalate niobate or KTN: $KTaO_3$ and $KNbO_3$, close relatives of sodium bismuth titanate or NBT: $SrTiO_3$, $BaTiO_3$, and $PbTiO_3$, and non-oxide materials such as $RbCaF_3$ and $KMnF_3$. By substitutionally doping and combining these basic materials, novel properties can be developed which are useful for both industrial applications and scientific understanding. Substitutions are often noted as $A(B_{(1-x)}B_x)X_3$ or $(A_{(1-x)}A_x)BX_3$ depending on whether the A-site or B-site cations are replaced. The end materials are studied for their characteristic behaviors which inform the understanding of the resulting mixed systems.

In the materials examined in this thesis, the anion oxygens are linked in a relatively rigid, corner sharing octahedron arrangement around the B-site cation[8, 9]. The KTN unit cell is illustrated in figure 1.1(a) with the Ta atom positioned its equilibrium site in the center of the unit cell, but the Nb and Li dopant atoms are known to be off center from their sites in one of the equivalent 8 <111>[10] or 6 <100>[11] directions respectively, resulting in a permanent, local electric dipole moment. These local dipoles can be dynamically reoriented in the presence of a external applied electric field. There is net charge neutrality in the KTN unit cell as the Ta^{5+} and Nb^{5+} atoms are isovalent, as are the K^{1+} and Li^{1+} atoms. The concentration of Nb and Li are randomly distributed and therefore not stoichiometric, potentially resulting in localized regions of differing concentration. The end materials, $KTaO_3$ [12] and $KNbO_3$[13], have similar lattice parameters at high temperature, 4.02 Åversus 3.99 Årespectively, a necessary condition for the formation of a stable solid solution[14]. X-Ray results for KTN samples with varying amounts of Nb show an increase in the average lattice parameter with increasing Nb concentration[15], indicating that local concentration differences may result in local strain. The purpose of mixing $KTaO_3$ and $KNbO_3$ into KTN is to create a new material that combines properties of both constituents[14]. $KTaO_3$ is cubic at all temperatures[16] with a large dielectric constant, but $KNbO_3$ has three phase transitions starting near 700 K[17]. Combining these two materials results in a crystal where the phase transition temperature can be adjusted with specific concentrations of[18].

In comparison, NBT has aliovalent Na^{1+} and Bi^{3+} atoms substituting on the A-site, resulting in an internal local dipole. In general the Na/Bi substitution is understood to be stoichiometric and variations in local concentrations have not yet been conclusively observed in single crystals despite many efforts to do so[19–24]. Similar to the Nb^{5+} and Li^{1+} atoms in KTN, all of the cations in NBT have been observed to be off-center from their equilibrium sites in neutron diffraction experiments[19]. The Ti^{4+} is assumed to occupy the same 8 <111> positions as Nb due to the hybridization of the electronic states between the Ti and the 2p states of the oxygen atoms[25] as in $BaTiO_3$. The Na and Bi atoms may have more freedom to move due to their small ionic sizes[26] and therefore may have a more

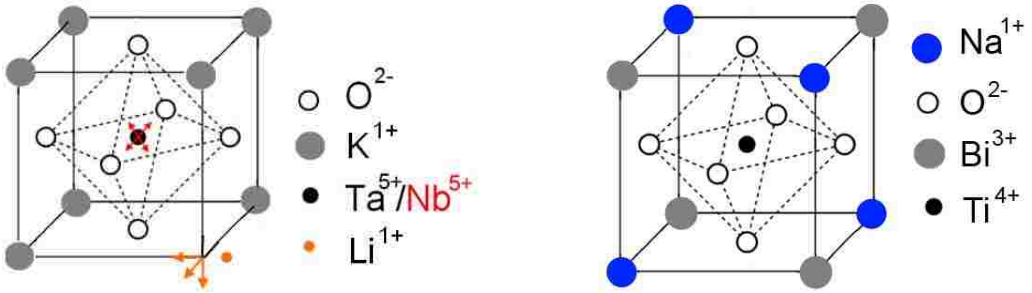

(a) KLTN Unit Cell (b) NBT Unit Cell

Figure 1.1: Perovskite unit cells with cation displacement shown.

spherical displacement similar to Pb relaxors[27]. The mobility of the Na atom has been demonstrated in NMR where the second moment exhibits a temperature dependence[28]. Recent theoretical work on similar multiferroic materials suggests that the Bi atom may be further off center than the Na[29, 30], but this has not been experimentally confirmed. One advantage of Raman spectroscopy is its ability to detect atomic displacements through their dynamics.

1.2 Applications of Perovskites

Perovskites are widely used in a wide variety of industrial applications including capacitors, transducers, modulators, and computer memory [8, 31]. KTN was originally identified as a promising candidate for electro-optic modulation, but was rejected due to the presence of both space charge fields[3], which create strong, internal electric fields that are difficult to remove without thermal treatment, and striations which are planar concentrational modulations formed during crystal growth[32, 33]. Nb concentration gradients in flux grown crystals[18] and striations in Top Seeded Solution Grown (TSSG)[34] materials are unavoidable consequences of the growth process for mixed materials due to temperature fluctuations in the growth melt[35]. Modifications of the crystal growth technique have been attempted to reduce the magnitude of striations[15, 18, 34] or, alternatively, to make them more prominent

and uniform[36]. Recently there has been a renewed interest in Li doped KTN as the Li allows the space charge field to reorient more easily[36]. Potential new applications include Bragg reflectors and transmission phase gratings permanently formed into the as-grown Li doped KTN crystal. KTN has recently been developed into new applications including beam scanners[37], optical waveguides[38], and vari-focal lenses[39].

Many perovskite materials are also piezoelectric, a term referring to the mechanical distortion resulting from the application of an electrical field. Doped ceramics and solid solutions of NBT have an electro-mechanical d_{33} coefficient ranging from 125 to 2000 pC/N [40, 41], while the single crystal ones are approximately 65 pC/N[42]. It is therefore a promising material for transducer and actuator applications as this higher end value is close to that of the commonly used relaxor PZN-PT[43]. NBT has also been suggested as an environmentally friendly replacement to the commonly used lead based relaxors since Na, Bi and Ti are all non-toxic elements.

1.3 Phase Transitions

A crystal is a condensed matter material whose atoms are arranged in a periodic array or lattice[44]. There are 14 three dimensional Bravais lattices which are used to describe an infinite array of atoms where each atom of a given type has the same environment regardless of its position in the lattice[45]. There are four Bravais lattices of interest for this report: cubic, tetragonal, monoclinic and rhombohedral, as shown in figure 1.2.

A 3-dimensional point group is a group of symmetry operators such as rotations, inversions, translations and glide planes that act on a site in the lattice and keep invariant all distances and angles with respect to that site, or point. By associating each point of a Bravais lattice with a point group, it is possible to define the semi-direct product as space groups. There are 230 possible space groups that are used to characterize the structural phases of crystal systems. A primitive unit cell

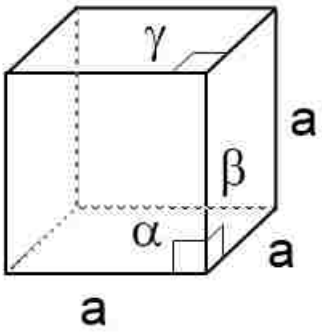

(a) Cubic Phase: $\alpha = \beta = \gamma = 90°$

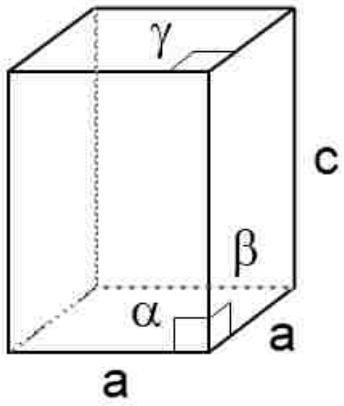

(b) Tetragonal Phase: $\alpha = \beta = \gamma = 90°$

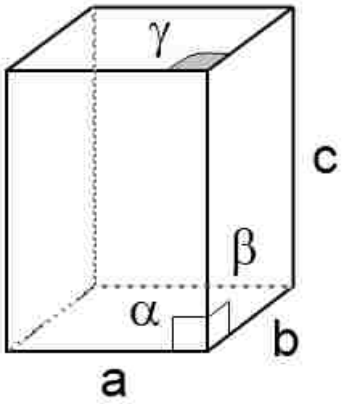

(c) Monoclinic Phase: $\alpha = \beta = 90°$,$\gamma \neq 90°$

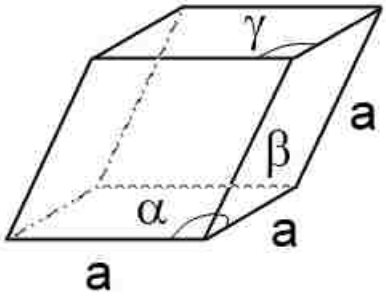

(d) Rhombohedral Phase: $\alpha = \beta = \gamma \neq 90°$

Figure 1.2: Bravais lattices referenced in this report.

is defined as a minimum volume parallelepiped that contains a single lattice point and through suitable translations fills all space without voids or overlap[45]. This parallelepiped also contains the complete molecular formula. This primitive unit cell can be chosen so that it has the same symmetry characteristics of a space group, which is how the unit cells in KTN and NBT are defined. A phase transition in a crystal involves collective re-orientation or displacement of atoms that reduces the

symmetry of the crystal to a lower symmetry space group[46]. Many observable physical properties change during phase transitions between different space groups, and these properties are used to positively identify and characterize the crystal morphology. The physical properties that are most commonly observed are spontaneous polarization and structural distortion. Ferroelectric (FE) and antiferroelectric (AFE) transitions involve the appearance of spontaneous polarization that is long range or anti-polar respectively. Anti-polar refers to oppositely aligned local dipoles with a zero net polarization[8]. Ferrodistortive (FD) transitions involve a change in dimension as illustrated by the difference in unit cell size of cubic and tetragonal systems in figures 1.2(a) and 1.2(b). A FD transition does not change the number of unit cells, as illustrated for a $KTaO_3$ unit cell in figure1.3(a), and thus translational symmetry is preserved. By contrast, antiferrodistortive (AFD) transitions do increase by an integer multiple of unit cells, i.e. z'=nz where n is an integer and so translational invariance is modified but still present[46]. Examples of AFD transitions are shown in figures 1.3(b) and 1.3(c) where the unit cell has doubled as a result of rotation of anion octahedra. The red diamond in figure 1.3(b) indicates the new unit cell whose principal axes have rotated by 90 degrees. The rotations are described in the Glazer notation as $a^0a^0c^+$ for M-point rotation and $a^-a^-a^-$[47] for R-point rotation, where the $^+$, $^-$ and ^{0} designate in-phase, out-of-phase and no rotation respectively. In-phase refers to a column of octahedra rotating together, while out-of-phase indicates that each individual octahedron is rotated in a direction opposite to its neighbors. The labels M and R indicate the locations in Brillouin zone of a simple cubic lattice[44] where Bragg peaks occur in the inelastic neutron scattering spectrum that are known to be correlated with octahedral rotations[48]. This notation is symbolic only, with the assignment of **a**, **b** and **c** indicating only relative differences in rotation. Therefore **aac** indicates that the rotation is the same along the [010] and [001] axes, but a different rotation angle along [100] axis. **aaa** indicates all axes have the same rotation magnitude.

A domain refers to a specific set of adjacent unit cells that have the same space group oriented together along one of the principal axes associated with that group[46]. Domains can range in size from nanometers to encompassing the entire

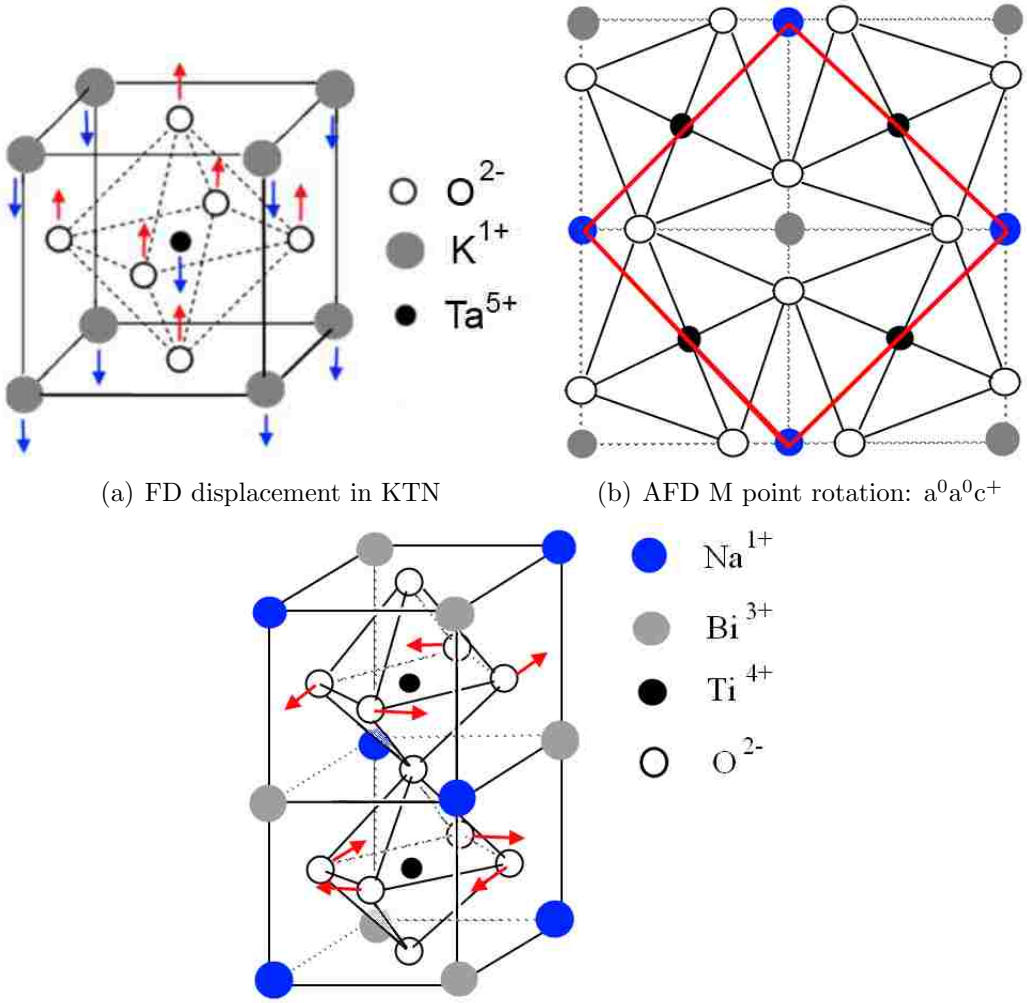

(a) FD displacement in KTN

(b) AFD M point rotation: $a^0a^0c^+$

(c) AFD R point rotation: $a^-a^-a^-$

Figure 1.3: Examples of ferrodistortive and anti-ferrodistortive transitions

sample. Boundaries between domains are referred to as domain walls. A polar nano region (PNR) refers to a nanometer sized polar domain that is short lived, dynamic in orientation, and easily reorientable while a polar nano domain (PND) refers to a PNR that has become static or equivalently frozen into a single orientation. Elastic, non polar domains are often referred to as chemically ordered regions or COR's or CNR's if they are nanometer in size[27].

Substitution, displacement or removal of one of the atoms in a lattice is known as a defect[49]. When the concentration of defects exceeds 0.1-2%, the material is often referred to as a dilute solid solution while concentrations above 2% are called solid solutions or alloys. Solid solutions typically have an average space group and local distortions due to defects have either identical or lower symmetry space groups[50]. The Nb,Li, Cu and V atoms in KTN can be considered substitutional defects in low concentration. Annealing an oxide sample in a reducing vacuum environment is known to strongly increase the number of oxygen vacancies, and potentially vacancies of other elements[49]. The vacancy concentration of any element can be easily calculated if the enthalpy of formation for that atomic component is known[49]. Annealing to 1000 K results in oxygen vacancy concentrations of one part billion in titanates such as $BaTiO_3$ and $SrTiO_3$, but the enthalpy of formation is not known in NBT and thus cannot be used to estimate any vacancy population. A key indicator of vacancies is the presence of Gaussian peaks in the absorption spectrum[51], which can be confirmed by theoretical calculations as in $BaTiO_3$[52] if the space group of the material is known.

Phenomenologically, a phase transition can be characterized by the appearance of a specific property or parameter below the transition that did not exist above the transition[8]. This parameter is referred to as the order parameter and can be remnant polarization due to the collective effects of dipole as in KTN, or the rotation angle of a molecular constituent that causes local strain as in NBT. An example of the expansion of the free energy in a phenomenological Landau-Devonshire formalism in the cubic $Pm\bar{3}m$ phase of KTN is as follows[53]:

$$
\begin{aligned}
G = G_0 &+ \frac{1}{2}A(X)(T - T_c(X))((P_x)^2 + (P_y)^2 + (P_z)^2) \\
&+ \frac{B_1}{4}((P_x)^4 + (P_y)^4 + (P_z)^4) \\
&+ \frac{B_2}{4}((P_x)^2(P_y)^2 + (P_x)^2(P_z)^2 + (P_y)^2(P_x)^2) \\
&+ \frac{C_1}{6}((P_x)^6 + (P_y)^6 + (P_z)^6) \\
&+ \frac{C_1}{6}((P_x)^4((P_y)^2 + (P_z)^2) + (P_y)^4((P_x)^2 + (P_z)^2) + (P_z)^4((P_x)^2 + (P_y)^2)) \\
&+ \frac{C_3}{6}(P_x)^2(P_y)^2(P_z)^2)
\end{aligned}
\tag{1.1}
$$

The P's indicate polarization, but Q or η could be used equivalently to indicate generalized strain as in NBT or some other order parameter for other systems.

Two general classes of structural transitions are first and second order transitions, differentiated on the basis of whether the transition is discontinuous or continuous. A first order transition has negative B_i values and the order parameter can be observed to have abrupt changes as a function of temperature as shown in figure 1.4(a)(ii). The free energy potential as shown in figure 1.4(a)(i) has multiple potential wells above the transition temperature, T_c, resulting in many possible local minima. This allows the system to have a disordered character. Lastly the reciprocal permittivity at constant stress, X, and temperature, T, exhibits a discontinuous jump as in figure 1.4(a)(iii).

The second order transition has positive B_i values and can be observed as continuous changes in the polarization in KTN[54] similar to the example shown in figure 1.4(b)(ii). This transition is characterized phenomenologically by a single well energy potential at the phase transition temperature as shown in figure 1.4(b)(i). The double well below T_c represents the two equivalent polarization directions that the system can transition into. The reciprocal permittivity goes to zero at T_c in figure 1.4(b)(iii), and critical behavior such as critical opalescence occurs at the transition. Away from T_c, κ follows the linear Curie-Weiss law as a function of temperature.

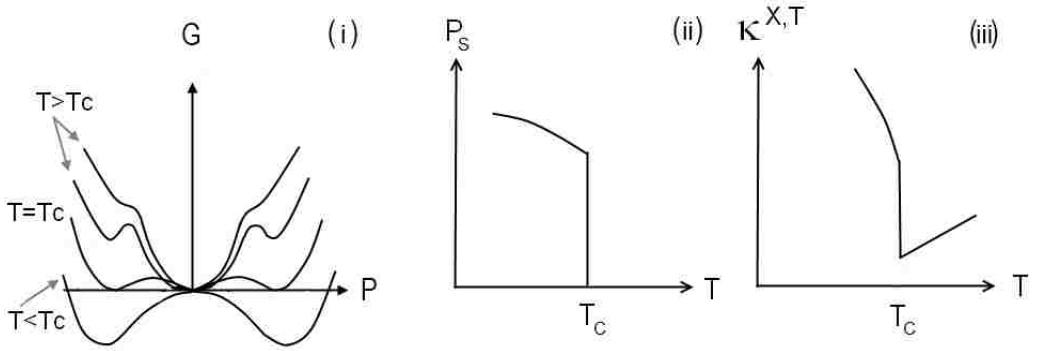

(a) First order transitions

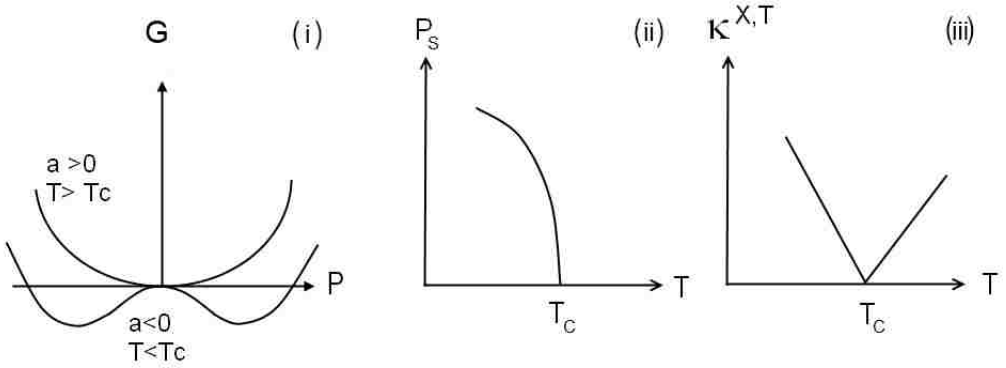

(b) Second order transitions

Figure 1.4: Characteristics of phase transitions. (i) shows the free energy expansion versus polarization, (ii) shows the order parameter (spontaneous polarization P_s is shown) versus temperature and (iii) shows the reciprocal permittivity, κ versus temperature.

1.4 Relaxation versus resonance

The distinction between resonance and relaxation can be understood simply in terms of the presence or absence of the restoring force. This is discussed in greater detail in section 5.1 to explain the Raman spectrum of NBT, but an abbreviated version is useful to understand the more general aspects of relaxation. The standard equation of motion for a driven damped harmonic oscillator[55], commonly used to describe

atomic motion, is:

$$\ddot{u}_i + \Gamma_i \dot{u}_i + \omega_i^2 u_i = F e^{i\omega t} \tag{1.2}$$

where u_i represents the displacement of an i^{th} mode, ω_i is the natural frequency and Γ is the damping constant for each of the i^{th} modes. F is the amplitude of an external sinusoidal driving force with frequency ω. When $\omega \approx \omega_i$, the system amplitude greatly increases due to resonance. If there is no restoring force then the system is no longer resonant but follows the driving frequency with a time dependent lag known as a phase difference. If the system has both resonant properties and a non-constant restoring force, such as might be expected when the atoms in perovskites have multiple potential wells, then there is a dispersion in the frequency response similar to relaxor ferroelectrics described in section 1.5. If the applied force is static without a time dependence, then the ω_i term disappears and $\ddot{u}_i + \Gamma_i \dot{u}_i$=F remains, which is an equation of diffusion that is commonly used to describe relaxation[56]. A time dependent response to a perturbation of any of the thermodynamic parameters of a system is known generally as a relaxation, but the nomenclature used to identify the response of various applied forces is often application specific as will be explained below. The Gibbs free energy is described as[8]:

$$G = U - TS - X_i x_i - E_i D_i - \mu N \tag{1.3}$$

where U is the internal energy, T is temperature, S is entropy, X_i is stress, x_i is strain, E_i is the electric field, D_i is the displacement, μ is the chemical potential and N is the number of chemical units. Any applied change to the system will result in an immediate response, and a time dependent response. An example is creep[50], also known as strain relaxation due to an applied force without a sinusoidal character. Strain is a second rank tensor used to describe the relative change in length of an object, or in this case a lattice structure, with respect to an its original length[57]. Each tensor element includes variations into the other Cartesian axes via the expression $\eta_{ij} = \frac{1}{2}\left(\frac{x_i - x_j^o}{x_j^o} + \frac{x_j - x_i^o}{x_j^o}\right)$. Therefore an object's strained dimensions, x,y,z, are related to its original dimensions, x^o,y^o,z^o, via the nine element, unitless

tensor:

$$\begin{bmatrix} x \\ y \\ z \end{bmatrix} = \begin{bmatrix} \eta_{xx} & \eta_{xy} & \eta_{xz} \\ \eta_{yx} & \eta_{yy} & \eta_{yz} \\ \eta_{zx} & \eta_{zy} & \eta_{zz} \end{bmatrix} \begin{bmatrix} x^o \\ y^o \\ z^o \end{bmatrix} \tag{1.4}$$

Strain due to a phase transition occurs along the principal axes of the unit cell and the number of possible directions are dependent on the space group[46, 58]. Given a time dependent stress, X(t), of the form[50]:

$$X(t) = \begin{cases} 0, & \text{for} \quad t < t_1 \\ X, & \text{for} \quad t_2 < t < t_1 \\ 0, & \text{for} \quad t > t_2 \end{cases} \tag{1.5}$$

The resulting strain is observed to follow the pattern shown in figure 1.5. The curve (a) is for an ideal elastic material that responds completely to the applied stress without a time dependence, while curve (b) represents the time dependent anelastic relaxation. The analogous time dependent change of polarization to applied electric field is referred to as aging[59]. Observation of dielectric aging characteristics is useful to determine the thermodynamic equilibrium in KTN. Aging in NBT has been observed over a six hour interval near the lower phase transition[60, 61].

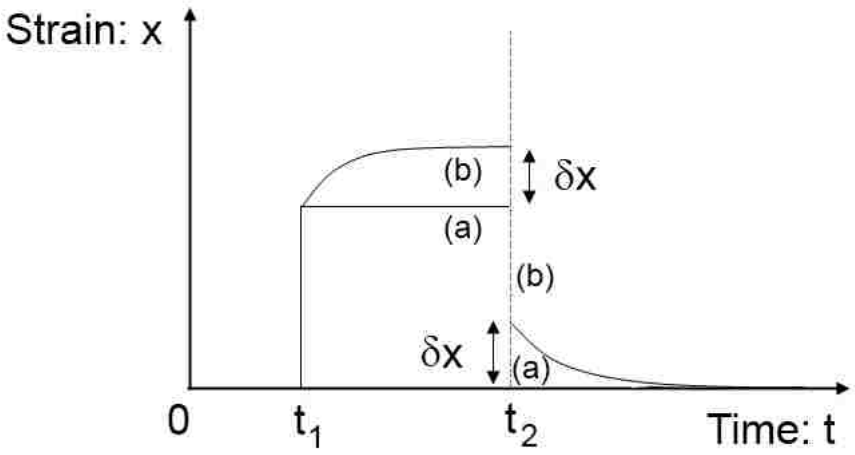

Figure 1.5: Strain response to abrupt application of external stress as per equation 1.5

1.5 Relaxor Ferroelectrics

1.5.1 Ferroelectrics

A crystal is labeled as ferroelectric if it possesses a spontaneous polarization that can be reoriented with an electric field[8]. This reorientation produces a hysteresis in the polarization curve as illustrated in figure 1.6(a)[62]. The labels in figure 1.6(a) indicate observable features such as the spontaneous polarization, P_S, the remnant polarization left after removal of the electric field, P_R, and the coercive field required to bring the polarization back to zero is E_C. The onset of spontaneous polarization can be either first or second order as explained in section 1.3, but second order is shown in figure 1.6(c). The result of this sudden onset of polarization is a strong optical anisotropy at the phase transition which results in birefringence. This is explored in more depth in section 3.2. The third standard feature of ferroelectrics is critical behavior in the dielectric constant as illustrated in figure 1.6(e). The inverse constant follows the Curie-Weiss law and exhibits linear behavior as a function of temperature in the form of ϵ'=C/(T-T_c), where T_c is the phase transition temperature. Several excellent histories of the ferroelectrics[63] and their ceramics[64] are available.

1.5.2 Relaxor Ferroelectrics

Relaxor ferroelectrics are a subclass of ferroelectric materials that have several distinct properties that distinguish them from ordinary ferroelectrics. The first is that the polarization hysteresis exhibits an "S" shaped or slim loop curve, which indicates that the polarization is due to small nanometer sized polar domains. These nanometer sized domains can exhibit polarization far above the phase transition temperature as seen in figure 1.6(d), thus preventing any obvious optical anisotropy changes at the phase transition. The change in the dielectric constant shown in figure 1.6(f) includes a much broader peak and frequency dispersion as a function of temperature which indicates a slowing down of dipolar motion due to increasing size.

In addition to the characteristics shown in figure 1.6, there are many additional properties that are understood to occur in relaxor materials. The first is that in the high temperature paraelectric phase there are several unusual features that significantly alter the macroscopic properties. The first is the onset of PNR's below the Burns temperature, T_B, first identified by the deviation of the refractive index from its linear temperature evolution[65]. They have since been widely observed in many relaxor materials[27, 66] through elastic neutron and X-Ray experiments and from the deviation of the inverse dielectric permittivity from the linear Curie-Weiss law. These PNR's are dynamic, reorientable, and range from 1.5 to 7 nm in size, with a correlation length that increases with decreasing temperature. Closer to the phase transition temperature there are several labeled temperatures mentioned that are indicative of different phenomenon. Relaxors have structural phase transitions to either a spin glass state, denoted by T_g, or a ferroelectric state, indicated by T_c. The onset of quasi-static local phase transitions, where the PNR's can no longer reorient, occurs about 20 to 40 K above T_c and is identified by T^*. The frequency dependent dielectric maxima occurs at T_m.

1.6 Soft modes

The term or label soft mode is a label applied to one or more low frequency phonon modes that move towards zero frequency as the temperature approaches a phase transition[56]. This decrease is due to the weakening of the restoring force of the corresponding atomic displacement, which also goes to zero until the phonon has condensed out and becomes optically inactive. The soft mode characteristics depend on the type of phase transition, commonly referred to as displacive or order-disorder based on whether the soft mode is resonant[67] or diffusive[8].

Soft modes in displacive systems generally originate in the zone center of the Brillouin zone and result from an instability of one of the normal modes of the lattice[68]. A displacive transition also has a single minimum in the potential energy at Q=0 as shown in figure 1.4(b)(i) and is therefore a subset of second order

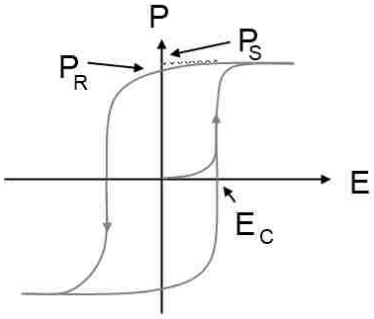

(a) FE-Macro size polar domains

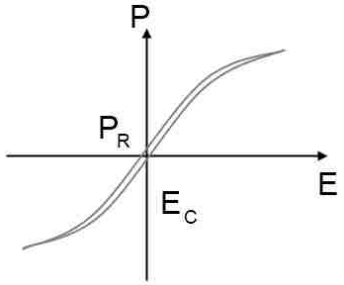

(b) RFE-Nano size polar domains

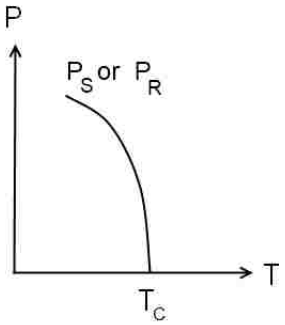

(c) FE-No polar domains above Tc. Strong optical anisotropy across Tc

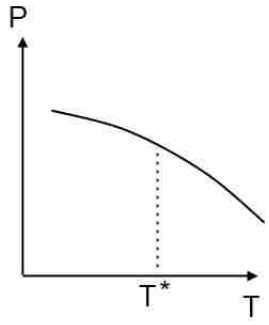

(d) RFE-nano sized polar domains exist well above T*. No optical anisotropy across Tc or T*

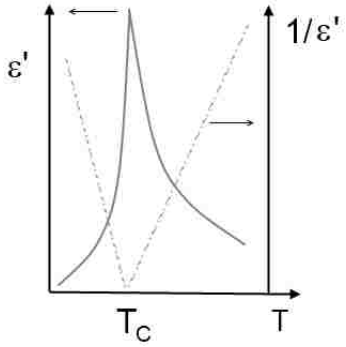

(e) FE-Sharp narrow transitions in dielectric constant, no frequency dispersion and ϵ' follows Curie Weiss law.

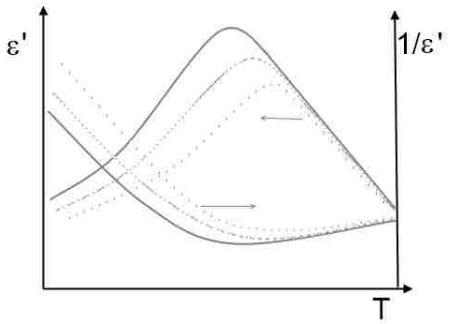

(f) RFE-Broad ϵ' peaks, strong frequency dispersion, strong deviation from Curie Weiss law.

Figure 1.6: Comparison between ferroelectrics (FE's) and relaxor ferroelectrics (RFE's).

transitions[56]. Ferroelectric phase transitions are the result of the condensation of the soft mode, which is polar, optically active, often damped, and both the real and imaginary portions are non zero away from T_c[56]. For this last reason these modes are commonly observed in the Raman spectrum of KTN[69]. A displacive transition can be understood qualitatively as a shifting of two intermeshed lattices with respect to each other. For example, if the anion oxygen octahedra are considered as forming one lattice, and the cations as forming a separate lattice in equilibrium relative to one another in the high temperature cubic phase, then below the transition the anions are collectively shifted relative to the cations as illustrated in figure 1.3(a). These sub-lattices can then be understood to have been displaced from one another. This displacement of sublattices is an example of a ferrodistortive transition and when this arrangement produces long range polar order the material is also ferroelectric. An alternative displacive configuration commonly seen in $SrTiO_3$, $KMnF_3$ and NBT is shown in figures 1.3(b) and 1.3(c). This transition is an example of an antiferrodistortive transition and if it has an intrinsic polar character,it is also referred to as anti-ferroelectric. The transition entropy is relatively small ($S \ll k_B \ln 2$) as the total lattice changes are small. The Lyddane-Sachs-Teller relation for resonant systems connects the dielectric constants to the lowest frequency mode, ω_T, which is the soft mode[70]:

$$\frac{\epsilon(0)}{\epsilon(\infty)} = \frac{\omega_L'^2}{\omega_T'^2} \tag{1.6}$$

where the static ($\epsilon(\omega)$) and high frequency ($\epsilon(\infty)$) dielectric constants are related to the zero ($\omega_L'^2$)and poles($\omega_T'^2$) of longitudinal and transverse normal modes of the dielectric response function. Comparing the temperature evolution of $\epsilon(0)$ and the ω'^2 of the soft mode provides a method of identification and confirmation for the character of the phase transition.

Soft modes are also observed in order-disorder transitions, but these modes originate at the zone boundaries and are of finite wavelength[56]. The order-disorder transition has a double well potential with an unstable saddle point at Q=0 similar to a first order transition. This potential results in large amplitude thermal hopping

or tunneling between wells that are described by unstable pseudo-spin waves[56]. The associated soft mode is diffusive and the imaginary part of the frequency is always non zero, while the real part is nonzero only if the tunneling splitting of the ground state is significant. The order-disorder transition can be understood qualitatively as the freezing that occurs at a liquid to solid phase transition. In solids this is understood as a local reordering of a component of the lattice from a disordered state, either atoms, dipoles, octahedra or polar regions, into new periodic arrangements. Typical order-disorder materials include potassium dihydrogen phosphate or KDP[71], $NaNO_2$ and NH_4Cl[67]. The transition entropy is relatively large ($S \approx k_B \ln 2$) as the total lattice changes are significant. The Lyddane-Sachs-Teller relation for relaxational systems of the Debye form is as follows[56, 67]:

$$\frac{\epsilon(0)}{\epsilon(\infty)} = \frac{\omega_p''}{\omega_L''} \tag{1.7}$$

where ω_p'' is the pole and ω_L'' is the is the zero of the dielectric function. It should be noted that few materials are purely displacive or order-disorder, and most exhibit characteristics of both transitions[8].

1.7 Central peaks and relaxations

Central peaks (CP's) are collective relaxation modes that appear around the laser excitation Rayleigh peak in Raman and Brillouin spectra and can also be observed around the Bragg peaks in neutron spectra[72, 73]. These peaks are typically modeled with one or two Lorentzian line shapes for simplicity[74], although it is recognized that there may be a distribution of modes. There have been many physical origins attributed to central peaks in the excellent review by Lyons and Fleury[74] and correct assignment must take into account the known physical attributes of the system in question. As the central peaks often overlap the soft modes and can couple to them, they must be considered together.

CP's in Raman spectra near displacive phase transitions are often due to the relaxation of precursor fluctuations which grow in size when approaching the transition[75].

The possible origins of these fluctuations include domain wall fluctuations[76], defect mobility[77], PNDs (or elastic clusters[78]) and an overdamped optical soft mode, either coupled to the precursor fluctuations or to an acoustic mode[79]. The cluster model was successfully invoked for KTN using PND's[80]. The eight site Nb potential acts as a memory with a Debye form[56, 79] when the Nb atom moves between sites, and the resulting energy shift gives rise to a Lorentzian line shape in the Raman spectrum. As the PND's are precursor regions of the lower symmetry phase, the temperature dependence of the central peak parameters of width and amplitude will reflect the slowing down of the dynamical fluctuations. The central peak width in KTN shows an Arrhenius temperature dependence[80] of the relaxation time, τ, that follows $\tau = \tau_0 exp(U/k_B T_c)$, indicating a slowing down of the dynamics near the transition. τ_0 is the relaxation time, U is the activation energy to move the Nb between sites, k_B is the Boltzmann constant and T_c is the transition temperature.

By contrast, the CP's in an order-disorder transition can understood with a pseudo-spin formalism using Pauli spin matrices[56]. There are two possible variations, the first of which involves a low, shallow potential barrier between the two equilibrium sites so that there is a well defined wave which behaves as a soft mode and propagates elementary excitations. The other variation involves a large, wide potential barrier so that there is no soft mode, only a relaxational type response. This variation has two relaxation times, a resonant soft mode and the other which varies negligibly with temperature with a Debye form[75]. It is expected from dielectric studies of relaxor ferroelectrics and order-disorder transitions that the temperature evolution of the central peak width will follow a Vogel-Fulcher form of $\tau = \tau_0 exp(U/k_B(T - T_f))$[81]. The Vogel-Fulcher formalism describes the dynamics of precursor regions down to a freezing temperature, T_f which may be independent of the phase transition temperature, T_c. The central peak in NBT has not yet been quantitatively deconvoluted, and this is one of the main objectives of this study[82, 83].

1.8 Purpose of study

Interest in structured crystals, exploiting the natural tendency of solid solution materials to form striations, provides a stable volume phase grating that is impervious to annealing treatments of a few hundred degrees K above the transition temperature. Optical applications of KTN are using striated crystals are very promising and the existence of internal strain, which interacts with the incident laser light, can alter the expected behavior. Our investigation into the evolution of the birefringence as a function of temperature in the paraelectric phase reveals new physics as well as the potential for novel functionality in future device applications.

Raman investigation of NBT using a detailed analysis in the low frequency spectral region reveals information about the strain related dynamics of the phase transitions. The temperature evolution of the central peak parameters are shown in order to better understand many of the unique features of the phase transition dynamics. Also, the low frequency soft modes are examined to determine the correct space group as well as to confirm the nature of the phase transition.

Chapter 2

Experiment

2.1 Sample Preparation

The KTN sample was flux grown and provided by Lynn Boatner of the Oakridge national lab using the slow cooling method[18], while the KLTN samples were created by the top seeded solution growth (TSSG) method and came from Aharon Agranat of the Hebrew University of Jerusalem. The KTN sample was polished to optical quality using a Buehler fibermet polishing device with the sample mounted using thermal wax on a custom jig. The KLTN samples were polished by the crystal provider. The surface quality was verified using an Olympus microscope and by examination of the reflection of a laser beam from the sample surface. The KTN sample was heated to 335 °C for 1 hour to remove any mechanical stress from the polishing process. The Al electrodes were applied via vapor deposition to the [001] rough polished faces that are co-planar to the striations and the 0.05 mil Pt wires were attached with Ag paint. The samples were cut and optically polished along the [100] direction, which was perpendicular to the visible striations in the samples as illustrated in figure 2.4. The dimensions are listed in the table below. The NBT samples were polished to optical quality in a similar manner and heated to 325 °C for 1 to 2 hours to bleach the crystals and restore transparency between experimental scans. The NBT samples were also TSSG Grown and provided by Haosu Luo of

Sample	length(L) (mm)	Width (W) (mm)	Height (H) (mm)	T_c (Kelvin)
KLTN 15.5	6.15	5.58	5.18	131
KLTN 36:CuV	4.25	1.52	1.23	275
KTN 27.7	3.39	1.70	1.04	213
NBT	2.0	2.0	0.87	$\approx$ 820/570

Table 2.1: Sample Dimensions

the Shanghai Institute of Ceramics.

2.2 The spectrometer

The Raman measurements were made with a Horiba JY U1000 spectrometer, originally manufactured by Instruments SA, Inc. This double monochromator is equipped with a pair of holographic, 1800 grooves/mm gratings and has a spectral bandwidth of 9.2 $\frac{1}{mm.cm}$ at 514.532 nm. The entrance and exit slits were set to 0.2 mm so that the final spectral resolution was 1.84 cm^{-1}. The spectral range is from 324 nm to 910 nm. The cryostat is mounted into a macrochamber adjacent to the U1000 so that an experimental geometry of 90° is obtained as illustrated in figure 2.2. A manually adjustable disc focal lens is mounted between the cryostat and spectrometer which allows specific portions of the sample to be imaged onto the entrance slit of the spectrometer. Each monochromator has a horizontal axis of rotation with an asymmetric Czerny-Turner configuration, shown in figure 2.1(b), with flat gratings, spherical mirrors and a 1 meter focal length. In figure 2.1(a), each monochromator takes the light from the entrance slit, S1, and focuses it onto the first mirror, MC1, which images the light as a parallel beam onto the grating. The prismatic reflection off the grating is sent to MC2, which images the now separated frequency components onto the intermediate exit slit, S2. S2 functions as a frequency selector and noise reducer, allowing only a narrow frequency range through the slit. This reduced beam is sent to the second monochromator via the flat mirrors M1 and M2, and through the identical second monochromator which further separates the

frequency components. The final frequency which emerges from the exit slit, S4, can be selected by rotating the grating. The two gratings are rotated synchronously by a motor controlled from the Horiba Labspec 5.0 software which allows a scan over a given frequency region, step sizes as small as 0.05 cm^{-1}, counting times from seconds to minutes and also provides backlash correction after resetting the grating position at the end of each scan. The output is directed onto a thermoelectrically cooled Hamamatsu R649 photomultiplier tube (PMT). The PMT is limited to a maximum output of 6×10^6 pulses per second, thus requiring a shutter mechanism when investigating near the Rayleigh peak. The PMT output is read by a discriminator/amplifier setup provided by Horiba JY and recorded by their Labspec 5.0 software. After each scan, the U1000 is reset to its original position. This reset is not precise, and varies by 0.05 to 0.2 cm^{-1} with each scan, ranging from $\pm2cm^{-1}$ over the course of 20 to 40 consecutive scans. While this is not significant for the higher frequency Raman peaks, correction of the data is essential for analysis near the Rayleigh peak.

2.3 The excitation sources

The KTN samples were investigated with the 633 nm laser line of a HeNe gas laser which produced a monochromatic linearly polarized beam at 2 mW with fluctuations of 2%. The NBT samples were investigated with various wavelengths of a linearly polarized, Coherent I90-C Ar ion gas laser and fluorescence measurements were made with the 442.1 and 325 nm lines of a HeCd laser at 200 mW. Raman measurements were taken with the laser stabilized at 1 W so that the manufacturers specification of intensity fluctuations of less than 0.3% were obtainable. The 514.532 nm wavelength was utilized for the Raman measurements, and the 454, 487.987, 496, and 501.2 nm lines were used for investigation of fluorescence. The Ar Ion laser output was filtered through a pair of Pellin Broca prisms and collimated through the lens and pinhole arrangement shown in figure 2.2. This filtering arrangement prevents undesired plasma lines of the laser from appearing in the spectral results.

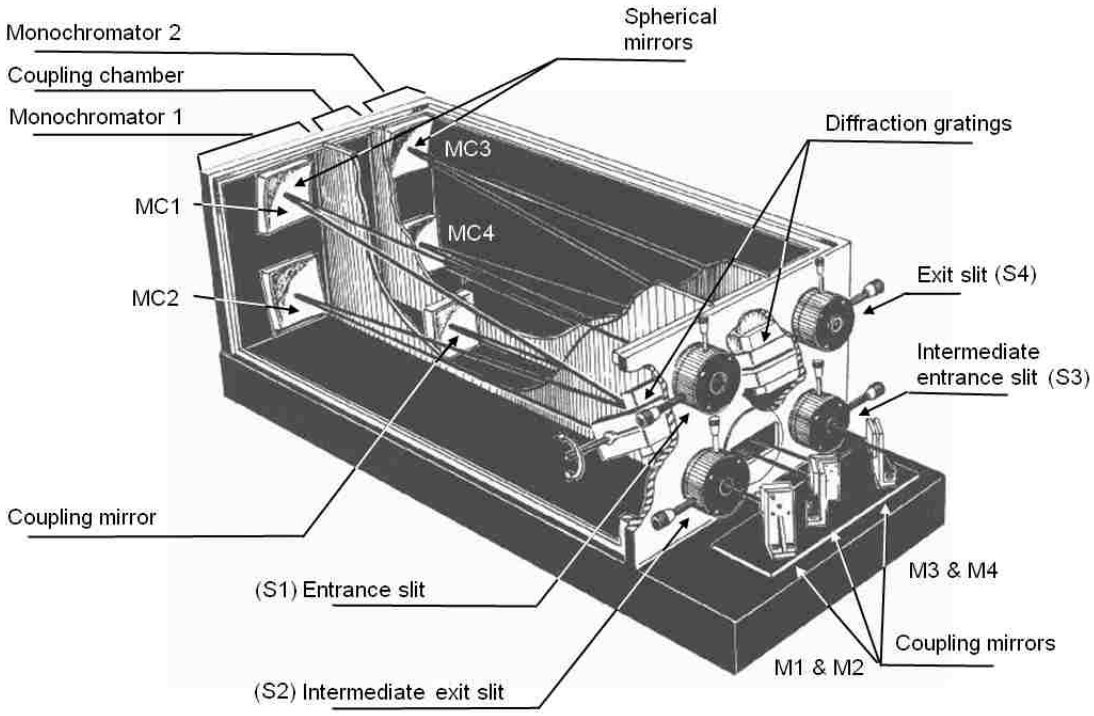

(a) Annotated schematic (from the manufacturers user guide)

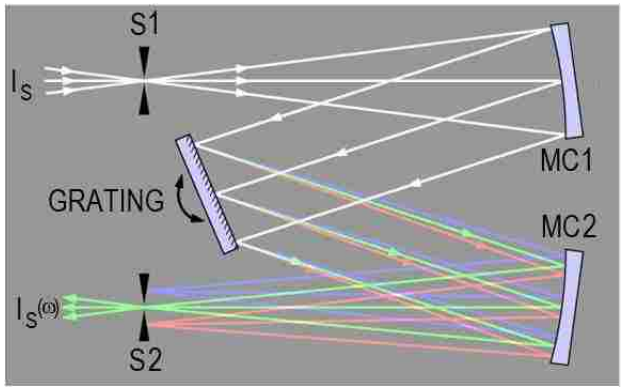

(b) Basic Czerny-Turner monochromator design.

Figure 2.1: Horiba JY U1000 double monochromator.

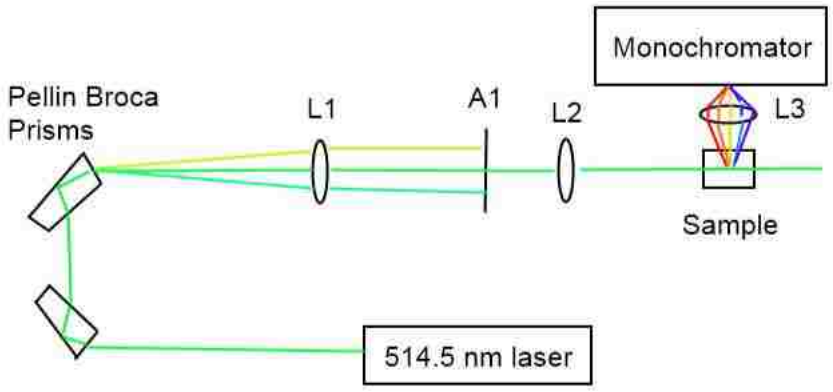

Figure 2.2: Ar ion laser beam path with prismatic filters

2.4 KTN experimental set-up

The KTN experiment was conducted with the apparatus shown in the figure 2.3. The polarized 633 nm HeNe laser was sent through a variable beam splitter (VBS) to reduce the intensity to ≈3 μW in order to prevent the formation of space charge fields[3, 84]. The beam was then sent through a focusing lens (L1), polarizer (Pol),and a pinhole aperture (A1) prior to arriving at the sample held inside the cryostat as shown in figure 2.5. After exiting the sample the beam was directed through a second aperture(A2) to remove any residual scattering, an analyzer(Ana) and a second focusing lens (L2) to ensure that the Si diode photodetector acquired the full intensity. This signal was compared to the intensity without the sample in place.

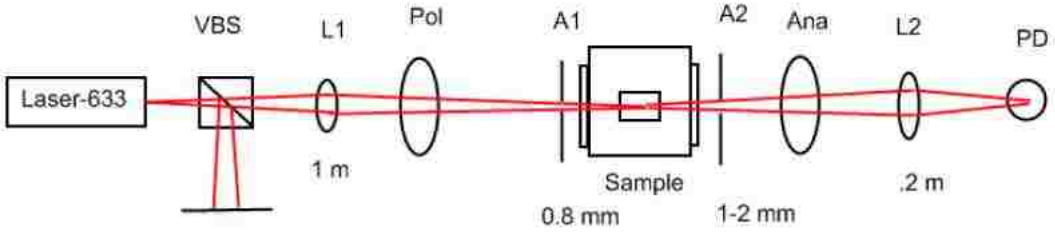

Figure 2.3: KTN experimental set-up

The incident laser beam propagation direction was normal to the crystal cubic face as shown in figure 2.4, such that the laser polarization could be aligned with a standard $\frac{\lambda}{2}$ plate to have a polarization orientation of transverse magnetic (TM or I_{90}), transverse electric (TE or I_0) or 45 (I_{45}) degrees orientation with respect to the plane of incidence. The plane of incidence is defined by the vectors of the laser propagation direction, which is parallel to the striation planes, and the striation normal vector, $\vec{K}$. These are shown in figure 2.4 and are consistent with the conventions of coupled wave theory so that the TE and TM orientations are orthogonal and uncoupled[85]. This arrangement is similar to work by prior authors[3, 86].

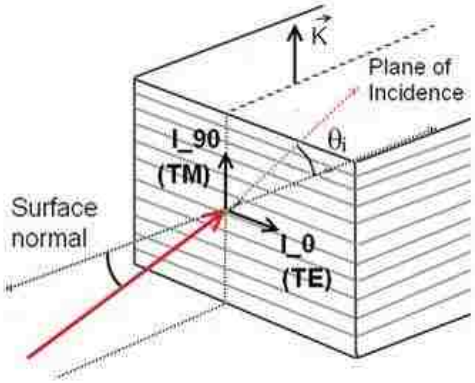

Figure 2.4: Image showing the light propagation direction with respect to the crystal striations and the polarization orientation of the electric field.

2.5 Dielectric measurements

The dielectric measurements were obtained on the KTN Crystals using a Labview controlled Agilent HP4194 Impedance analyzer. A 25 mV ac signal was applied over a range of frequencies from 100 Hz to 2 MHz at each temperature measured. These measurements were obtained independently of the optical measurement. Dielectric aging was investigated at all temperatures to verify thermal equilibrium.

2.6 Cryogenic temperature control

During the Raman scattering experiment with NBT the sample was mounted inside a Cryo Industries Inc. RC-102 cryofurnace capable of temperatures from 4 to 1000 K. The diagram is shown in figure 2.5. This is a continuous flow system used with gaseous nitrogen evaporating from a liquid state at 77 K. The sample chamber was evacuated to a pressure of 1 mTorr to prevent condensation at low temperatures and oxidation of the copper mounting plates at high temperature. A PT100 platinum resistive sensor was used with a Lakeshore Inc. model 300 temperature controller internally set to the PT100, which provided temperature stabilization to ± 0.1 K. Several custom modifications to the cryostat were necessary to allow the intended research. Due to an inherent limitation in the Lakeshore controller, which can only measure up to 300 Ohms ($\approx$810 K on the PT 100 scale), a 1650 Ohm precision resistor was mounted in parallel with the PT100 so that 300 Ohms corresponds to 1000 K, thus allowing temperature control over the full range of measurement. Also, a $\frac{1}{3}$ inch copper mounting plate previously installed had become thermally fused to the original manufacturers mounting plate. This extra mass and radiant area prevented the original 2 heater system from achieving the needed 1000K, so 4 additional heaters were added. These 4 heaters were supplied with power from a Variac adjustable power supply. The cryostat was mounted on a custom mount platform with X,Y,and Z axis micrometer precision positioners and a 3 point tilting platform.

During the KTN Optical measurements, a separate Cryo Industries RC-102 cryostat with Si sensors was used that was capable of temperatures from 4 to 325 K. The same Lakeshore controller was used but the internal settings were changed to accept input from the Si sensor, and temperatures were also controlled to ± 0.1 K. This was mounted with the same positioning mount used in the Raman measurements.

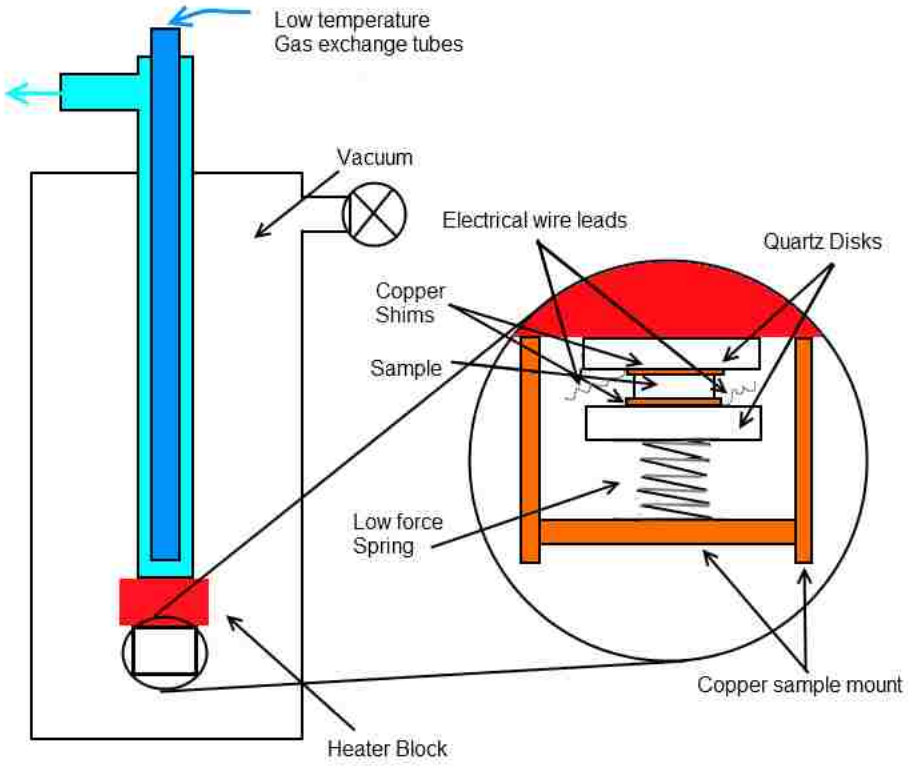

Figure 2.5: Lakeshore Industries RC-102 Cryostat with mounting arrangement for samples

2.7 Sample mounting into cryostats

The NBT sample was mounted as shown in the figure 2.5. The sample was first placed between 2 copper shims of 0.05 mil thickness to provide a mechanical cushion at high temperatures, as well as to provide a conductive surface to allow redistribution of the bound surface charges that appear due to polar domain formation over a phase transition. If the surface charges are not dispersed, cracking and fracturing of the crystal can result due to electrostatic repulsion. The shims were separated from the cryostat copper mounting with thin 0.5 mm fused quartz plates in order to prevent the shims from thermally bonding to the cryostat at high temperature and to distribute the mechanical pressure from the spring. The sample/shim/plate

arrangement was held against the copper cryostat surface with a custom built Inconel 718 $\frac{1}{2}$ inch diameter, ground flat end, low force spring. The Inconel 718 is the only material available that will still function as a spring at high temperatures. The KTN sample was similarly mounted between two quartz discs and held in place with a spring made of coiled copper shim. As the KTN had Al electrodes with Pt wires attached, the quartz plates provided electrical insulation.

2.8 Absorption

The absorption measurements were made on a SPEX Cary 10 UV/VIS spectrophotometer. These measurements were only obtainable at room temperature. The SPEX unit has 2 lamps, visible and UV, whose light is sent through a double monochromator equipped with a filter wheel that restricts the light incident on the sample to a narrow bandwidth. The input light scans from the IR range down to the UV in order to prevent any cascading processes. This light is sent through 2 beam paths, one with a sample and one without as a reference, and the result is normalized with data obtained from both paths without samples.

2.9 Procedural notes

All of the experiments were performed as a function of temperature except for the absorption and optical microscopy experiments which were only obtained at room temperature. Prior to conducting a spectrum scan the sample temperature must be adjusted and stabilized. This was accomplished by permitting the sample to thermally equilibrate for 15 minutes after the desired sensor temperature was reached. This was confirmed in the KTN sample by measuring the stability of the dielectric signal (aging) at a given frequency over a 3 minute span. It is important to observe this equilibrium protocol or the data may fluctuate in an unpredictable manner. The time frame for true equilibrium of the NBT sample was found to exceed 6 hours[61] in the temperature region near the lower phase transition. Repeated

Raman scans over a 10 hour period at various temperatures from 400 to 650 K were obtained and no change in the spectrum was observed, either in intensity or spectral peak positions. The Raman signal intensity was also checked at every temperature measured to verify signal stability as an indicator of equilibrium. The data of both KTN and NBT are very sensitive to small changes in temperature and laser power, and due to thermal hysteresis effects, the results can vary greatly depending on the direction of temperature change. As a result, both KTN and NBT were measured starting from an initial temperature and heated or cooled in discrete temperature steps so that the direction of temperature change was never reversed.

Chapter 3

Refractive indices, Birefringence and Strain

3.1 Refractive indices

A material's refractive index is defined as n=c/v, where c is the speed of light in vacuum[87] and v is the speed of light in the material. The refractive indices are dependent on the material properties including electronic density and their associated oscillator strengths[88]. These oscillator strengths are strongly affected by the structural phase of the material as shown in section 1.3. A cubic material is optically homogeneous and has only a single refractive index. Tetragonal materials have two refractive indices and are referred to as uniaxial while monoclinic materials are biaxial with three indices. Obtaining precise values for the refractive index is not trivial and not always practical as in the case of NBT, which is multi-domain at room temperature. The refractive indices of KTN as a function of niobium concentration have not been published and only a few examples are available in the literature. In order to estimate the average refractive indices of the KTN samples, the Clausius-Mossotti relations[89] in equation 3.1 were used with the known indices of the end materials: cubic KTaO3[1] and both cubic and tetragonal KNbO3[2] as shown in figure 3.1.

$$3\left(\frac{n^2-1}{n^2+2}\right) = (1-x)\gamma_{(KTaO_3)} + x\gamma_{(KNbO_3)} \tag{3.1}$$

Where n is the refractive index, x is the niobium concentration and γ is the polarizability. The results are shown in table 4.1 and figure 3.1. The refractive indices are necessary to use Snells' law in determining the refraction angles inside the crystal. The frequency of the applied laser exceeds the frequencies of any elastic waves[59] and therefore the crystal can be considered as clamped, and the low power of the laser precludes any electro-optic contribution[84, 90].

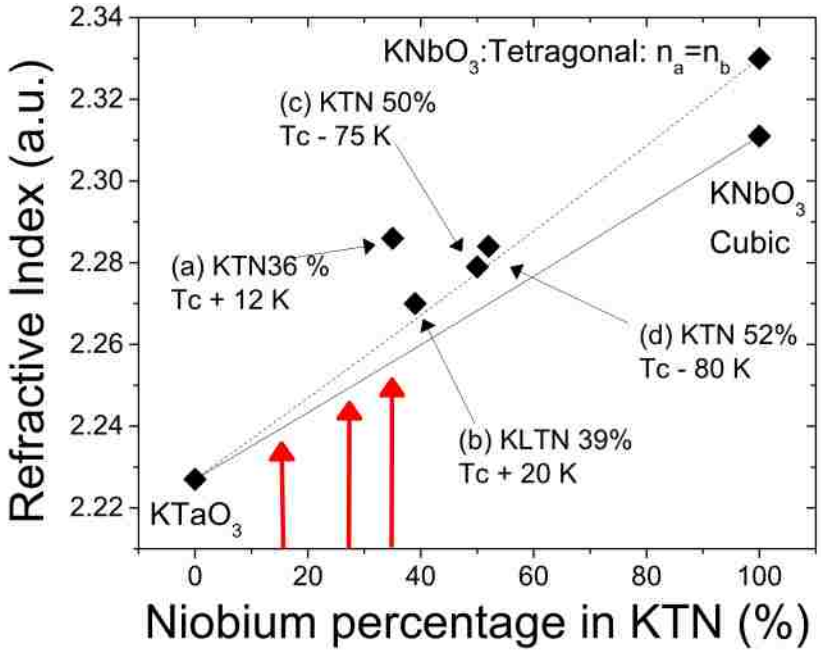

Figure 3.1: Refractive indices comparison between the end materials KTaO3[1] and KNbO3[2] versus several samples measured near and below the cubic-tetragonal transition temperature Tc. (a)[3],(b)[4],(c)[5] and (d)[6] are closer to the dashed line connecting the cubic $KTaO_3$ to the tetragonal $KNbO_3$. The vertical red arrows mark the estimated concentrations for the three samples used in this study.

3.2 Birefringence

Birefringence is defined as the double refraction of light which occurs in uniaxial and biaxial crystals. It is typically expressed as the difference between the two indices aligned with the crystalline axes of the material. Birefringence measurements are very sensitive and can be useful for observing changes in structure, either locally as in the relaxor PND's below T^* or macroscopically in ferroelectric transitions as explained in section 1.5. The expression for optical transmission through a birefringent crystal between crossed polarizers is given by[87]:

$$\begin{aligned} I &= I_0[\cos^2(\chi) - \sin(2\phi)\sin(2\phi - 2\chi)\sin^2(\tfrac{\Gamma}{2})] \\ \Gamma &= \tfrac{2\pi}{\lambda} L\delta n \end{aligned} \tag{3.2}$$

Where I_0 is the input light intensity on the crystal, $\cos\chi$ comes from Malus's law for the output intensity transmitted through two polarizers with their principal axes (PA) aligned at an angle χ with respect to each other. The second term in the left bracket describes the output through a uniaxial crystal with ϕ being the angle between the input polarization vector and one of the principal axes of the material. Γ is the phase difference between the ordinary and extraordinary beam paths in the crystal and is a function of crystal length, L, wavelength, λ, and effective birefringence, δn. This phase difference results in elliptical polarization. As this thesis will show, there are two main components to the birefringence in KTN, a volume birefringence and an intrinsic one. A qualitative form of δn will demonstrate the critical behavior of the phase transition more directly.

When both polarizers are oriented parallel to each other with so that χ=0 and $\cos^2\chi$=1 and ϕ=$\frac{\pi}{2}$, a configuration designated as " $\|$ "in the following figures, expression 3.2 becomes:

$$\frac{I_{\|}}{I_o} = \left(1 - \sin^2\left(\frac{\Gamma}{2}\right)\right) \tag{3.3}$$

Assuming no isotropic loss, $I_{\parallel}/I_0$=1 is the expected result when the input polarization is parallel to the optic axis at $\phi = 0$. The second term is relevant for any angle away from the PA. If the polarizer and analyzer are oriented so that $\chi = \frac{\pi}{2}$, a configuration referred to as "crossed" and designated by " $\perp$ " in the subsequent figures, then the resulting output should be entirely dependent on the birefringence of the crystal and expression 3.2 becomes:

$$\frac{I_{\perp}}{I_o} = \sin^2\left(\frac{\Gamma}{2}\right) \tag{3.4}$$

In this case the effective phase difference can be obtained directly from the data as:

$$\Gamma = 2\arcsin(\sqrt{\frac{I_{\perp}}{I_0}}) \tag{3.5}$$

Using the expressions 3.2 and 3.4, we are able to estimate the birefringence for the various crystals from the measurement of the transmitted intensities as a function of temperature.

3.3 Diffraction

Light diffraction occurs in solid state materials when there is a modulation or periodicity of the refractive index of the general form[91]:

$$n = n_0 + \sum_{m=1,2,3,\cdots}^{\infty} a_m \sin mx + b_m \cos mx \tag{3.6}$$

where n_0 is the average refractive index and a_m and b_m are the amplitudes of the various components. This modulation creates a volume phase grating that produces 1 or more diffraction beams whose output angles can be expressed as follows:

$$\sin\theta_{Tm} = \sin\theta_i \pm m\left(\frac{\lambda}{\Lambda}\right)\sin\beta \tag{3.7}$$

where the m^{th} order beam transmission angle, θ_{Tm}, is dependent on the incident angle of the light outside the crystal, θ_i, the wavelength of the light,λ, the periodicity

of the sinusoidal grating, Λ, and the angle of that grating with respect to the plane of the incident light, β. For this experiment, β is set at 90 degrees, and small deviations would have negligible effect on the angle variation. The reference, or incident, beam is coupled to the diffracted beam and there is a transfer of energy to the diffracted beam that is dependent on several factors. There are two well known cases for coupled wave equations due to refractive index modulation: one for a simple sinusoidal form[85] that shows a single diffraction beams, and one for a perfect layered material[92] that has many diffraction orders. The simple sinusoidal form is used for the KTN experiment as a first order approximation. Any modulation pattern between these two extremes can be modeled with a Fourier series like equation 3.6 if the refractive index profile can be accurately determined or estimated.

Figure 3.2 shows an example of the reflected and matching diffraction orders in a layered material. The $|K| = \frac{2\pi}{\Lambda}$ indicates the grating vector slanted at an angle β. The incident laser has a vector $|k_0| = \frac{2\pi}{\lambda}$ angled θ' from the surface normal, which becomes $|k_i| = \frac{2n\pi}{\lambda}$ at angle θ" inside the crystal. The diffraction orders are shown with the zeroth order indicating the undiffracted beam that follows the standard optical path due to Snell's law: $n_1 \sin\theta' = n_2 \sin\theta$"[87].

3.4 The photoelastic effect

Strain, as described in section 1.4, affects the refractive indices through the photo-elastic effect. The refractive indices, which are scalar values that do not transform as tensors, are connected to the dielectric permittivity via $\epsilon_{ij} = n_{ij}^2$. The photo-elastic components are defined through the impermeability tensor, which is defined as the inverse of the permittivity: $B_{ij} = \frac{1}{\epsilon_{ij}}$. These tensor elements make up the refractive index ellipsoid, also known as the optical index ellipsoid, and the impermeability tensor is expressed relative to the principal axes in the following:

$$B_{11}x^2 + B_{22}y^2 + B_{33}z^2 \tag{3.8}$$

where x, y and z are the Cartesian axes. The strained, B, and unstrained, B^0,

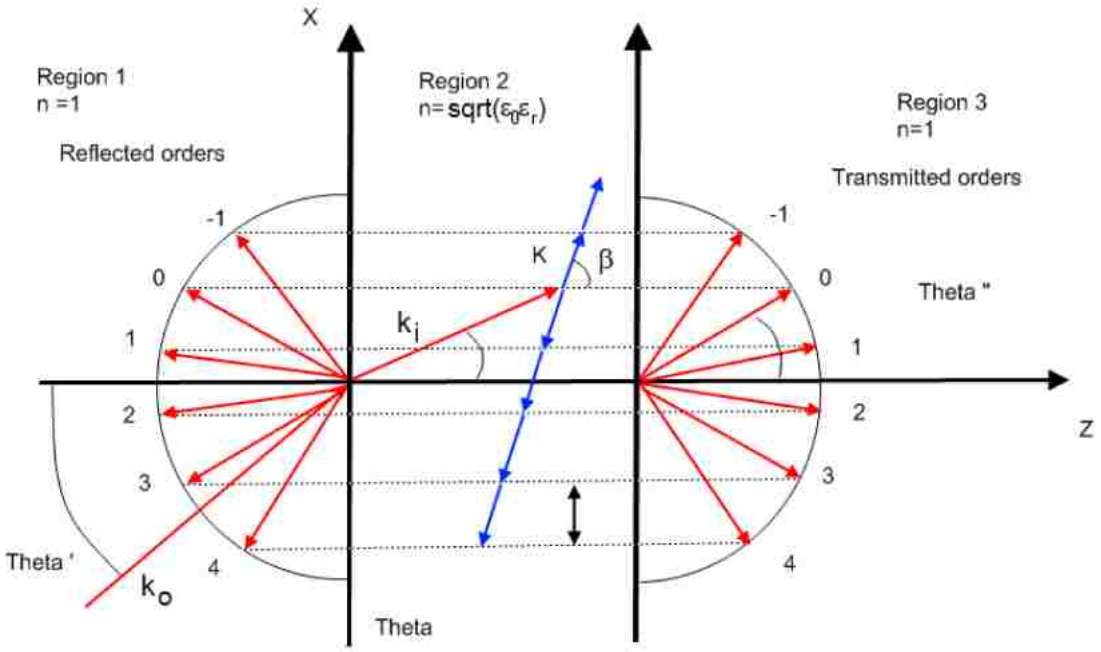

Figure 3.2: Diffraction orders observed due to modulation of the refractive index

ellipsoid values are different and this difference is expressed as a fourth order tensor in the form of:

$$B_{ij} - B_{ij}^{0} = p_{ijkl}\eta_{kl} \tag{3.9}$$

There are 81 p_{ijkl} photo-elastic tensor elements, but only 3 non-zero values are present in the cubic $Pm\bar{3}m$ phase: p_{1111},p_{1122} and p_{2323}=p_{1111}-p_{1122}[93]. The value of these coefficients are not known in the mixed system of KTN, but are known its' end materials[2, 94, 95].

Chapter 4

KTN Results and Discussion

4.1 KTN introduction

Two of the original promising applications for KTN were its potential for use as an electro-optic modulator [3, 32] and holographic storage[96]. Recently KTN has received renewed attention for optical communications applications,[38] beam scanners,[37] and variable focus lenses[39]. The interest in KTN is due to its high electro-optic coefficient, which makes it much more responsive to small electric fields[38]. The physical properties of KTN are strongly dependent on the Nb concentration. Dilute Nb concentrations below 1% do not have a phase transition but act as a dipole glass[62], while concentrations over 2% exhibit the phase transitions of the end material $KNbO_3$: cubic $Pm\bar{3}m$ to tetragonal P4mm to orthorhombic and finally rhombohedral[18, 53]. The focus for this thesis is on the higher temperature cubic $Pm\bar{3}m$ to tetragonal P4mm transition. This phase transition has been listed as a non-magnetic, full ferroelectric and partial ferrodistortive transition with 12 possible polar or strain orientations along the principal axes[46, 58]. As KTN is not known to exhibit rotations of the octahedra, any strain effects are due to the presence of polar domains. The dielectric spectrum indicates the phase transitions are first order above x=30%[14], and second order below[54]. The presence of soft

modes that approach zero frequency indicates that KTN has a displacive phase transition. These modes have been clearly identified in KTN in both Raman[69] and neutron studies[9, 97] to follow the linear ω^2 vs. temperature dependence which is consistent with the dielectric constant temperature evolution[14].

KTN and its doped substituents all exhibit the standard characteristics of relaxor ferroelectrics as described in section 1.5. The first, which defines the relaxor class, is the frequency dispersion of the dielectric constant, seen in KTN15.7% under application of a dc field[98], or in dilute concentrations below 8%[99]. The dielectric spectra of KTN is well known to follow the Curie-Weiss law as shown in figure 1.4(b)(iii)[14], however it also deviates from the linear temperature dependence below the T^* temperature range of 20 to 40 Kelvin above the transition, T_c[14], a response that was explained by the appearance of PND's[98, 100–102]. The second relaxor characteristic is the presence of "S" shaped or slim looped curves in the polarization hysteresis curves[98]. The third characteristic is the evidence of linear birefringence above the phase transition for low Nb concentration samples: x=0.008, 0.012, 0.02[103], 0.0028 and 0.06[11] and 0.076[104, 105].

The conventionally accepted theory, based on dilute Nb samples[62], is that PNR's are spontaneous polarization fluctuations formed when the off-center Niobium atoms create a local dipole that polarizes the surrounding region ($\approx$100 unit cells)[106]. This local polarization results in a strain field that couples to light via the photoelastic effect as explained in section 3.4. An ideal cubic material would have a homogeneous index of refraction and would not exhibit birefringence[107]. The PND's cause the cubic phase to become inhomogeneous and have been observed with a variety of methods including NMR[108], XFAS[10], Raman spectroscopy[102, 109, 110], resonant ultrasound[111], second harmonic generation[69, 105], and low-frequency dielectric measurements[101]. Dimensional changes have been reported in KTN in the PND region that do not follow the expected linear behavior[112, 113]. Below the cubic to tetragonal phase transition the PND's evolve into needle-like domains as seen with polarization microscopy [114] and exhibit a continuous change of linear birefringence with decreasing temperature[6]. These reports suggest that KTN should have interesting and potentially useful effects on the polarization of

light above the transition.

This thesis reports the temperature dependence of both diffraction and birefringent light transmission through three KTN samples at high temperatures in the cubic phase, even in the absence of a bias electric field. The birefringence was previously mentioned[32] to be the result of striations formed during crystal growth[34] but there are no reports to date of higher Nb concentrations that characterize it as a function of temperature. Nb concentration gradients in flux grown crystals[18] and striations in Top Seeded Solution Grown (TSSG)[34] materials are unavoidable consequences of the growth process for all solid solution materials due to temperature fluctuations in the growth melt[35]. Modifications of the crystal growth technique have been attempted to reduce the magnitude of striations[15, 18, 34] or, alternatively, to make them more prominent and uniform.[36] The end materials, $KTaO_3$ [12] and $KNbO_3$,[13] have similar lattice parameters at high temperature, 4.02 Åversus 3.99 Årespectively, which is a necessary condition for the formation of a stable solid solution[14]. X-Ray results for varying Nb concentration show an increase in the average lattice parameter with increasing Nb concentration[15]. Also, the refractive indices of the end materials are very different as shown in figure 3.1. It is noteworthy that the cubic phase measurements, taken below T^*, fall on or above the tetragonal a-axis line, indicating the presence of precursor PND's optically. The production of crystals with uniform striations may reduce local inhomogeneity of the birefringence, thus increasing their utility as optical devices. Interest in applications for volume holography with materials of fixed grating strength that are impervious to thermal annealing make it desirable to characterize this birefringence. The goal of this thesis is to describe the birefringent properties of several bulk KTN crystals with differing striation strengths, or contrast, and their temperature evolution in order to determine the origin of the unusual birefringence.

4.2 Optical Microscopy

The transmitted light intensity seen by optical microscopy provides details regarding the pattern of transmission. Figure 4.1(a) shows a broad region of transmitted light near the center of the crystal due to strain related birefringence caused by the Nb gradient across the crystal, while figures 4.2(a) and 4.2(b) show modulated light transmission due to striations. The samples are oriented in the standard way[34] so that the striations are at 45 degrees relative to the crossed axes of the polarizers. The striations of the KLTN15[36] sample seen in figure 4.2(a) are very regular, more prominent, and uniform in all parts of the crystal. In figure 4.2(b) the KLTN36 has striations that are less distinct and more random in modulation intensity. Note that the images were obtained at a room temperature of 295 K where all crystals are in the cubic phase.

As seen in figures 4.3(a) and 4.3(b), incident monochromatic light results in a diffraction pattern for the two striated samples, but there are no diffracted beams at any temperature from the KTN27 sample. The KLTN 36 produced a single diffraction beam when the incident angle of the laser was rotated away from the surface normal as shown in figure 4.3(a). At near normal incidence, only a single beam spot was observed. The KLTN15 sample gave rise to five diffraction beams, three of which are seen in figure 4.3(b). The beam diffraction angles for this sample were fixed with respect to the input angle of incidence, but their relative intensities changed as a function of incidence angle. The period of the striations in KLTN15 and KLTN36, shown in table 4.1, are large in comparison to the input wavelength of the light, but small in comparison to the 0.6 mm beam diameter and this ordering can therefore be considered as a volume phase grating[85, 115]. The output angle observed is consistent with expression 3.7 when using the modulation period and estimated refractive index from table 4.1.

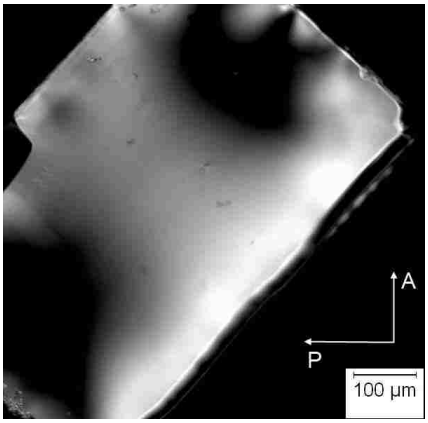

(a) KTN27-PA axes set 45 degrees to polarizer axes

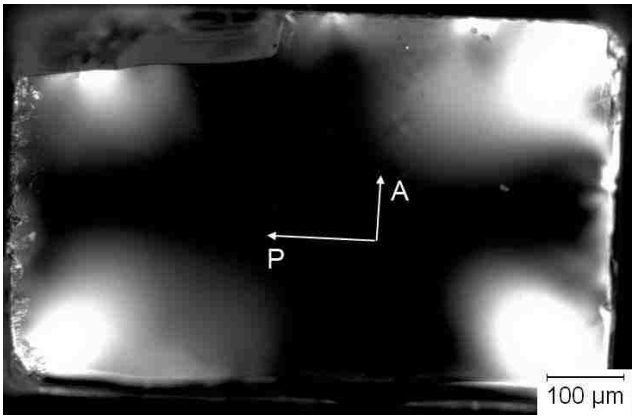

(b) KTN27-PA axes parallel to polarizer axes

Figure 4.1: KTN27 crystal shown through crossed polarizers in an optical microscope. Strain birefringence is observed in the corners in figure 4.1(b). The birefringence seen at the crystal center in figure 4.1(a) is due to the Nb concentration gradient common to flux grown crystals, but no obvious striations are seen at room temperature. The laser beam input was centered in the middle of the crystal.

4.3 Sample properties and Diffraction results

The principal axes (PA) in these samples were determined by the method of null ellipsometry, in which the polarizers are crossed and concurrently rotated until an intensity minima is located. The PA were also found to be parallel and perpendicular to the axes formed by the striations in the material. These striation planes were observed to be normal to the [001] surface of the crystal. This orientation was found to be independent of temperature and consistent with the required geometry for coupled wave equations[85] such that the TE and TM orientations are uncoupled as specified in section 2.4. The striation periodicity, estimated refractive indices and transition temperatures are shown in table 4.1. The optical path length for each sample is designated by the length or "L" dimension in table 2.1. Refractive indices were estimated using expression 3.1 in section 3.1. The Nb concentration was

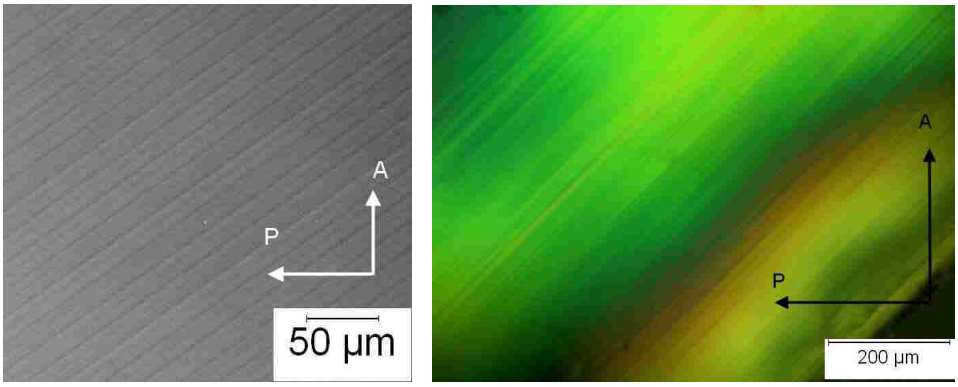

(a) KLTN15.5-Top seeded solution growth method with induced striations

(b) KLTN36- Top seeded solution growth method with random striations formed due to temperature variations in the growth melt

Figure 4.2: Striations of KLTN15 and KLTN36 crystals seen through crossed polarizers in an optical microscope. The striations are oriented at ≈45 degrees to the polarizer.

estimated by using expression T_c=682x+33.2 (Kelvin)[18, 116], which is useful for concentrations between 0.1≤x≤1. The T_c value used in this expression was obtained from the observed phase transition temperatures shown in figures 4.4(c), 4.5(a) and 4.5(b) by the sharp drop in both the dielectric constant and total intensity. The temperature dependent increase of the dielectric constant in KTN near the phase transition is understood to be a key indicator of the formation of PNDs[98, 117]. The striation periods were determined by digitizing the images shown in figures 4.2(a) and 4.2(b) using Matlab and estimating an average distance between peaks of light and dark using the distance scale shown. These widths were confirmed by comparing the separation of the diffracted beam(s) seen in figure 5 with expression 3.7 using the estimated refractive indices from table 4.1. Since the thermal expansion of KTN is approximately linear at temperatures greater than 40 K above the phase transition[118], the thermal expansion coefficients were used to estimate the change in optical path length due to thermal expansion at high temperature and this was found to have a negligible effect on the birefringence when used in expression 3.2.

This estimation is shown by the blue dash-dot line in figure 4.5(a).

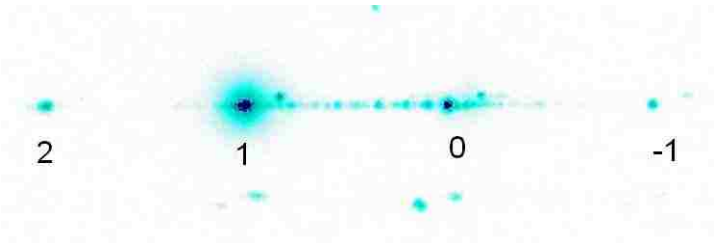

(a) KLTN15.5 with four prominent diffraction spots, 0.0424±0.0003 radians apart. The zeroth order beam is the undiffracted incident beam.

(b) KLTN36 with only 1 diffracted beam that varies with input angle.

Figure 4.3: Diffraction patterns for 2 crystals using inverted color palette where red dots on a black field are shown as blue dots on a white field.

4.4 Birefringence and Dielectric data

Table 4.1: Relevant crystal data

Crystal	Striation period (μm)	Estimated Refractive Index	Transition temperature: T_c (Kelvin)
KLTN15.5	14.92 ± 1.0	2.239	131
KTN 27	—	2.247	213
KLTN36	14.96 ± 3.3	2.254	273

Figure 4.4(a) shows the total transmitted intensity of the combined zeroth (ZOB) and first (FOB) order beams through the KLTN15 crystal with the polarization oriented parallel (I_0) and perpendicular (I_{90}) to the striation axes as per figure

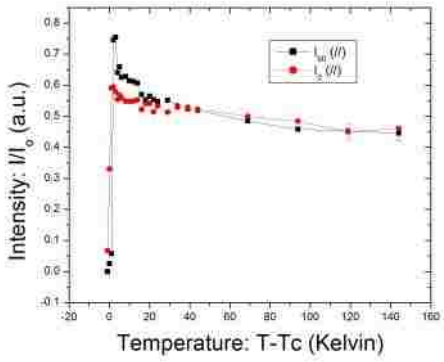

(a) Total intensity of transmitted light (ZOB+FOB) at each polarization input.

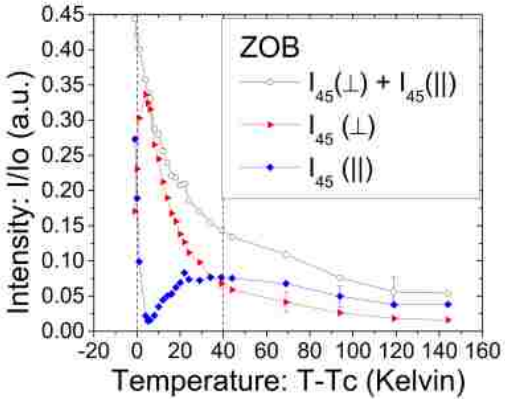

(b) Transmitted intensity normalized to incident beam for zeroth order beam with light polarization oriented to 45 degrees relative to the striation axes.

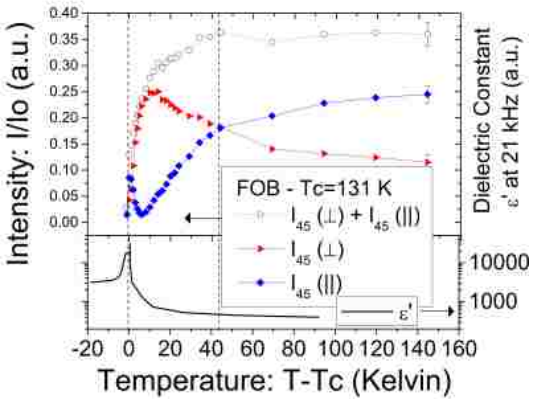

(c) Transmitted intensity normalized to incident beam for first order beam with light polarization oriented to 45 degrees relative to the striation axes. Dielectric constant data is shown in lower graph.

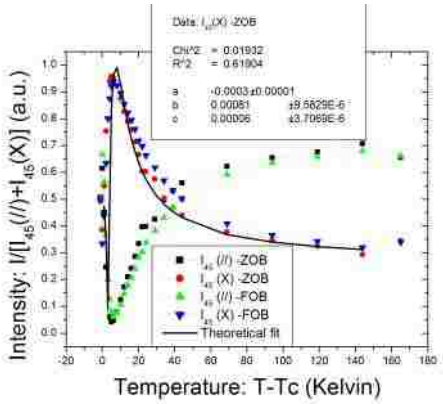

(d) KLTN15 intensity comparison of ZOB and FOB components from figures 4.4(b) and 4.4(c) are normalized to the summation values.

Figure 4.4: KLTN15 birefringence data as a function of temperature.

2.4. At higher temperatures the combined transmitted intensities of the ZOB + FOB beams are consistently near 45% of the incident intensity. Near the phase transition temperature, T_c, the transmitted intensities of the different polarization orientations increase at different rates, which reveals a change in reflectivity and

therefore a change in effective refractive index from the standard transmissivity equation for normal incidence: $T = 4n/(n+1)^2$[87]. Undoped KTN is known to have low absorption characteristics at 633 nm[119, 120], so this is not a possible cause of the changing refractive index. The abrupt drop in intensity over 2 degrees at the transition is caused by the crystal becoming cloudy, or milky, and optically opaque. The error bars shown on the highest temperature data points are based on a worst case drift of $\pm 2.5\%$ of the incident laser intensity.

Figures 4.4(b) and 4.4(c) show the change in birefringence as a function of temperature for the KLTN15. The -1 and 2^{nd} order beams have intensities less than half a percent of the total and therefore only the zeroth(ZOB) and first order (+1) beams(FOB) are examined. Figure 4.4(b) shows the transmitted intensity of the ZOB beam's $I_{45}(\perp)$ and I_{45} ($\parallel$) components along with their summation, referred to hereafter as the total transmitted intensity. As described in section 2.4, I_{45} designates the incident polarization rotated at 45 degrees relative to the TM or TE orientations. Both orientations have finite intensities at high temperature indicating birefringence. The intensity of the $I_{45}(\perp)$ component increases to a maximal value at T_c +4 K, indicating the light polarization is aligned with the axis of the analyzer, while the corresponding I_{45} ($\parallel$) component becomes nearly extinguished at the same temperature. The total intensity increases steadily from high temperature to T_c + 40 K, highlighted by the vertical dashed line, where an apparent inflection point begins a more rapid increase to T_c + 1 K, indicating a more rapid change in polarization orientation with decreasing temperature.

Figure 4.4(c) shows a similar temperature evolution for the FOB intensity of both the $I_{45}(\perp)$ and I_{45} ($\parallel$) components concurrently with the dielectric constant to emphasize both the transition temperature and the temperature range where PND's are observed. The dielectric constant was noted to take 15-30 minutes to reach thermal equilibrium when the temperature was within 2 degrees of the phase transition, but less than 5 minutes at higher temperatures. The total intensity of the FOB decreases as the ZOB increases, indicating that the intensity is shifting from the FOB to the ZOB, therefore implying a loss of diffraction efficiency. Regardless of

the changes in total intensities, when the $I_{45}(\perp)$ and I_{45} $(\parallel)$ components are normalized to the total values of their respective beams, they evolve in a nearly identical fashion as shown in figure 4.4(d). This similarity indicates that the evolution of the birefringence is the same for both FOB and ZOB beams. The theoretical fit from expression 3.2 is also shown to emphasize the quality of fit. Based on these results only the ZOB intensity will be shown for the other two samples.

The intensity data for the KTN27 sample are shown in figure 4.5(a). These results display very similar features to those in KLTN15 and certain notable differences. The similarities include both the temperature independence of the total intensity value and the steady change in the birefringence above T_c + 40 K, the general profile of the temperature dependence of the dielectric constant and the $I_{45}(\perp)$ intensity is observed to be non-zero at all temperatures, increasing with decreasing temperature above the phase transition. The first difference is that the KTN27 exhibits Rayleigh scattering in all directions below T_c + 40 K a feature that becomes progressively more pronounced below T_c + 15 K. This Rayleigh scattering is likely due to the presence of PND's revealed in the dielectric spectrum and the effect on the total transmitted intensity is seen by the decrease in figure 4.5(a). Simultaneously, a plateau in both the $I_{45}(\perp)$ and I_{45} $(\parallel)$ components is observed at 10 to 20 K above Tc, suggesting that the temperature evolution of the birefringence has become stalled. The dielectric peak is broader with a half width at half max of 7.8 K versus 3.9 K for the KLTN15, suggesting that the PND's are more numerous at higher temperatures. The drop from the dielectric loss peak is also more gradual, decreasing over a 4 degree range from the transition, indicating that the transition is not as sharp and thus more disordered. This crystal was also found to reach thermal equilibrium very rapidly at all measured points, even within a few degrees of the transition, indicating that slow relaxations are not present. This further indicates that the PND's are smaller and more numerous, which explains the stronger Rayleigh scattering and faster equilibration time.

Results for the KLTN36 sample are shown in figure 4.5(b). These results are qualitatively similar to those in the other two samples in that the total intensity

values are temperature independent at high temperatures where the $I_{45}(\perp)$ component evolves slowly with temperature. KLTN36 differs from the other two crystals in several respects. Strong birefringence is already present at high temperature, indicated by the $I_{45}(\perp)$ intensity starting near a maximum value. This is followed by several oscillations with decreasing T, which indicate a much stronger temperature dependence of the birefringence. Rayleigh scattering was evident in the loss of total intensity below T_c + 40 K, but it was not as strong near the phase transition as in the KTN27 sample. Also, the transmitted beam is not completely extinguished below the phase transition but remains with a clearly defined polarization and a consistent total transmission of 15%, indicating larger or better defined domains which may explain the relatively smaller Rayleigh scattering. Lastly, while the temperature was held fixed at the transition temperature of 273 K, the dielectric constant was observed to decrease slowly, losing 90% of its maximum value over a 2 hour period. This indicated that close to the transition, the crystal required a very long time to come to thermal equilibrium. By contrast, thermal equilibrium at higher temperatures occurred in under two minutes.

Figure 4.6 shows the extracted value of the birefringence, δn from expressions 3.2 and 3.4, plotted on a log-log scale as a function of T-T_c. Upon approaching the transition temperature, the increase in the period of the oscillation indicates an increase in the birefringence exhibiting critical behavior and is therefore related to the transition. The observed behavior can be described phenomenologically with an expression usually applicable to critical phenomena as:

$$\delta n = \left(\frac{a}{(T - T_c)^{\alpha}} + c \right) \tag{4.1}$$

Where a and c are constants and α is the critical exponent. The exponent and constants were varied to find the best fit to the data using Origin 8.5 and these values are shown as solid lines in figure 4.6. δn is only a difference expression, and therefore not a direct measure of the susceptibility although there will be some correlation. The linear fit on the log-log plot shows that the two striated samples exhibit critical behavior with exponents that are smaller than the common susceptibility value of

α=1.0 from mean field theory[8, 121]. Also, the KLTN36 sample has a larger initial birefringence. The KTN 27 sample does not exhibit critical behavior and its δn becomes approximately constant with temperature below T_c + 30 K.

4.5 Discussion

We propose that the striations in KTN create both a volume phase grating from the refractive index modulation and a net strain from the lattice parameter modulation resulting in an average birefringence due to the photoelastic effect. The two main results of this study are the observation and temperature dependence of diffraction and the observation of birefringence at high temperature with its unexpected temperature evolution upon approaching the phase transition.

The strain gradient and the refractive index variation are inherently linked via the differences in the two end materials which affect the local polarizability. The $KTaO_3$ and $KNbO_3$ end materials have different unit cell sizes and refractive indices as mentioned in sections 1.1 and 3.1. Figure 4.7(a) shows that the substitution of a niobium for a tantalum will result in a larger unit cell. This induces a local symmetric strain in the surrounding lattice[50] which results in a homogeneous optical response in the average refractive index. When two Nb unit cells are close enough for their strain fields to overlap as in figure 4.7(b), the average symmetry is no longer cubic and will result in local birefringence due to the photoelastic effect as per equation 3.9[87]. However, given sufficient Nb unit cells, the lattice will be approximately cubic again as the Nb cells stretch the Ta cells as shown in figure 4.7(c) where a 40% Nb distribution is shown. Different regions or layers with different concentrations will have different average unit cell dimensions as shown in X-Ray results[15] and thus exhibit a net strain between them. Therefore a sinusoidal modulation of the refractive index as specified expression 3.6 will be correlated to a matching modulation of the lattice parameter. The dominant patterning of the strain-induced birefringence can be observed qualitatively by optical microscopy as

shown in figures 4.1(a), 4.2(a) and 4.2(b), but these figures cannot be used to quantify the refractive index patterning other than the periodicity. It should be noted that this hypothesis is different than the standard model which assumed the strain distortion was only due to the polarizability of the Nb[10].

The flux grown KTN27 sample exhibits no diffracted beams, but does have birefringence due to the Nb gradient that commonly occurs during growth of solid solutions[18]. The TSSG grown KLTN36 sample exhibits a single diffracted beam that is consistent with the two beam coupled wave theory resulting from a single cosine term in the refractive index modulation. For small input angles no birefringence is predicted by this theory[85], and thus strain must be the cause. The TSSG grown KLTN15 sample exhibits multiple beams whose output angles are consistent with the periodicity of the striations as per expression 3.7 from the multiple coupled wave theory[91]. Without a quantitative estimate of the refractive index profile, an analysis of the diffraction efficiency and correlated strain birefringence is not possible.

The birefringence, dielectric and diffraction results do however reveal the physics of the respective phase transitions. For temperatures above T_c + 40 K, the crystals are on average cubic with either a gradient or modulation in both the refractive index and lattice parameters which are the dominant pattern. As is common in in many materials, a temperature decrease results in a change in the lattice parameters[15], and refractive indices[88]. This will result in a change in the strain mediated birefringence of expression 3.2 via the optical path length, and effective refractive index. This is observed in figures 4.4(c), 4.5(a) and 4.5(b). The KTN27 sample displays a more rapid temperature evolution in the high temperature region as seen in figure 4.6 despite the absence of striations.

Below T_c + 40 K, the precursor tetragonal phase transition begins in nano-scale local regions, or PND's, where the Nb concentration is greatest. The $KNbO_3$ unit cells act as nucleation sites for the PND's, which grow with decreasing temperature and have inherent uniaxial refractive indices with lower values along the c axis relative to the a or b axes of the crystal[2]. The pattern of how this is accomplished is not yet clear, but is reasonable to assume that the phase transition and associated

PND formation will begin in the Nb rich layers and influence the orientation of the subsequently forming PND's in the lower concentration layers. Each PND will change its local strain field to reflect its new, localized tetragonal structure. The PND orientation is expected to be random[122], but the pre-existing macroscopic strain from the concentration modulation couples to the precursor PND's and preferentially orients their c-axis direction along the principal strain axis. The presence of the PND's have several observable effects which support this hypothesis. The dielectric constant is known to increase with the increasing number and size of the PND's and this is observed directly in figures 4.4(c), 4.5(a) and 4.5(b). The net birefringence is observed to increase by addition of the inherent uniaxial indices of the PND's which grow in size and number and a relatively larger proportion are oriented to the c-axis. The local strain field of the PND's also causes Rayleigh scattering in all samples[114], occurring at higher temperatures above T_c with increasing Nb concentration as seen by the loss of total intensity in figures 4.5(a) and 4.5(b). This intrinsically uniaxial PND strain field then obscures the volume, or extrinsic, refractive index modulation in the KLTN15 sample, effectively creating an optically homogeneous uniaxial sample. This result is consistent with the observed directional changes in the measured Young's modulus of KTN16% [111], where the modulus was larger in the (001) direction at T_c + 150 K but more uniform in all other directions at T_c +1 K.

The failure of the KLTN15 and KLTN36 samples to show a distinct change at T^* in figure 4.6, other than the loss of intensity seen in figure 4.5(b), indicates another factor besides the strain. The KTN27 sample reveals the PND onset with an inflection point at T_c + 40 K where the birefringence becomes relatively constant with temperature. KTN has only been reported to exhibit dielectric aging[117] under application of a electric field but not under zero field cooling conditions. The KTN27 sample reached a dielectric equilibrium immediately at all temperatures, including the phase transition temperatures where the dielectric constant was seen to decrease. In contrast, aging is well known in KLTN[123], and is indicated by the equilibrium time scale of the dielectric data close the phase transition for both

KLTN samples in this study. The KLTN15 sample needed 30 minutes to equilibrate near T_c, while the KLTN 36 phase transition was completed over a 2 hour period at a single critical temperature where the transition began spontaneously. This time dependent transition appears to indicate slow growth of domains that coalescence into larger domains and reduce the amount of light scattered compared to the KLTN15 and KTN27 samples. This aging would also allow the PND's more time to orient to the macroscopic modulated strain pattern. Also, the presence of the Cu[116] and Li[124] impurities are known to result in additional low frequency relaxation modes in the dielectric spectrum that follows a Vogel-Fulcher-Tamman (VFT) temperature dependence. This VFT behavior was suggested to originate from coupling between the Cu, Li and Nb atoms resulting in a percolative type phase transition with a first order character in the temperature range between T_c and T_c + 20 K. Although the KLTN36 had stable values when the dielectric constant was measured at temperature away from T_c, the presence of the symmetry breaking defects of Cu,Li and V may have allowed larger domains to form while the temperature was changed. These additional dopants, in combination with the relatively stronger striation patterns in the KLTN15 and KLTN36 samples, result in the critical character of the phase transition. The lack of a strong strain pattern and additional polar constituents in the pure KTN27 sample did not allow a smooth continuation of the temperature evolution.

Below the transition, the measurements show that all polarization information was lost, and the beam was completely scattered by the KLTN15 and KTN27 crystals, while the KLTN36 sample still had a 15% light transmission below T_c. The structural birefringence and electro-optic coefficients in KTN in the lower symmetry phases are also known to display very pronounced temperature dependence[6], indicating that the domains still have strong elastic components that are evolving with temperature or time.

The complex nature of these transitions, combining strain and precursor uniaxial PNDs with various dopants, suggests the use of the modified phenomenological expression 4.1 for the birefringence that is characteristic of critical phenomena as shown figure 4.6. The fit obtained is quite good, and can explain the very rapid

oscillation of the transmitted intensities $I_{45}(\perp)$ and $I_{45}(\parallel)$ close to the transition for both striated samples. Per Cowley[125], the susceptibility is directly linked to the evolution of the order parameter through changes in the polarizability, and this parameter can be coupled to the elastic coefficients with a phenomenological Landau theory. As the elastic coefficients have also been shown to be strongly temperature dependent[111] in the PND temperature range, the piezoelectric and elastooptic coefficients are also assumed to be temperature dependent. Thus, the exponents of α =0.315 and 0.408 governing the change in birefringence are different from the exponents expected for critical behavior of the susceptibility from the phenomenological Landau theory[8, 121] which has α=1.0. This difference may be due to the higher order nature of combined piezoelectric and elastic-optic effects in a disordered system with inherent strain fields.

4.6 Conclusion

In a striated KTN crystal, niobium concentration modulations are responsible for both diffraction and volume birefringence at high temperature in the cubic phase. Both the transmitted and diffracted beams are shown to exhibit the same birefringence. The clearer the striations or the stronger the contrast, the stronger the observed diffraction and the larger the critical behavior near the transition. As temperature decreases, the diffraction efficiency decreases while the overall measured birefringence concurrently increases, particularly below Tc+40K when polar nanodomains appear which also give rise to an increase in the dielectric constant. The combined decrease in diffraction efficiency and increase in measured birefringence indicate that the appearance of PNDs introduces a microscopic intrinsic birefringence that eclipses the strain induced volume birefringence observed at high temperature. This microscopic birefringence can be formally described by a critical-like function of $(T\text{-}Tc)^{-\alpha}$, i.e. it increases progressively faster upon approaching the transition from above. Below the transition, polarization information was lost except for the highest niobium concentration sample of 36% which retained some polarization information,

indicating a more homogeneous transformation.

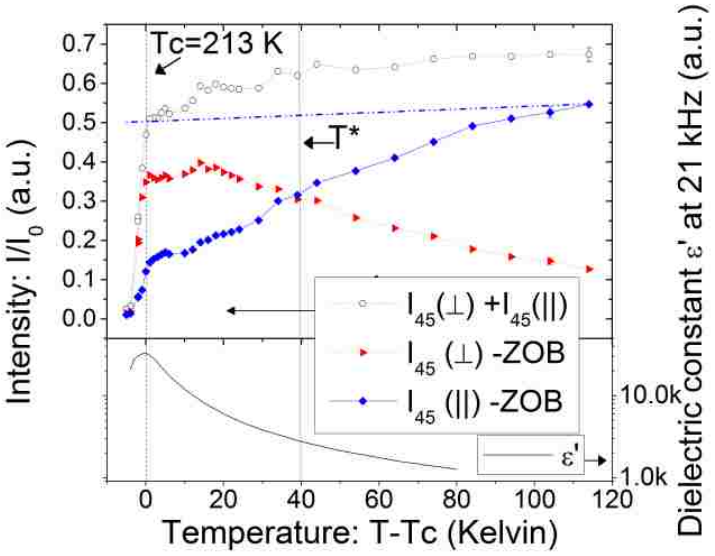

(a) KTN27

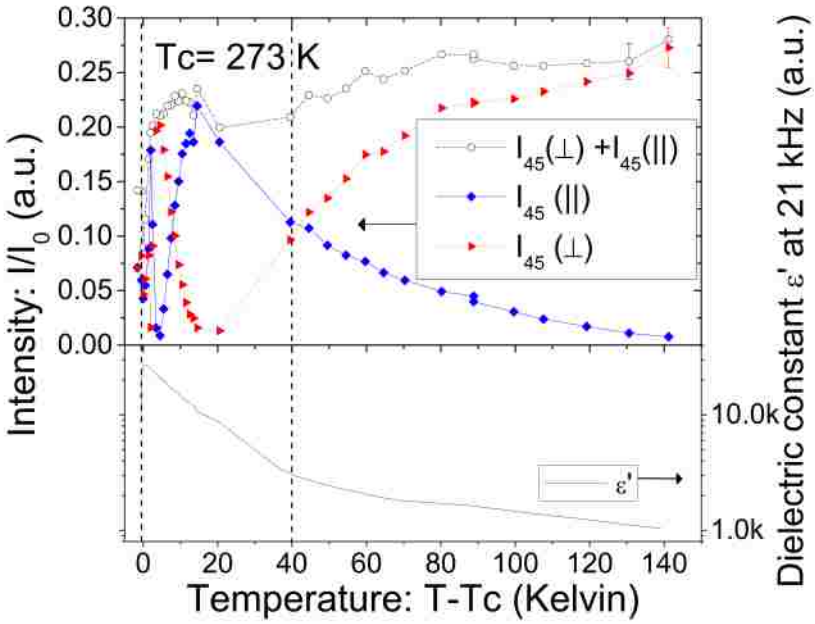

(b) KLTN36

Figure 4.5: KTN27 and KLTN36 birefringence and dielectric data. The KTN 27 optical rotation stops near T_c + 20 K while the KLTN36 shows several rotations.

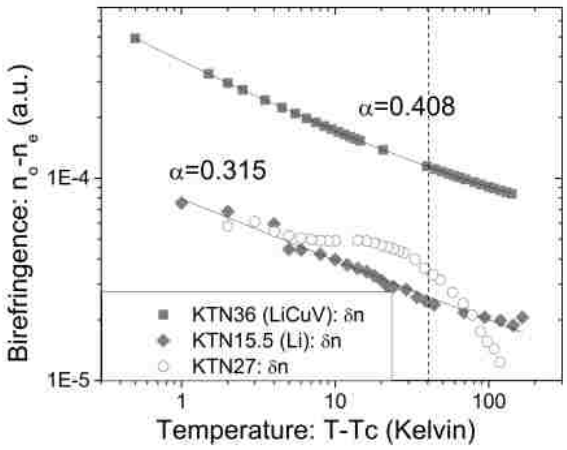

Figure 4.6: Comparison of the effective birefringence fits as calculated from equation 4.1. The strongly striated, Li doped samples show critical behavior, while the KTN27 sample temperature evolution becomes static below Tc + 40 K.

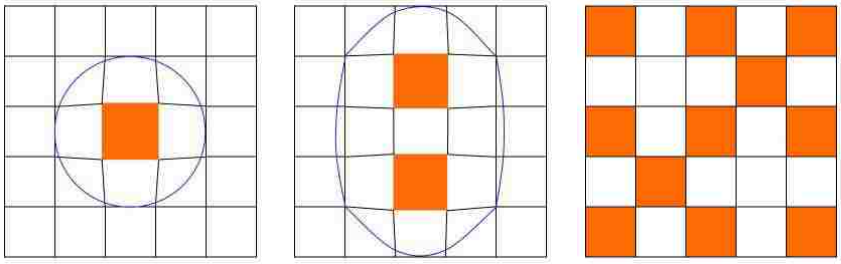

(a) Single Nb unit cell. (b) Two Nb unit cells (c) Many Nb unit cells.

Figure 4.7: Local strain fields due to lattice mis-match of end materials

Chapter 5

Raman scattering in solids

5.1 Fluctuations and time correlation functions

The description of the fluctuation dissipation theorem presented here follows the presentation given by Berne and Pecora[126]. The atoms in ionic crystals such as perovskites are in constant motion due to thermal interactions with the lattice heat bath vibrations. This motion can be translational, rotational or oscillatory in nature and each type of motion will be apparent in the resulting interaction with the incident light wave. The fluctuations are considered as dissipative as they both add to and remove energy from the incident beam of light and therefore contribute to the imaginary part of the susceptibility. This can be understood from conservation of momentum[127] where the material loses or gains a momentum $\hbar\mathbf{q}$ when the incident photon of momentum $\mathbf{k_I}$ scatters from an atom in motion:

$$\begin{aligned} \mathbf{q} &= \mathbf{k}_I - \mathbf{k}_S \\ \mathbf{q}' &= \mathbf{k}_I + \mathbf{k}_{AS} \end{aligned} \tag{5.1}$$

The designation S represents Stokes scattering where the photon loses energy and AS designates Anti-Stokes scattering from a gain in energy. This can also be considered as annihilation and creation operations on the incident photon. Because of the energy transfer, they are identified as the imaginary components of the inelastic

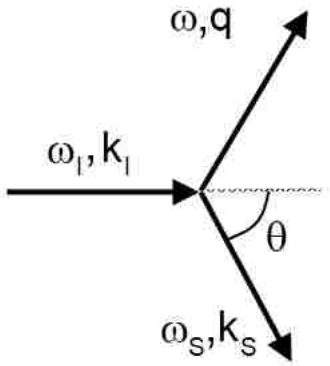

(a) Stokes Scattering

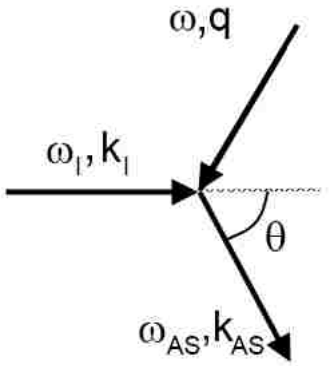

(b) Anti-Stokes Scattering

light scattering spectrum, while any scattering that does not involve a change in energy is referred to as the elastic or Rayleigh scattering. This is shown schematically in figures 5.1(a) and 5.1(b).

It is possible to define this atomic motion as a deviation of the atom from its average equilibrium position:

$$u(\mathbf{q},t) \equiv x(\mathbf{q},t) - \bar{x} \tag{5.2}$$

where u is the magnitude of the deviation from the average position $\bar{x}$ and can be either positively or negatively valued. These motions can be described as having a time average:

$$\bar{u}(\mathbf{q},t_0,T) = \frac{1}{T}\int_{t_0}^{t_0+T} dt' u(\mathbf{q},t') \tag{5.3}$$

Where t_0 is the initial time and T is the time interval. If this average displacement is independent of t_0, it is called a stationary property and in the limit as T approaches infinity it is expressed as:

$$\langle u \rangle = \lim_{T\to\infty} \frac{1}{T}\int_0^T dt' u(t') \tag{5.4}$$

Note the absence of the variable $\mathbf{q}$ for visual clarity. In general, these displacements will not be similar in time, i.e.: $\langle u(t)\rangle \neq \langle u(t+\tau)\rangle$. If the time interval

between measurements, τ, is short enough relative to typical fluctuation times, then there is a correlation where $\langle u(t+\tau)\rangle$ is close to $\langle u(t)\rangle$. This is known as the autocorrelation function and is described as:

$$\langle u(0)u(\tau)\rangle = \lim_{T\to\infty} \frac{1}{T}\int_0^T dt' u(t')u(t'+\tau) \tag{5.5}$$

The integral can be approximated as a sum and since the elements will be both positive and negative, it is clear that

$$\sum_{j=0}^{N} u_j^2 \geq \sum_{j=0}^{N} u_j u_{j+n} \tag{5.6}$$

or equivalently:

$$\langle u(0)^2\rangle \geq \langle u(0)u(\tau)\rangle \tag{5.7}$$

This states that it is possible for a displacement to remain equal to its initial value for all times τ indicating that u is a conserved quantity. Alternately it can decay from the initial value and this distinction fundamentally separates the relaxations from the oscillatory behavior of NBT. The decay can take the form:

$$\langle u(0)u(\tau)\rangle = \langle u\rangle^2 + (\langle u^2\rangle - \langle u\rangle^2) exp^{\left(\frac{t}{\tau_R}\right)} \tag{5.8}$$

where τ_R is the relaxation time. There can be one or many relaxation times depending on the physical properties of the material system in question. It should be recognized that this formalism is quite general, applicable to any variety of displacement related sources: thermal, dielectric, elastic or some other thermodynamic property of the system. The relaxational motion in NBT corresponding to this displacement is observed in the central peak portions of the spectral profile. In the frequency domain, the Lorentzian shape is the Fourier transform of the exponential term $e^{\left(\frac{t}{\tau_R}\right)}$. The physical origin of this displacement must be understood in the context of the known material properties and by direct comparison to other similar materials.

The oscillatory atomic motion follows the familiar example of a simple harmonic oscillator[127], a model commonly used as a first order approximation, where the

equation of motion can be represented as:

$$\ddot{u}_i + \Gamma_i \dot{u}_i + \omega_i^2 u_i = F e^{i\omega t} \tag{5.9}$$

where u_i again represents the displacement, ω_i is the natural frequency and Γ is the damping constant for each of the i^{th} modes. F is the amplitude of an external driving force with frequency ω. It is well known from mechanics that the steady state amplitude of this model when u is defined as $u_i = u_{0i} e^{i\omega_i t}$ is:

$$u_{0i} = \frac{F}{(\omega_i^2 - \omega^2 - i\omega\Gamma_i)} \tag{5.10}$$

It is also known that oscillatory vibrations of this type correspond to normal vibrational modes of the crystal that are called phonons. Phonons are bosons and their population density is directly dependent on the ambient temperature of the material[128]. The thermal scaling factor is denoted:

$$n(\omega_i) = \frac{1}{e^{\frac{\hbar\omega_i}{k_B T}} - 1} \tag{5.11}$$

Where k_B is the Boltzmann constant, T is the temperature. $n(\omega_i)$ scales the Anti-Stokes spectrum, and $n(\omega_i)+1$ scales the Stokes portion of the spectrum. A useful technique to determine the internal temperature of the crystal is to take the ratio of the Stokes spectrum versus the Anti-Stokes spectrum and the resulting slope will be dependent only on temperature:

$$\frac{I_{STOKES}}{I_{ANTI-STOKES}} = \frac{\omega_S^4}{\omega_{AS}^4} e^{\frac{\hbar\omega_i}{k_B T}} \tag{5.12}$$

The relationship between the scattered light and the atomic displacement can be understood in the following way. The spectral density, or intensity as a function of frequency, is defined as the Fourier transform of the time correlation function:

$$I_u(\omega) \equiv \frac{1}{2\pi} \int_{-\infty}^{+\infty} dt e^{-i\omega t} \langle u^*(0) u(t) \rangle \tag{5.13}$$

The connection to the scattering of the electric field of a laser comes through the polarization, which is the the physical response of a material to an applied electric field:

$$\mathbf{p} = e\mathbf{u} = \overleftrightarrow{\chi_{ij}} \mathbf{E_j} + \frac{\overleftrightarrow{\chi_{ij}(\omega_I)}}{\delta u_q^*} \mathbf{u(t)} \mathbf{E_j} \tag{5.14}$$

e is the electrical charge of the atom, χ_{ij} is the susceptibility tensor, and $\mathbf{E_j}$ is the electric field vector, commonly described as $\mathbf{E} = E_0 e^{i\omega t}\hat{e_j}$ with $\hat{e_j}$ representing the unit vector parallel to the field and E_0 as the amplitude. The first term represents the linear first order oscillations that are at the same frequency as the incident electric field. The second term includes displacements whose time dependence are based on the material characteristics such as the symmetry and local potentials and the susceptibility derivative with respect to position. However, because of the ionic nature of the perovskites, dynamical displacements result in changes in the local dipoles and thus changes in how the material responds to the applied electric field. As a result of the time dependent electric field of the laser interacting with the local dipoles, the scattered light intensity is expressed as:

$$\bar{I_S} = \sum_{i=1}^{N} \int d\Omega \int d\omega_S \omega_S^3 V A \langle u(\mathbf{q},t)_i u^*(\mathbf{q},t)_i \rangle_{\omega_S} \tag{5.15}$$

Where $A=\frac{n_S|\epsilon_0 e_S^i e_I^j \chi^{ij}|^2}{(4\pi\epsilon_0)^2 c^4 n_I}$ is a constant of the applied electric field with χ^{ij} as the susceptibility tensor. The refractive index, n_I, unit vector, e_I^j, and frequency, ω_I, are associated with the incident laser field, while the corresponding n_S, e_S^i and ω_S are associated with the scattering field. Also, c is the speed of light, ϵ_0 is the permittivity of free space, V is the scattering volume, and $d\Omega$ is the solid angle. It should be noted that the $\langle u(\mathbf{q})_i u^*(\mathbf{q})_i \rangle$ term will include the Bose thermal population factor for phonon modes but not for relaxational modes. This will be further described in section 6.6. Further details of the derivation of this equation can be found in the excellent book by Hayes and Loudon[127].

5.2 Correlation method of mode determination

An important aspect of Raman spectroscopy is the determination of how many modes of what symmetry are expected in a given structural phase. Kreisel et al.[129] and Petzelt et al.[130] did not agree on the number of modes for the low symmetry R3c phase in NBT, reporting $7A_1$ + 6E and $4A_1$ and 9E respectively. It is not possible to use polarization to distinguish between these two assignments due

Space group	Modes
Cc	13 A' + 15 A"
P4bm	4 A_1 + B_1 + 3 B_2 + 8 E
R3c	4 A_1 + 9 E
Pm3m	No Raman active modes

Table 5.1: Raman active phonon modes in NBT

the excessive Rayleigh and Mie scattering resulting from the nano- and micro-scale polar[131] and elastic domains[132, 133]. To confirm the correct number and character of the modes, the site correlation method[134] was used. These results were checked against another well known R3c material, $BiFeO_3$[135], which has well defined and clearly characterized modes that exhibit $4A_1$ and 9E symmetries. The results shown in table 5.1 include the Cc monoclinic assignments.

Chapter 6

NBT Results and Discussion

6.1 NBT Introduction

NBT is a particularly interesting relaxor system for three reasons. First it is lead-free, with an electro-mechanical d_{33} coefficient for doped ceramics and solid solutions ranging from 125 to 2000 pC/N [40, 41] while the single crystal ones are approximately 65 pC/N[42]. It is therefore a promising material for transducer and actuator applications as this higher end value is close to that of the commonly used relaxor PZN-PT. Secondly, bismuth is one of the least toxic heavy metals. Thirdly, NBT is also interesting from a condensed matter physics point of view because it exhibits, in a single system, the two major instabilities (tilting and shifting) that are separately observed in other perovskite systems. The tilting instability involves the rotation of the anion octahedra which is known to reduce the size of the unit cell[47] in the plane of the rotation, causing local strain[136]. This tilting instability gives rise to R and M point Bragg peaks in neutron scattering spectra[19, 48] and is useful in describing the elastic domain ordering. A recent review of NBT[137] discusses the local elastic organization at several length scales: 1-2 nm platelets[132], nanometer scale twinning and micrometer scale domains[131]. These can be considered as the chemically ordered regions[66] or chemical nano regions (CNR's)[27] commonly associated with relaxors. The dynamical behavior of these elastic domains are not well understood,

but the slow nature of the phase transitions seen in X-Ray[61] suggest there may be a time dependency of an elastic nature. This non-polar tilting instability is also found in fluoro-perovskites such as $RbCaF_3$ [138] and $KMnF_3$[139] as well as oxides such as $SrTiO_3$ [140], which provide useful comparisons. The shifting instability is due to cation displacements which are assumed to have polar character due to the aliovalency of the cations. The cations have been shown to be off center from their equilibrium sites at all temperatures [19], but recent work in NMR[28] suggests that the Na^{1+} ions have multiple potential well sites in the <111> directions similar to the Pb based relaxors[27]. The cation local mobility is confirmed by the appearance of the characteristic frequency dispersion of the dielectric constant typical of relaxors[141]. Nanoscale local regions with polar ordering are known as polar nanodomains (PND's), and their dipole re-orientation is understood to be the origin of the relaxor behavior in NBT. The displacement direction[19] in NBT is consistent with recent theoretical work on A-site disorder in multiferroic materials[29, 30] where the cations are shown to displace in the <111> directions, but the nature of the coupling between the A-site cations and the TiO_6 octahedra rotation is poorly understood and still a topic of active research[27, 142, 143]. These PNRs can be expected to contribute to the dynamical properties if local cation re-ordering results in a time dependent shifting of the cations in the adjacent unit cells, effectively a slow cascading of disorder which may explain the slow time dependent evolution of the dielectric constant[61].

NBT undergoes two separate transitions, a high temperature transition at $T_{c1}=\sim$ 820 K, from a cubic, paraelectric, paraelastic $Pm\bar{3}m$ phase [19, 144] to tetragonal P4bm, and a second lower transition around $T_{c2}=\sim$ 570 K to either a rhombohedral R3c or a monoclinic Cc phase[145, 146]. The onset of M and R point Bragg peaks in the Brillouin zone[48] are considered the order parameters for these transitions. The onset of these Bragg peaks are abrupt in the phase transitions of NBT like a first order transition as described in section 1.3. The higher temperature transition also has anti-parallel cation displacements[19] and anti-ferrodistortive rotations of the anion octahedrons[48] as shown in figures 1.3(b), described in Glazer[47] notation as $a^0a^0c^+$. The lower temperature transition is a ferroelectric one, corresponding

to both $a^-a^-a^-$ octahedral tilts as shown in 1.3(c) and parallel cation [111] displacements. The distortive domains in NBT are observed in neutron[48], X-ray[20], and electron diffraction[132], while polar behavior that is commonly associated with PNR's are observed in dielectric measurements[141]. The presence of both rotational distortive and polar domains is another unique feature of NBT that is not commonly found in other perovskites. As the lower temperature phases are not subgroups of the higher temperature phases[44], which is also characteristic of first order transitions, it is unclear what the nature of the transitions should be[58] in terms of displacive and order-disorder. The Raman active soft mode in NBT was reported to have a linear ω^2 vs. temperature dependence[83] based on the softening of the broad peak at 50 cm^{-1}, but this is inconsistent with the known first order character of the phase transitions and the linear temperature evolution of the dielectric constant at low temperature. Neutron studies have observed modes described as soft modes[72, 73], but there is insufficient detail to conclusively determine which transition they originate from. The phase transition sequence in NBT is unique among the ferroelectric perovskites as there are no other materials known that transition in the same manner[56]. The results cited suggest that both transitions are not purely polar or purely structural but have mixed characters, with strain and polarization coupled and competing [83, 147, 148]. Similarities have in fact been noted between NBT and two other well-known relaxors, $PbMg_{\frac{1}{3}}Nb_{\frac{2}{3}}O_3$ (PMN) [83] and $K_{1-x}Li_xTaO_3$ (KLT) [149] in which both polarization and strain play important roles.

NBT also exhibits many of the standard relaxor characteristics described in section 1.5. It has the typical frequency dispersion of the dielectric constant[141] with peaks far above the AFE-AFD high temperature transition, thus indicating PNR's several hundred degrees above T_{c1}. There is an "S" shape or slim profile in the polarization hysteresis curve[150] near the lower phase transition temperature. The abrupt spontaneous polarization onset[141] is consistent with a first order transition, but the optical birefringence associated with it is unusual in that it has a hysteresis spread over several hundred degrees[150]. Based on these observations, NBT is a typical example of a relaxor ferroelectric. However, there are unusual

features to the dielectric spectrum. The dispersion is continuous through the transition near T_{c1} and exhibits a maximum in the lowest frequency dielectric constant closer to T_{c2}[141]. Below T_{c2}, NBT becomes ferroelectric and no longer exhibits relaxor behavior with frequency dispersion[141, 151]. When measured while drifting the temperature, the dielectric constant around this lower transition exhibits a thermal hysteresis due to the coexistence of both phases[61]. The temperature evolution of the dielectric maxima at the various T_m's were shown to follow a Curie-Weiss law for a 125 dipole cluster[141], but any deviation of the inverse dielectric permittivity from a linear temperature dependence has not been shown. Dielectric studies in NBT are unclear with respect to behavior near the expected quasi-static PND region below T^* and this temperature has not been reported as such. There are reports of an Arrhenius temperature dependence of the dielectric constant for ceramics[152], some single crystals[141], but not others[153], and Vogel-Fulcher for Ba doped samples[154, 155]. The dielectric constant is also reported to contain multiple components due to a combination of ionic conductivity and the polarization response of bound charges[141]. Due to the known aging characteristics[60, 61], dielectric spectra should be referred to with caution.

Raman spectroscopy is a very useful tool for the study of both the lattice dynamics of the phonons and the local dynamics of the PNDs in relaxors. Based on the symmetry selection rules for phonons, it also provides structural information about local symmetry changes and phase transformations. In ferroelectrics, particularly relaxors, one can distinguish between two main sections of the Raman spectrum, high frequency and low frequency. Above approximately 100 cm^{-1}, the hard phonon modes correspond to more local vibrations involving specific atoms and molecular bonds in the unit cell, and their frequencies are usually not strongly temperature dependent. At frequencies below 100 cm^{-1}, the spectrum usually contains contributions from more collective modes such as the soft optic phonon, acoustic phonons and local relaxations that may be coupled to these phonons. These low frequency excitations are more difficult to study, first because they are close to the intense Rayleigh line and, secondly, because their respective contributions overlap significantly in the frequency spectrum. The low frequency range of the Raman spectra

of relaxors and other disordered systems undergoing phase transformations is often dominated by a 'Central Peak' associated with relaxing fluctuations or precursor dynamics of the lower temperature phase. In relaxors such as NBT, the CP associated with these relaxations can extend significantly beyond 100cm^{-1}, overlapping some of the higher frequency phonons.

Several Raman studies of NBT have already been reported on ceramics [130], pure crystals, [82, 83, 156–158] and powders under high pressure [129, 144, 159, 160], but there still are many unresolved questions. The correct symmetry of the low temperature phase[145] and thus the total number of phonon modes associated with it, the correct temperature evolution of the soft mode, the number and origin of the CPs, and the inconsistencies in the temperature dependence of the intensity[157, 161] are all still open questions. The previous NBT Raman studies most relevant for the present work are those of the higher frequency region of the spectrum by Kreisel et al.[129] and Luo et al.[157] and the lower frequency region by Siny et al.[83] As already mentioned, because of the overlap of features in different regions of the spectrum, especially the CP, it is important when deconvoluting the spectra to include all peaks present rather than analyze them separately. In the present paper, we have measured full spectra up to 1000 cm^{-1} over the entire temperature range from 1000 K down to 80 K and have performed a comprehensive analysis over the entire spectral range. Based on this analysis, we describe the quantitative evolution of the different low frequency modes, propose an interpretation of the transitional behavior of NBT and examine its concordance with earlier interpretations. Our results reveal the existence of two CP's, a narrow one and a broad one, and their respective temperature evolution provides information on the pretransitional or precursor dynamics of NBT and the nature of the two transitions.

6.2 Fluorescence

When undertaking any Raman measurements a standard procedure is to first determine the presence and possible effects of fluorescence peaks. These can be easily

discerned at low temperatures, $\leq$ 80 K, when full range spectral measurements are obtained with two or more excitation frequencies and compared. The fluorescence results at 80 K are shown in figure 6.1. Four excitation wavelengths were used, 514.5, 488.0 and 457.9 from the Ar laser, and 442.1 from the HeCd laser. There are two fluorescence peaks observed, clearly distinguished from the Raman peaks as they do not shift with different excitation frequencies. The weak broad peak, best observed with the 442.1 nm excitation, is centered at 500 nm and the intense narrow peak is centered at 760 nm. Together, these can be fit with a Fano line shape[162], suggesting they are coupled, but the nature and origin of the larger peak is not of interest to this investigation. The broader peak completely underlies the Raman spectra obtained at 514.5 nm but is 350 times smaller in magnitude and therefore cannot be useful in fitting. Similar to fluorescence observed in $PbTiO_3$[163], $SrTiO_3$[164] and $CaTiO_3$[165], which were attributed to oxygen vacancies, this broad peak amplitude is dependent on the annealing history of the sample, becoming larger when annealed in vacuum. However, based on the small relative amplitude compared to the Raman spectra after either air or vacuum annealing, the fluorescence contribution is ignored.

6.3 Absorption

A slight darkening of the crystal from a light yellow to a burnt amber color was observed after exposure to laser powers greater than 10 mW and at temperatures above 570 K. Any combination of an incident laser at any power with an applied electric field at temperatures above 570 K darkened the crystal completely to a black color. Application of the laser alone darkened the crystal proportionately to the incident power, increasing with repeated heating cycles. As expected, the Raman signal amplitude was inversely proportional to the darkening, nonexistent when completely darkened. Annealing in air at 600K for 1 hour was found to bleach the crystal and restore its transparency. The darkening and bleaching is illustrated in figure 6.2(b). Based on these results, each measurement cycle was begun after an

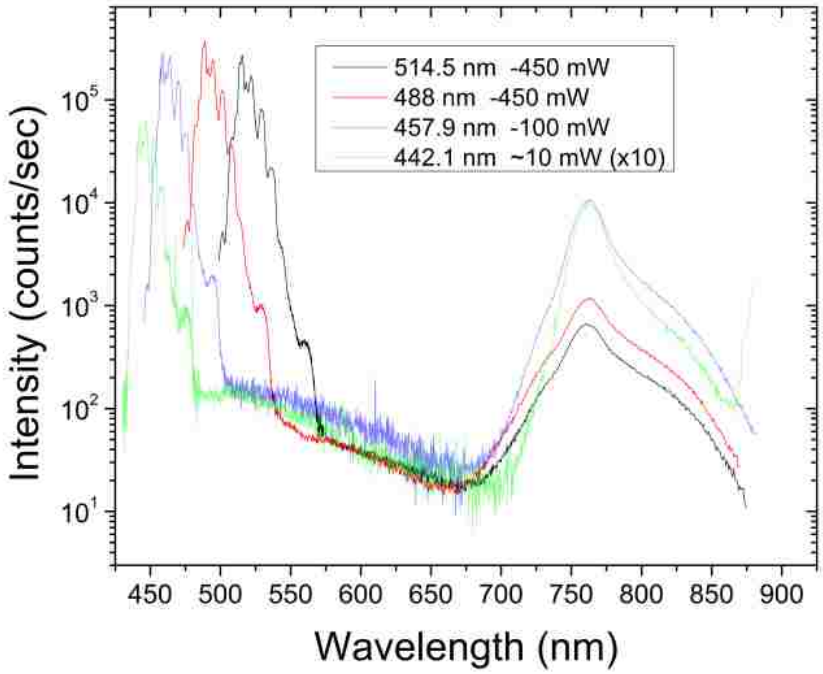

Figure 6.1: Fluorescence peaks observed with 4 excitation frequencies.

air anneal at 600 K, in the tetragonal phase, in order to obtain the largest Raman signal possible and all measurements shown in the paper were made with a low laser power of 10 mW. Since it has not been uniformly reported by all authors, we must conclude that such darkening depends on the particular crystal studied[82, 151, 157] and the crystal thermal history.

This darkening was further investigated by measuring the optical absorption over a wide range of frequencies with a Perkin-Elmer Lambda 9 spectrophotometer. Figure 6.3 shows an optical density profile of NBT after annealing in air, and this result is qualitatively similar to the as-received samples from the crystal provider. Two absorption peaks, both with a Gaussian profile, are seen between 440nm and 520nm, which is different than the previously published results[42, 166]. Exciting the samples with wavelengths shorter than the peak centers (467, 488, and 501 nm) resulted in fluorescence making the Raman anti-Stokes intensities anomalously larger than the Stokes ones. In order to minimize any fluorescence contribution to

(a) Before experiment

(b) After experiment where 500 V/cm field is applied above 570 K

(c) After air anneal at 600 K for 30 minutes

(d) After air anneal at 600 K for 90 minutes

Figure 6.2: Darkening seen in NBT crystals and results of annealing. Penny is shown for size reference.

the Raman profiles, all measurements were therefore made with the 514.5 nm line of the laser. The absorption spectra was obtained to determine the best excitation source that would have the least fluorescence contribution to the Raman spectra.

6.4 Laser Heating

Both Stokes and anti-Stokes spectra were taken at all temperatures in order to determine the precise internal temperature of the crystal and compare it to the measured PT100 sensor temperature using equation 5.12. The results of this analysis are shown in figure 6.4 and they reveal substantial thermal heating at a low sensor temperature of 80 K for all laser powers above 2 mW but above 300 K where the laser heating contribution was negligible compared to the thermal heating from the cryofurnace. The apparent failure of the temperature difference to approach zero as the power approaches zero is anomalous but appears to be independent of temperature and may be due to a frequency independent background noise that would skew the evaluation of the internal temperature. Corrections for the spectrometer grating efficiency and PMT quantum efficiency were taken into account but did not

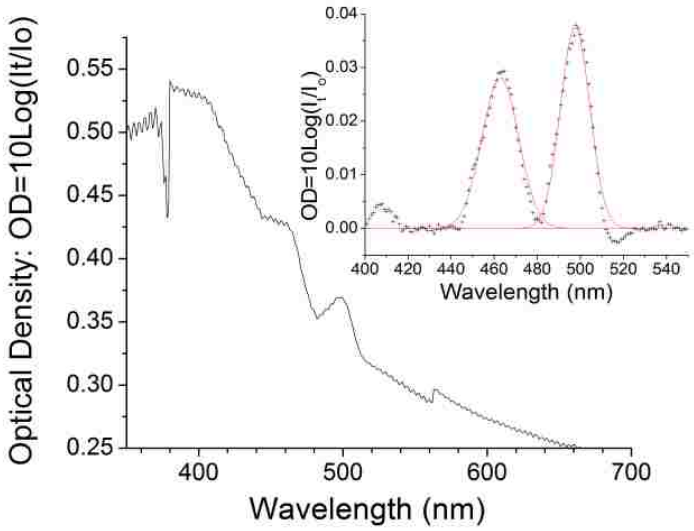

Figure 6.3: Absorbance measurement of NBT immediately after annealing the crystal in air at 600 K on a hot plate. The inset shows the two Gaussian peaks at 463 nm and 498 nm which remain after subtraction of the background from the UV resonance.

resolve the difference. Despite variations in the Stokes/Anti-Stokes ratios, the spectral profiles at each temperature were relatively consistent, staying within 5% of the original value over 8 hours of continuous laser exposure. Based on these observations the listed temperatures on all subsequent figures are the sensor temperature of the PT100 platinum sensor. It should also be noted that precise temperature values are not critical for this study as the main focus is on the progressive temperature evolution of the profiles through each of the three crystal phases.

6.5 Raman Results

Raman peaks, once they have been distinguished from the fluorescence peaks, can be used to determine or verify the structural symmetry. The number of modes, position and width can all provide useful information, particularly if they are examined as

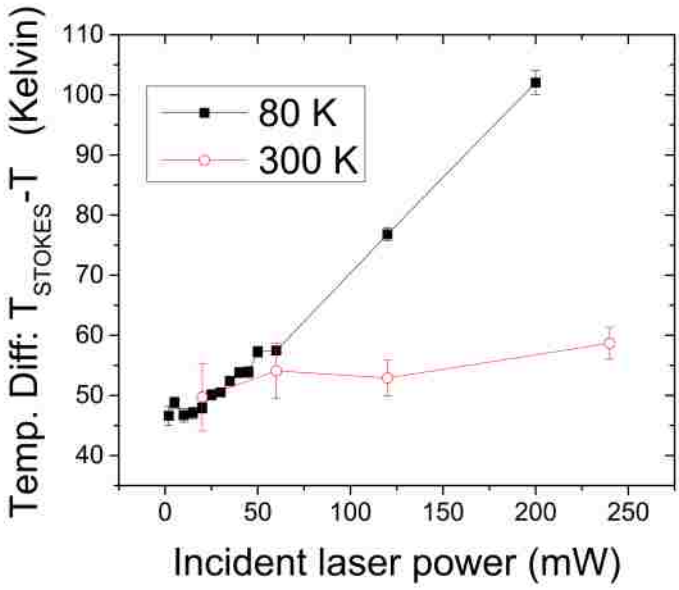

Figure 6.4: Analysis of the variation of actual crystal temperature as determined by the Stokes ratio temperature from the measured sensor temperature. 80 K and 300 K data are shown with error bars.

a function of temperature. The temperature evolution of the low frequency modes can often confirm the nature of the phase transition, i.e. whether it is first or second order for instance. Raman measurements were obtained from -100 to + 1000 cm^{-1} and from 1000 K down to 80 K, deconvoluted and compared to other materials with similar phase transition characteristics.

Figures 6.5(a) and 6.5(b) show the unpolarized Raman spectra of NBT measured at different temperatures upon cooling from 1000 K. In these spectra, one can distinguish the high frequency peaks above $\sim$100 cm^{-1} from the low frequency ones, including two CPs and a composite phonon peak centered near $\sim$50 cm^{-1}. The evolution of the central intensity is highlighted in figure 6.5(a), where two CPs are observed around zero frequency, one narrow and the other very broad, extending past 300 cm^{-1}. The narrow CP is small in the 1000 K spectra, but increases

steadily in strength with decreasing temperature to a maximum amplitude at 600 K, decreases below and has largely disappeared at 80 K. The broad peak is the dominant feature at high temperature, but progressively disappears below ∼550 K while several low frequency phonon peaks become apparent at ∼20, ∼35, ∼50 and ∼70 cm^{-1}, as determined from the fits below. The Rayleigh peak is seen at the center of the spectrum, indicated by the abrupt rise in intensity. The high frequency first order phonon peaks above 100 cm^{-1}, shown in figure 6.5(b) are already observable at 1000 K, possibly due to the precursor regions of the P4bm space group[21, 167]. Upon cooling below 550 K, these peaks develop structure, i.e. multiple components, and the positions appear to shift towards higher frequencies as indicated by the vertical lines. This shift is due to the unequal growth of the different underlying component peaks[157].

Figure 6.6(a) shows the total integrated intensities as a function of temperature upon heating from 200 K or cooling from either 800 or 1000 K. The difference in the curves, while striking, are also reported for other NBT crystals during cooling[161] and heating[157] experiments. All results were obtained on the same sample and were broadly reproducible. The intensity differences between heating and cooling may therefore be a consequence of thermal hysteresis, darkening and intrinsic structural changes. Due to these effects, all measurements shown were made in a single direction, either heating or cooling, from the specific temperatures listed. Figure 6.6(b) shows the comparison of the non-Bose corrected integrated intensity of the full Stokes spectrum data cooled from 1000 K to the low frequency CPs from 5 to 50 cm^{-1} and the Bose corrected high frequency phonon peaks above 300 cm^{-1}. It is expected from Raman theory[168] that the intensity contribution from the phonons within a given structural phase should be constant with temperature as the Bose factor accounts for any thermal differences. The flat portion of the 5-1000 cm^{-1} curve in the tetragonal phase and the decrease at higher temperatures in the cubic phase are inconsistent with the decrease in intensity of the phonons expected due to decreasing temperatures. Correction by the Bose factor would only cause the intensity to exhibit an increase upon cooling through the tetragonal phase, a result

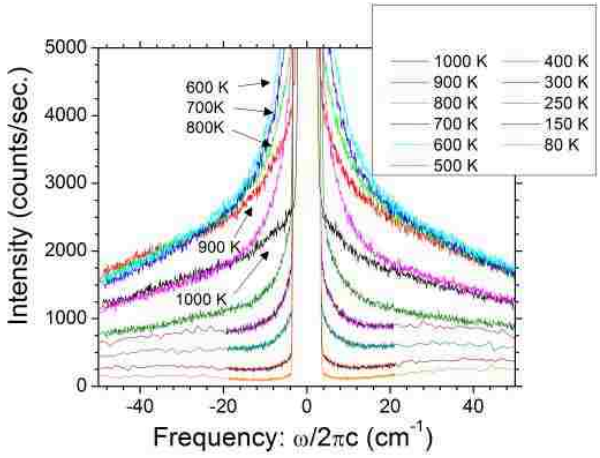

(a) Central peaks

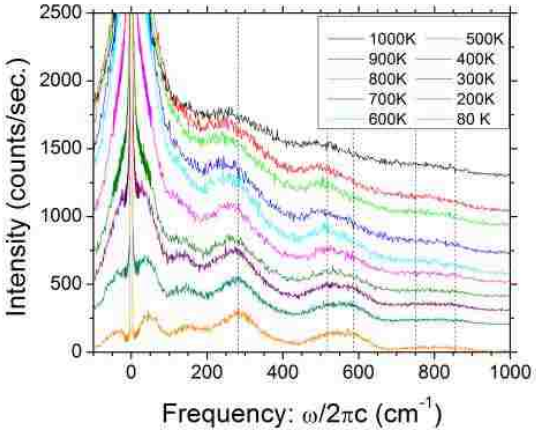

(b) Full Raman spectrum

Figure 6.5: NBT Raman spectra of different frequency regions upon cooling, with vertical lines as guides for the eye to the positions of the high frequency peaks.

that is inconsistent with the constant phonon density expected after Bose correction. The decrease in the 5-50 cm^{-1} portion of the spectrum below 600K is notably similar to that of the 5-1000 cm^{-1} curve. Since the CP's contribute most of the total intensity in this low frequency region as shown in figure 6.5(a), it is reasonable

to attribute changes in intensity to these relaxation peaks. The Bose normalized intensity above 300 cm^{-1} is flat in the low temperature phase below 300 K and from 650 to 950 K as would be expected based on Raman theory[168] per the volume component of equation 5.15, which states that the intensity is proportional to the number of scattering centers. There is an increase from 350 K to a maximum at 600 K, coincident with the temperature region of phase coexistence[61].

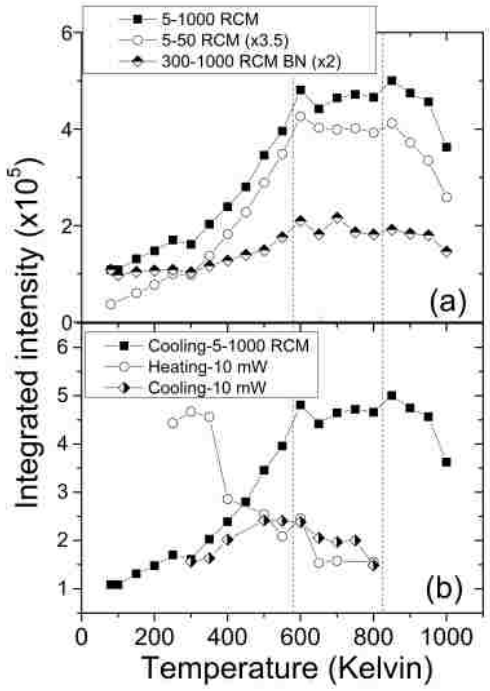

Figure 6.6: (a) Comparison of the integrated intensity of different portions of the spectrum to the total integrated intensity of the cooling scan started at 1000K, note the scaling factors in the legend. The 300-1000 cm^{-1} segment of the spectrum is shown after Bose normalization to be much less temperature dependent. (b) Integrated intensity of the Stokes portion of the spectrum for 3 scans from 5-1000 cm^{-1} upon heating and cooling. Integrated intensity is dependent on thermal history. The vertical lines indicate the nominal phase transition temperatures.

Figure 6.7 shows the ratios of the non-Bose corrected peak intensities from Fig.

6.5(b) upon heating and cooling for the primary peaks at 35 and 515 cm^{-1} relative to 295 cm^{-1}. These ratios were observed to be identical upon cooling and heating, and therefore independent of the crystal thermal history. Direct comparison of CP and phonon widths and positions between heating and cooling cycles are also in qualitative agreement, but the data is not shown. It was concluded from this comparison that the spectral profiles are the same for measurements made upon heating or cooling. It is on this basis that the peak positions and widths are analyzed for their temperature dependence, regardless of the overall absolute intensity. The 295/35 peak ratios are nearly temperature independent above 550K as seen in figure 6.7(a) but increases at lower temperatures, concurrent with the loss of integrated intensity seen in figure 6.6. This indicates that the 35 cm^{-1} peak is decreasing in amplitude with decreasing temperature as can be observed directly in figure 6.5(a). The 295/515 peak ratio shows an increase with decreasing temperature in the cubic phase (850-1000K), is flat in the tetragonal phase, and has a small but steady increase in the low temperature phase with decreasing temperature. Since apart from the usual Bose thermal population dependence, the broad CP is the spectral feature that is most rapidly changing with temperature, it is reasonable to attribute the difference in ratio behavior to the varying degrees of overlap of the CP with phonon peaks; the 35 and 295 cm-1 peaks in the spectrum will therefore be strongly affected by changes in the broad CP while the 515 cm^{-1} and higher peaks will not, resulting in a more gradual change of the 295/515 ratios. The absence of change with the 295/35 ratios in the cubic and tetragonal phases indicates that they are equally affected by the broad CP and there is little difference between them across the phase transitions. A similar analysis was performed on the data that was completely Bose corrected as shown in figure 6.8 and the analysis in which only the phonon peaks were Bose corrected as shown in figure 6.10. The results were qualitatively similar, indicating that the Bose correction is not the cause of this temperature evolution of the peak ratios. The results of the 295/135, and 295/750 peak ratios are similar to the 35 and 515 ratios and the data is not shown.

For a quantitative analysis of the temperature evolution it is important to correct the phonon part of the spectra by the Bose factor as explained in the experimental

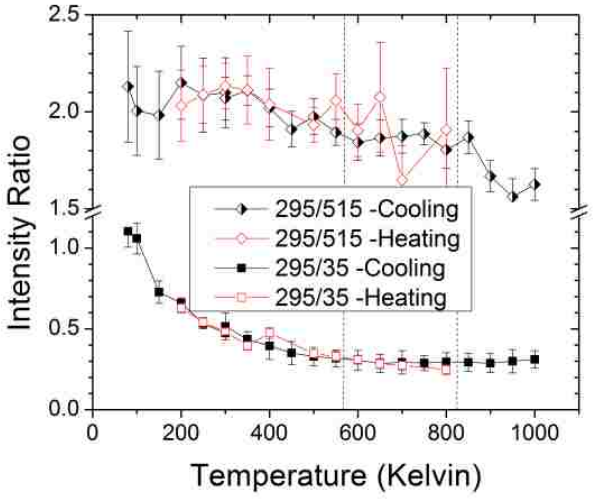

Figure 6.7: Peak intensity ratios relative to the 275 cm-1 peak using data without correction by Bose factor. The intensities used are directly read from the peaks of the measured spectra at the specified frequencies, using an average value and error which includes the adjacent 5 point values. The vertical dashed lines indicate the nominal phase transition temperatures.

section, which removes any temperature dependence related to the phonon population. To demonstrate that the CPs should not be Bose corrected, figure 6.8 shows the same data from figure 6.5(a) after Bose correction has been applied to both the phonons and CPs. The corrected total intensity exhibits a strong temperature dependence at low frequency, which is not consistent with the theory of phonon strength in a given structural phase. This result confirms the presence of additional scattering which is therefore quasi-elastic below $\sim$50 cm^{-1}, similar to Raman data in disordered glass materials[169]. The temperature dependence that remains after Bose correction must then be due to dynamical changes in the internal state of the crystal system.

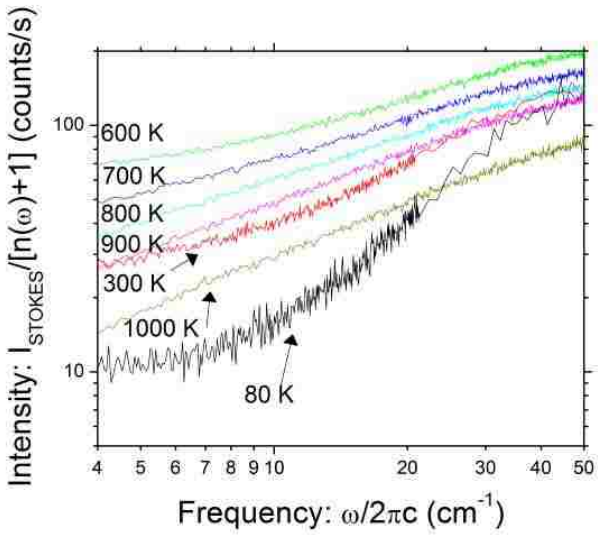

Figure 6.8: The low frequency portion the Raman spectrum after normalization of the spectra by dividing with the Bose factor:n(ω)+1. The data clearly has a temperature dependence.

6.6 Analysis

As explained section 5.1 and demonstrated in section 6.4, the generic expression describing Raman spectra in crystals is:$I(\omega) = \{ \begin{matrix} n(\omega)+1 \\ n(\omega) \end{matrix} \}\text{Im}\chi(\omega)$. In this expression, Im$\chi(\omega)$ is the imaginary part of the susceptibility and $n(\omega)$ is the Bose thermal population factor defined by expression 5.11, with $n(\omega)+1$ for Stokes processes and $n(\omega)$ for anti-Stokes processes. For phonons, the susceptibility is usually taken to be the response of a damped harmonic oscillator as per expression 5.10 and the Bose factor correction is notationally modified to be $n(\omega_{0i})$ so that the entire lineshape of each ith phonon is corrected by the same correction value[8, 127, 168]. The Raman literature commonly fits the central and DHO peaks with $n(\omega)$, which is only really appropriate for the central peak if it is considered as a distribution of many harmonic oscillators. For relaxations a Debye response is represented by a Lorentzian function as per expression 5.8 and the Bose factor was not applied. For

fitting purposes, the following simplified versions were used:

$$\chi"_i(\omega) = A\omega_i^2 \frac{\omega\Gamma}{(\omega_i^2 - \omega^2)^2 + (\omega\Gamma)^2} \quad \text{DHO Profile} \tag{6.1}$$

$$\chi"(\omega) = \frac{2A}{\pi} \frac{\Gamma}{4\omega^2 + \Gamma^2} \quad \text{Lorentz Profile} \tag{6.2}$$

where A is the integrated intensity, Γ is the damping parameter which is approximately equal to the half width at half max (HWHM) for a DHO and full width at half max (FWHM) for a Lorentzian and ω_i is the normal frequency of the phonon. Due to the overlap of CPs and low frequency modes at temperatures near the 570 K transition, the Raman spectra of NBT were analyzed in the following way while excluding the region from $\pm 5\text{cm}^{-1}$ where Rayleigh scattering occurs: Starting from the 1000K spectral profile of the cooling data, the two CPs were initialized first with Lorentzian functions, then the high frequency peaks associated with hard phonons were initialized with damped harmonic oscillator (DHO) response functions scaled by the Bose factor. The Levenburg-Marquart algorithm was applied in Origin 8.5 to obtain the best fit. The parameters of each successive lower temperature were initialized with the best fit values of the previous higher temperature results. This was continued down to 500K and the goodness of fit χ^2 minima was used to determine the best fit. Fits were attempted with and without the four low frequency peaks from 20 to 75 cm^{-1} at each temperature, but the best fit results had the low frequency peaks with zero amplitude above 650K, thus indicating they could not be resolved from the Lorentzian central peaks. Profiles from 500 to 600 K had significantly smaller χ^2 values when the low frequency peaks were included, thus indicating their presence. At each temperature a fit of the broad CP was attempted with both a variable width and a fixed width set equal to the value found at 1000K. The χ^2 result with variable width fits were consistently smaller and the parameters are shown in figure 6.11(b).

The lower temperature profiles from 80K upwards were similarly analyzed: the narrow CP was initialized first, followed by an arbitrary broad CP that was given a fixed width based on the 1000K spectra and an amplitude that was set as large

as possible, with the remaining DHO peaks initialized including the Bose factor expression. Higher temperatures were fit using the final parameters of the previous lower temperature and care was taken to fix the DHO amplitudes above 100 cm^{-1} whenever possible. This ensured that the fastest changing component of the spectrum would be attributed to the CPs, which is apparent from the temperature evolution of the integrated intensities seen in figure 6.6. Fits with variable broad CP widths were attempted but found not to be successful in that the parameter evolution of the low frequency phonon modes became erratic. The decision to fix the broad CP width was also partly based on the results shown in KH_2PO_4[170] and $Rb_{1-x}K_xCaF_3$[171] where broad CPs are found to be temperature independent within each phase. It is important to note that, when fitting complex spectra such as those of NBT, the quality of the fit is necessary but not sufficient in determining the validity of the underlying model. It is also essential to examine the values obtained for the fitting parameters in the context of the particular physical phenomena studied as shown in a recent study of PZN[172]. It is often possible to obtain good fits with values of the fitting parameters that are not physically meaningful in this context, hence the decision to fit with a fixed broad CP width despite the possibility of higher goodness of fit values compared to a variable width.

The analysis of the low frequency part of the spectrum was more delicate, particularly at intermediate temperatures, where both CPs overlap with the four lowest frequency peaks. A set of models were examined: the four low frequency modes were allowed positions and widths that were either fixed or variable for only the lowest one, two, three or all four at once. Additionally, the model by Axe and Shirane[79] where the CP is coupled to the lowest DHO phonon was considered as it reduces the number of parameters by 1 for each mode coupled. The use of this model did not substantially improve the fits and thus cannot be informative as to the underlying physics in this system, particularly as the four lowest phonon modes overlap so significantly. The uncoupled fit using all four modes with variable widths and positions had the lowest χ^2 value and the results are shown in figure 6.9. The phonon peak at 23 cm^{-1} is seen to change position and width up to 200K, basically becoming Lorentzian in profile and fitting directly underneath the narrow CP. Adjustments

of its parameters above 300K did not result in any changes to the χ^2 value and its presence is assumed only on the basis of its existence at 80-150 K. The other 3 peaks slowly soften and dampen with increasing temperature up to 600K. Fits were not attempted above 600K as the low frequency peaks merge into the CP's and are not resolved from the broad CP as explained above.

Lorentzian fits instead of DHOs were also attempted for the high frequency peaks in the cubic, tetragonal and low temperature phases but were not retained as useful solutions because the χ^2 values were much higher than for DHOs, particularly at the lowest temperatures. The possibility of an anharmonic oscillator model was also not considered as the DHO fits were excellent at all temperatures above 100 K and there is no indication of a Fano-like line shape as reported in $BaTiO_3$[173].

In analyzing the above Raman spectra a distinction was made between the higher frequency peaks, corresponding to the hard modes, and the lower frequency peaks and CPs. Comparing the experimental spectra at different temperatures, it is relatively easy to see that each main phonon peak is composed of two or more component peaks, as should be expected from symmetry considerations. According to the table 5.1, 15 Raman active modes are expected in the tetragonal phase and 13 in the rhombohedral phase. However, to minimize the number of fitting parameters, only two DHOs were used for each high frequency phonon peak in the tetragonal phase and a good fit could still be obtained. The temperature dependent results of the high frequency modes were similar to those reported by Luo et al.[157] and are not reproduced here. The temperature evolution of the parameters of the low frequency composite peak are shown in figure 6.9.

Figure 6.10 shows examples of the fitted spectra at 80K, 400K, 700K and 950K, i.e. below the lower transition, between the two transitions and above the higher transition respectively. The main features that differentiate these results from the previous work by Luo[157], Siny[83] and Kreisel[129] are the inclusion of two CPs and fitting of the low frequency composite peak near 40 cm^{-1} with 4 peaks.

Figures 6.11(a) and 6.11(b) show the results of the CP parameters. The amplitudes of the two Lorentzian CPs exhibit different temperature dependencies. The

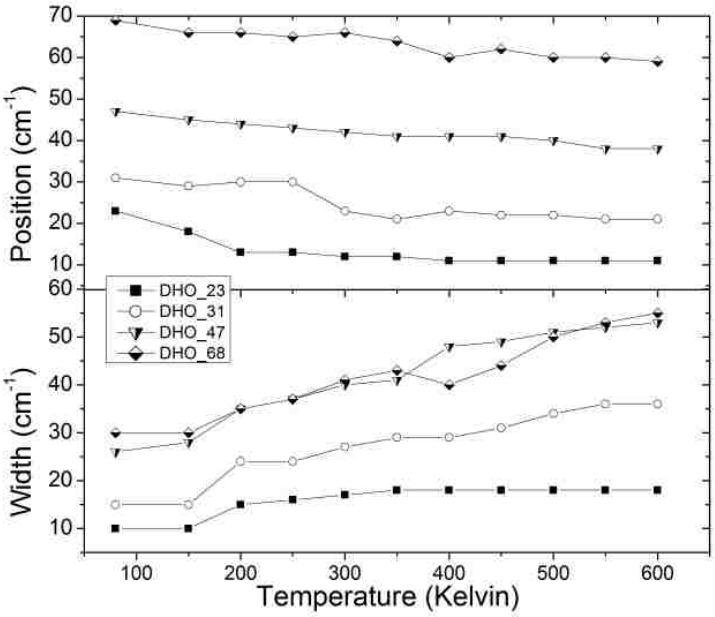

Figure 6.9: Comparison of position and width of the 4 lowest frequency phonon modes upon cooling. All peaks exhibit softening and damping near the 570 K transition.

narrow CP amplitude has a cusp-like maximum at 600K, near the lower phase transition, and steadily decreases on either side to a minimum at the highest and lowest temperatures similar to the dielectric constant[141]. The narrow CP amplitude also has notably similar values when comparing the two fitting models used in the region of 450-600 despite the fact of having arrived to these values from two very different initial spectra. The broad CP amplitude profile is qualitatively similar to the total integrated intensity seen in figure 6.6, flat between 900 and 600 K with a steadily decrease in the low temperature range similar to the narrow CP amplitude. The width of the narrow CP decreases continuously with temperature and shows a faint width anomaly at the lower of the phase transitions. The corresponding relaxation time for the high temperature region is shown in the inset to follow a Vogel-Fulcher

pattern. In contrast, the broad CP width decreases throughout the cubic phase and becomes flat in the tetragonal phase with a small increase at 600 K. The curves for the broad CP amplitude do not meet near 550 K due to the presence of the low frequency peaks in the low temperature fits.

6.7 Central peaks

The present results on the CPs and low frequency peaks represent the most original part of the present study. Previous reports[82] indicated that there was only one low frequency peak and one CP. Only a qualitative estimate of the relaxation time from the width of the broad CP was given without deconvolution into two separate peaks although the possibility for two peaks was suggested. Consequently, the present study with a full deconvolution provides further and finer details on the transition dynamics of NBT. The Raman results for the CPs are shown qualitatively in figures 6.5(a) and 6.10 and quantitatively in figures 6.11(a) and 6.11(b). In the high temperature range, 650 to 1000 K, the low frequency region of the spectrum, 5-100 cm^{-1}, is fitted with 2 Lorentzian's as it is impossible to resolve any low frequency peaks. At the highest temperature, T=1000 K, the central part of the spectrum seen in figure 6.5(a) has a different overall shape from those at lower temperatures and it is primarily composed of a broad CP. Below the first transition at ≈820K, two CPs can be distinguished, a narrow one and a broad one. Below the second transition at ≈ 570K, three low frequency phonon peaks emerge from the broad CP becoming four below 200 K. The analysis reveals that the CP spectrum cannot be fitted with a single Lorentzian profile at any temperature. It is also possible to speculate that the profile might be understood as one continuous distribution of relaxations potentially fitted with a single functional shape, but the 2 Lorentzian approach shown below makes physical sense, allowing for separation of the central intensity into differing relaxation regions originating or related to two different physical mechanisms.

6.7.1 Broad central peak

Precursor ordering, common to order-disorder phase transitions[75] and relaxor FE's[27] well above the phase transition temperature as mentioned in section 1.3, occurs in NBT as rotation of the anion octahedron which diffuses to surrounding octahedra and lowers the space group symmetry. The CP widths associated with precursor ordering correspond to fluctuation lifetimes while their amplitudes are related to the size or number of regions. In NBT these precursor regions can be modeled as asymmetric double well potentials involving the rotation of the relatively rigid[8] TiO_6 anion octahedra[75, 174], which is the accepted order parameter in NBT[19]. The double well potential for the anion octahedra in NBT can be understood qualitatively by considering the greater attraction of an oxygen atom to either of the two neighboring Bi^{3+} atoms rather than the Na^{1+} atoms, with Bi^{3+} therefore acting as a driver of the TiO_6 rotation. Given sufficient thermal energy, the octahedron anions can "hop" or equivalently "twist" over to an alternate configuration and thus re-orient either a single octahedron or a local elastic region. Thermal fluctuations must therefore involve variations in the rotational angle and propagate in a diffusive manner as the octahedra are corner sharing. These diffusive fluctuations are expected to increase in size and lifetime as the phase transition is approached as a result of the growth of the precursor regions. TiO_6 rotation also causes a change in the unit cell lattice parameters[47] resulting in localized strain. Adjacent or nearby regions will interact via these local strain fields, resulting in rotational diffusion through rotational-translational coupling. This coupling has been described with a microscopic model in molecular crystals such as CH_4 and KCN[175], but to the author's knowledge has not been applied to perovskites. We speculate that the relatively larger CP widths in NBT correspond not to a single time scale but to a distribution of relaxation times that include fast rotations of single octahedra, and slower rotations of both correlated chains (M-point rotation) and regions (R-point rotations) which have differing sizes and interact via strain. This suggestion may help resolve the current questions about the origin and mechanism of strain dynamics in NBT[176, 177].

The amplitude and width of the broad CP are shown in figure 6.11(a) and follow the expected temperature evolution for dynamics of precursor regions near first order phase transitions. The presence of cubic phase precursor regions in NBT are observed as faint neutron superlattice reflections at the M-point of the Brillouin zone which correspond to rotations of the anion octahedron[48] and from second harmonic generated light which indicates a lower symmetry up to 900 K[19]. The neutron superlattice reflections are present at 1000 K and increase steadily in magnitude upon cooling to the 820 K phase transition[48] where there is an abrupt large increase to a stable value that is nearly constant through the tetragonal phase. This is consistent with the characteristics of first order phase transitions discussed in section 1.3. Therefore the large broad CP width at 1000 K can be attributed to fast lifetime fluctuations of the anion octahedra, and the decrease through the cubic phase towards the 820 K transition therefore indicates a slowing down of these fluctuations to the phase transition, where they become constant with temperature. The corresponding amplitude increase will therefore denote an increase in the size or amplitude of the fluctuations. The presence of precursor regions is also observed in figure 6.10 where the high frequency fits in the cubic phase at 950 K and the tetragonal phase at 700 K are notably similar, thus confirming that the Raman inactive F_{1u} phonons[130] become Raman active due to the local asymmetry of the precursor regions. This similarity also suggests that NBT exhibits no significant second order scattering, unlike $SrTiO_3$[174].

In the tetragonal phase, from 650 K to 800 K in figure 6.11(a), the amplitude and width of the broad CP remain relatively constant, consistent with the M point Bragg peak amplitude[48]. This indicates that the precursor regions have grown in size and number so that they are in contact with each other and represent the dominant structural phase. The strain due to the octahedron rotations, observed with X-rays to have a maximum axis ratio[136] of $\frac{c}{a} - 1 = 0.002$, are not large enough to suppress the local fluctuations[75]. The polydomain nature of this phase suggests that the diffusive fluctuations will involve strain mediated rotational diffusion between adjacent nanoscale domains.

In the low temperature phase, there is a five fold decrease in amplitude from

600 to 80 K, seen in figure 6.11(a), which is consistent with freezing of the dynamic fluctuations[75] and correlated with the appearance of the low symmetry, polar phase[131]. As mentioned in section 6.5, the increase in the ratio of the 295/35 peak intensities seen in figure 6.7 through the low temperature phase suggests a change in the broad CP background. This intensity ratio is temperature independent above 600 K and shows a steady increase upon cooling to 80 K due to the broad CP amplitude decrease, therefore affecting the 35 cm^{-1} peak more strongly than the 295 cm^{-1} peak. The mechanism of the diffusive fluctuations from 600 to 400 K are now related to hetero-phase rotational diffusion between the coexisting R-point and M-point anion octahedral rotations observed in neutron[48] and X-ray results[61]. Below 400 K, the observation of nanometer scale tetragonal platelets and twinning[132] suggests that these strain related rotational fluctuations can persist down to lower temperatures.

To confirm this hypothesis, a comparison to other similar perovskite materials is considered. The width of the broad CP in NBT is comparable only to materials that exhibit rotational reorientation of molecular constituents with precursor ordering near the structural phase transitions. The previously mentioned fluoro-perovskites, $KMnF_3$[178]($\Gamma_1 \approx$ 10-30cm^{-1} and $\Gamma_2 \approx$ 120-170cm^{-1} between T_{c1}=186K and T_{c2}=91.5K), $RbCaF_3$ ($\Gamma \approx$ 80 cm^{-1} above T_{c1}=186)[138] and its potassium doped solid solutions[171], all have comparable CP widths that are present far above the transition temperature and are constant within the non-cubic structural phases. The precursor ordering above the phase transition also results in first order Raman peaks, and octahedral rotation is the primary order parameter of their respective phase transitions. By contrast, none of the titanate perovskites have similar widths, nor do any of their A-site mixed derivatives such as $Pb_{0.6}Sr_{0.4}TiO_3$[179], $Ba_xSr_{1-x}TiO_3$[180], $Ba_xCa_{1-x}TiO_3$[181],or $Pb_{1-x}Ba_xTiO_3$[182]. There are few A-site disordered perovskites with well studied CPs available for comparison. Lead based relaxors were also considered because of their disorder based characteristics and the lone pair of electrons in the outer shell is similar to the configuration of the Bi^{3+} ion in NBT. However, the CPs in Pb relaxors were generally found to derive from different physical phenomena, namely an overdamped soft mode in PMN[183],

TA-TO coupling in PZN[172] and slow relaxations of polar regions in PST[184]. Based on these comparisons to other similar materials, we conclude that the physical origin of the broad CP in NBT is due to the diffusion of the anion octahedra rotations.

6.7.2 Narrow central peak

The temperature evolution of the narrow CP amplitude can be explained by PND dynamics and, near the lower temperature phase transition, overlap of the low frequency phonon modes. Dynamical polar behavior has been observed in the dielectric relaxation spectrum[61, 141] to increase with decreasing temperature smoothly through the 820 K phase transition to a maximum near the 570 K phase transition and then decrease in a monotonic fashion through the lower temperature phase[141]. The narrow CP amplitude seen in figure 6.11(b) qualitatively follows this temperature progression in that it also increases without obvious changes through the 820 K phase transition to a single cusp at 600 K and decreases steadily thereafter down to 80 K. In the cubic to tetragonal phases the amplitude increase can therefore be attributed to the increasing size and number of PND's until 570 K, where the subsequent decrease is then due to freezing of the domains which become static and macroscopically large in the ferroelectric phase[81, 131]. The presence of cation relaxation at all temperatures, far from the phase transitions and at low temperatures, is unusual and due to the small cation size on the A-site relative to the available space. The ^{23}Na re-orientation observed in NMR[28] suggests that dynamical variations in dipole strength and direction are possible without complete polarization reversal. Although the 8-site potential model is well accepted for B-site cations such as Ti[8], there is no theoretical model to this author's knowledge about the local potential restrictions for the A-site cations, but they are observed to have average positions aligned with the B-site ion[19].

The cusp in the amplitude near 570 K is sharper than expected for the known dielectric response. Comparison of the dielectric relaxation peaks seen in NBT[141]

to other typical relaxors such as KLT and PST[185] provides information on the nature of the local ordering of the PNDs. KLT and PST data indicate that strongly disordered systems exhibit broad dielectric peaks, while more ordered systems have a sharp drop at the transition temperature. There is more evidence of NBT being a disordered system with the lower phase transition spread over at least 100 degrees[48], so the relatively sharp CP amplitude peak at 600 K, which does not follow the broad character of the dielectric relaxation profile, may be due to an additional component besides the abrupt freezing of the high frequency fluctuations that contribute to the narrow CP amplitude. A possible alternate explanation is that the low frequency phonons, which exhibit increased damping near the transition and soften so that they overlap the CP near 600 K, couple to the relaxations as symmetry considerations do not exclude this interaction. Similar low frequency phonons are assigned as R-point phonons in both $KMnF_3$ and $RbCaF_3$ systems and are therefore expected to become Raman inactive above the transition. The presence of faint R-point neutron Bragg peaks[48] in the tetragonal phase suggest remnants of these phonons may continue to contribute to the narrow CP above 600 K, exhibiting increased damping that is associated with shorter phonon lifetimes[127], but are not resolvable in these measurements. The steady decrease in the amplitude below 600 K to 80 K is remarkably similar to the temperature evolution of the amplitude of the broad CP below 600K, indicating that they are affected by the same freezing related changes. It should also be noted that the temperature dependence of the narrow CP amplitude seen in figure 6.11(b) is nearly identical to that of the Brillouin CP integrated intensity[161] taken upon cooling, which would be expected as the total Brillouin spectra corresponds to ± 3 cm^{-1}, i.e. within the narrow CP.

The width of the narrow CP also follows the expected behavior for order-disorder phase transitions and relaxor ferroelectrics[27]. As mentioned in section 1.7, dielectric relaxations originating from PND fluctuations are generally recognized to follow the Vogel-Fulcher (VF) model for order-disorder transitions[81] and have been observed in NBT doped with Ba[154]. This model has not been invoked in any of the dielectric work to date for pure NBT[141, 152, 153]. The VF model, $\tau = \tau_0 exp^{(U/(k(T-T_m)))}$, is used to describe freezing related to the growth of clusters

of electric dipoles above a freezing temperature, T_m, that can be independent of the phase transition temperature, T_c. The narrow CP width in NBT appears linear in figure 6.11(b), but the inset shows the relaxation time from 1000 K to 600 K following a VF model with an activation energy $\frac{U}{k} = 24$ K, a freezing temperature T_m of 554 K and a relaxation time τ_0 of 2.09 x10^{-12} s. This value for T_m is close to the known onset temperature of spontaneous remnant polarization[141]. Below T_m, the relaxation time from 600 K to 150 K changes linearly with temperature with a slope of 7.45 x10^{-9} $\frac{s}{K}$, which is also consistent with the monotonic evolution of the dielectric constant below 570 K[141] and the expected change in dynamics due to the onset of microscopic polar regions[131].

An alternate hypothesis that must be considered is a CP due to fluctuations resulting from defect mobility[186] as these are also known to be 3-15 cm^{-1} in width. Oxygen vacancy defects in NBT have been reported in conductivity measurements[187], crystal growth[188, 189] and may be deduced in our sample from both the absorption spectrum and laser heating as shown in figures 6.3 and 6.4 respectively as well as the presence of the faint Ti-O terminating mode at 1060 cm^{-1} attributed to vacancies[190] (data not shown). However, the defect concentration is expected to be less than one part per billion based on similar vacancy concentrations observed after vacuum annealing in other titanates[49]. Therefore the physical origin of the narrow CP is more likely to be the PND dynamics rather than defects based on the simple argument of the relative density of the two components. Also, defect mobility is not expected to have a peak at 600 K as mobility would increase with increasing temperature, thus affirming the correlation between the narrow CP amplitude peak at 600K and the temperature evolution of the dielectric constant.

One can thus propose the following description of the transition dynamics in NBT. Above Tc_1 at 820 K, NBT is on average cubic, although the high frequency phonon peaks and the broad CP both reveal the onset of precursor regions of tetragonal symmetry observed as the planar M-point rotations of the O_6 octahedra. The associated relaxations are related to thermally activated rotational diffusion and translational-rotational coupling. The relaxation time of these fluctuations decrease with decreasing temperature in the cubic phase, with the broad CP becoming stable

in the tetragonal phase while the narrow CP continues to decrease with a VF character to $\sim$ 554 K. These relaxations in the tetragonal phase are also accompanied by low symmetry precursor phase formations as evidenced by R-point Bragg peaks as well as correlated fluctuations of the cation displacements which are responsible for the growth of the narrow CP and are confirmed by the characteristic relaxor behavior of the dielectric constant due to the formation of polar nanodomains in the same temperature range[141]. Finally, the low temperature phase exhibits a decrease in the amplitudes of both CP's and a linear decrease in the narrow CP width due to motional freezing of the cations, TiO_6 octahedrons and the hardening of the low frequency phonon modes.

6.8 Assignment and temperature evolution of the phonon peaks

The NBT Raman results are shown in figure 6.10, and as the high frequency regions above 100 cm^{-1} have already been well described[83, 129, 157], the focus here is on the new low frequency results. The fits reveal the presence of four peaks in the 5-100 cm^{-1} region below 150 K, which can be reduced to three above 200 K as the lowest frequency peak becomes eclipsed by the narrow CP. As can be seen in figure 6.9, the evolution of the four low frequency phonon peaks show definite softening behavior that is linear in ω vs. T, as well as increased damping. None of the attempted fits showed the linear ω^2 vs. T character reported previously for the composite peak[82]. This observed temperature dependence is more characteristic of an order-disorder transition as per the Lyddane-Sachs Teller relation[56] shown in equation 1.7, and is consistent with the known characteristics of the lower temperature phase transition and the monotonic evolution of the dielectric constant below 570 K[141]. The temperature dependence of the low frequency modes seen in figure 6.9 is notably similar to the monotonic temperature evolution of the width and position of the low frequency modes at 28,37,49 and 62 cm^{-1} in monoclinic $KMnF_3$

and 31,36,44,75.6 and 84 cm^{-1} in orthorhombic $RbCaF_3$. By comparison, the previously mentioned oxide perovskites all have either 1 or 2 low frequency modes which exhibit softening with a linear ω^2 vs temperature dependence upon approach to the cubic to tetragonal transition, and no significant change near the lower temperature R3c symmetry phases. In general, R3c symmetry perovskite ferroelectrics such as $BiFeO_3$[135] and $NaNbO_3$[191], $R\bar{3}c$ symmetry perovskites such as LaAlO3[192] and $LaCoO_3$[193] all have either 1 or 2 modes in the low temperature phase. The lack of correspondence between the low frequency modes of NBT and any of either the oxide titanate perovskites or perovskites of R3c and $R\bar{3}c$ symmetry suggests that the R3c symmetry assignment may not be correct. The recent suggestion of Cc monoclinic symmetry[145] was made despite the admitted absence of a confirming peak at the [0.5,0.5,0.5] point of the Brillouin zone. This inconsistency, in conjunction with the low frequency results shown here, suggests that additional work is required to determine the correct low temperature symmetry. We also note that the lattice parameters determined from X-ray analysis are strikingly similar between NBT[136] and $KMnF_3$[139], particularly in the low temperature phases where the lattice parameters in $KMnF_3$ are too similar to be resolved. Direct comparison to other perovskite materials of Cc symmetry is not possible at this time as we are unaware of any other perovskite materials with fitted low frequency modes. PZT-PT[194–196] and thin films of $BiFeO_3$[197] on $SrTiO_3$ substrates have been assigned Cc symmetry, but no deconvolution of low frequency modes was attempted despite evidence of multiple peaks in the low frequency region. These results in NBT appear to confirm the recent suggestions of a different low temperature symmetry in NBT as there are more low frequency modes than R3c materials and these modes disappear concurrently with the R-point Bragg peak in neutron scattering[48]. However, the assignment of Cc cannot be confirmed due to the lack of polarization information for each peak.

6.9 Conclusion

The Raman results of NBT presented in this thesis have revealed the existence of two CPs, a narrow one and a broad one. Both peaks appear well above the high temperature cubic-tetragonal transition but display very different temperature behavior. The broad CP clearly grows upon approach of the high temperature transition (≈820K), which is related to the cooperative rotations of oxygen octahedra (M-point of the reciprocal lattice). Its origin is therefore attributed to the rotational fluctuations and their diffusion, which are associated with the presence of precursor clusters of the tetragonal phase. By contrast, the narrow CP grows continuously through that transition and is unaffected by it, as does the dielectric peak which corresponds to the relaxor behavior. The narrow CP is therefore associated with the same relaxational dynamics that give rise to the relaxor behavior of the dielectric constant. Upon crossing the low temperature phase transition (≈580K), both CPs progressively loose amplitude, indicative of a slowing down of their relaxational dynamics and the progressive establishment of a static long range order, independently confirmed by x-ray measurements. Concurrently, four low frequency phonons appear in the spectrum. Their number suggests a low temperature ferroelectric phase different than the R3c symmetry previously reported.

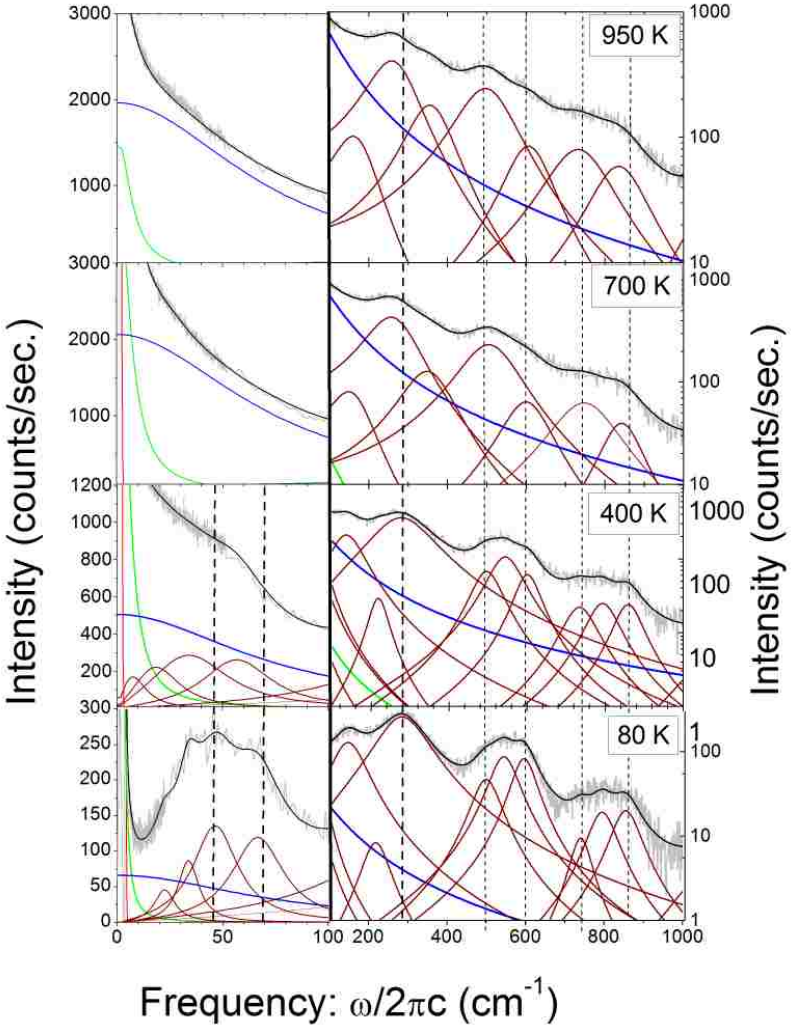

Figure 6.10: Fitted spectra at 950K, 700K, 400and 78K from the cooling data starting from 1000 K. At all temperatures, the CPs are fitted with two Lorentzian functions (blue for the broad CP and green lines for the narrow CP). High frequency peaks are fitted with DHOs. For graphical purposes, the spectra are shown in two frequency panels, the left side has the lower frequency with linear vertical scale and the right hand side has the higher frequencies with the log 10 vertical scale. The vertical dashed lines are visual guides to highlight the apparent shift in frequency of the peaks with temperature.

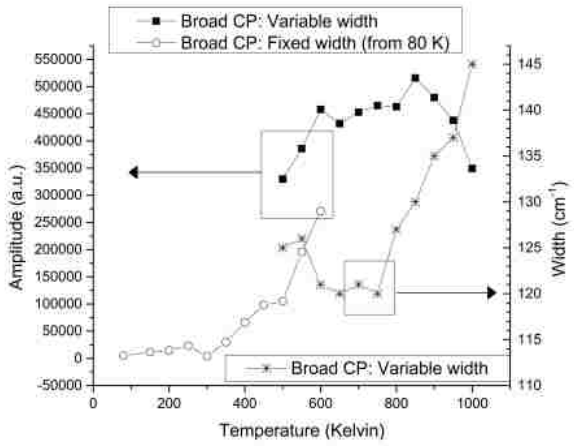

(a) Broad central peak

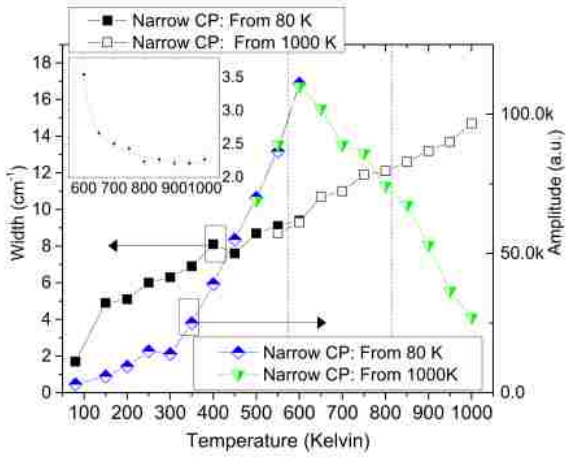

(b) Narrow central peak

Figure 6.11: Temperature dependence of the two CP parameters of width and amplitude, showing the fits started from 80K and 1000K. The broad CP was fixed at 145 cm^{-1} for all low temperature fits shown as explained in the text. Although there appears to be a discontinuity in amplitude of the broad CP, the reader should refer to figure 6.6(b) where the addition of the amplitudes of the low frequency peaks makes up for the change in total amplitude. The inset in figure 6.11(a) is the relaxation time, $\tau = 1/c\Gamma$ (x10^{-12} s^{-1}), vs. temperature in Kelvin with a Vogel-Fulcher fit to the data.

Bibliography

[1] Bass, M. (ed.) *Handbook of Optics:Devices, Measurements, and Properties*, vol. 2 (McGraw-Hill, 1994), second edn.

[2] Zysset, B., Biaggio, I. & Günter, P. Refractive indices of orthorhombic $KNbO_3$. I. Dispersion and temperature dependence. *J. Opt. Soc. Am. B* **9**, 380–386 (1992).

[3] Chen, F. S., Guesic, J. E., Kurtz, S. K., Skinner, J. G. & Wemple, S. H. Light modulation and beam deflection with potassium tantalate-niobate crystals. *Journal of Applied Physics* **40**, 3389–3394 (1966).

[4] Tian, H., Zhou, Z., Wang, H. & Liu, D. Optical properties of cubic $K_{0.95}Li_{0.05}Ta_{0.61}Nb_{0.39}O_3$ single crystal. *Optical Materials* **31**, 106 – 109 (2008).

[5] Yang, W. *et al.* Structure and refractive index dispersive behavior of potassium niobate tantalate films prepared by pulsed laser deposition. *Applied Surface Science* **257**, 7221 – 7225 (2011).

[6] Loheide, S., Riehemann, S., Mersch, F., Pankrath, R. & Krätzig, E. Refractive indices, permittivities, and linear electrooptic coefficients of tetragonal potassium tantalate-niobate crystals. *Physica Status Solidi (a)* **137**, 257–265 (1993).

[7] De Graef, M. & McHenry, M. E. *Structure of Materials:An Introduction to Crystallography, Diffraction and Symmetry* (Cambridge University Press, 2012), second edn.

[8] Lines, M. & Glass, A. *Principals and Applications of Ferroelectrics and Related Materials* (Oxford University Press, 2004).

[9] Zaccai, G. & Hewat, A. W. Soft modes and the structure of ferroelectric tetragonal KTN. II. The lattice dynamics of the cubic phase. *Journal of Physics C: Solid State Physics* **7**, 15 (1974).

[10] Girshberg, Y. & Yacoby, Y. Off-centre displacements and ferroelectric phase transition in dilute $KTa_{1-x}Nb_xO_3$. *Journal of Physics: Condensed Matter* **13**, 8817–8830 (2001).

[11] Prater, R. L., Chase, L. L. & Boatner, L. A. Raman scattering studies of the impurity-induced ferroelectric phase transition in $KTaO_3$:Nb. *Phys. Rev. B* **23**, 221–231 (1981).

[12] Samara, G. A. & Morosin, B. Anharmonic effects in $KTaO_3$: Ferroelectric mode, thermal expansion,and compressibility. *Phys. Rev. B* **8**, 1256–1264 (1973).

[13] Shirane, G., Newnham, R. & Pepinsky, R. Dielectric properties and phase transitions of $NaNbO_3$ and (Na,K)NbO_3. *Phys. Rev.* **96**, 581–588 (1954).

[14] Triebwasser, S. Study of ferroelectric transitions of solid-solution single crystals of $KNbO_3$-$KTaO_3$. *Phys. Rev.* **114**, 63–70 (1959).

[15] Goeking, K. W., Pandey, R. K., Squattrito, P. J., Clearfield, A. & Beratan, H. R. Temperature gradient transport growth of potassium tantalate niobate, $KTa_{1-x}Nb_xO_3$, single crystals. *Ferroelectrics* **92**, 89–97 (1989).

[16] Jellison, G. E., Paulauskas, I., Boatner, L. A. & Singh, D. J. Optical functions of $ktao_3$ as determined by spectroscopic ellipsometry and comparison with band structure calculations. *Phys. Rev. B* **74**, 155130 (2006).

[17] Hewat, A. W. Cubic-tetragonal-orthorhombic-rhombohedral ferroelectric

transitions in perovskite potassium niobate: neutron powder profile refinement of the structures. *Journal of Physics C: Solid State Physics* **6**, 2559 (1973).

[18] Rytz, D. & Scheel, H. Crystal growth of $KTa_{1-x}Nb_xO_3$ ($0 \leq x \leq 0.04$) solid solutions by a slow-cooling method. *Journal of Crystal Growth* **69**, 468–484 (1982).

[19] Jones, G. & Thomas, P. Investigation of the structure and phase transitions in the novel A-site substituted distorted perovskite compound $Na_{0.5}Bi_{0.5}TiO_3$. *Acta Crystallographica* **B58**, 168 (2002).

[20] Thomas, P., Trujillo, S., Boudard, M., Gorfman, S. & Kreisel, J. Diffuse X-ray scattering in the lead-free piezoelectric crystals $Na_{\frac{1}{2}}Bi_{\frac{1}{2}}TiO_3$ and Ba-doped $Na_{\frac{1}{2}}Bi_{\frac{1}{2}}TiO_3$. *Solid State Sciences* **12**, 311 – 317 (2010).

[21] Seung-Eek Park, I.-T. K., Su-Jin Chung & Hong, K. S. Nonstoichiometry and the long range cation ordering in crystals of $(Na_{\frac{1}{2}}Bi_{\frac{1}{2}})TiO_3$. *J. Amer. Ceram. Soc.* **77**, 2641–7 (1994).

[22] Spreitzer, M., Valant, M. & Suvorov, D. Sodium deficiency in $Na_{0.5}Bi_{0.5}TiO_3$. *J. Mater. Chem.* **17**, 185–192 (2007).

[23] Sung, Y. S. *et al.* Effects of Bi nonstoichiometry in $(Bi_{0.5+x}Na)TiO_3$ ceramics. *Applied Physics Letters* **98**, 012902 (2011).

[24] Gröting, M., Kornev, I., Dkhil, B. & Albe, K. Pressure-induced phase transitions and structure of chemically ordered nanoregions in the lead-free relaxor ferroelectric $Na_{1/2}Bi_{1/2}TiO_3$. *Phys. Rev. B* **86**, 134118 (2012).

[25] Stern, E. A. Character of order-disorder and displacive components in barium titanate. *Phys. Rev. Lett.* **93**, 037601 (2004).

[26] Shannon, R. Revised effective ionic radii and systematic studies of interatomic distances in halides and chalcogenides. *Acta Crystallographica* **B32**, 751 (1976).

[27] Bokov, A. & Ye, Z.-G. Recent progress in relaxor ferroelectrics with perovskite structure. *Journal of Materials Science* **41**, 31–52 (2006).

[28] Aleksandrova, I. P., Sukhovsky, A. A., Ivanov, Y. N., Yablonskaya, Y. E. & Vakhrushev, S. B. Local and average structure of relaxor $Na_{\frac{1}{2}}Bi_{\frac{1}{2}}TiO_3$ from the point of view of NMR. *Ferroelectrics* **378**, 16–22 (2009).

[29] Takagi, S., Subedi, A., Cooper, V. R. & Singh, D. J. Effect of A-site size difference on polar behavior in $MBiScNbO_6$ (M=Na, K, and Rb): Density functional calculations. *Phys. Rev. B* **82**, 134108 (2010).

[30] Wang, K., Liu, J.-M. & Ren, Z. Multiferroicity: the coupling between magnetic and polarization orders. *Advances in Physics* **58**, 321448 (2009).

[31] Tejuca, L. & Fierro, J. (eds.) *Properties and Applications of Perovskite-Type Oxides* (CRC Press, 1992), first edn.

[32] Fay, H. Characterization of potassium tantalate-niobate crystals by electro-optic measurements. *Materials Research Bulletin* **2**, 679–688 (1967).

[33] Kurtz, S. Design of an electro-optic switch for high capacity high speed digital light deflection system. *Bell System technical Journal* 1209–1246 (1966).

[34] Scheel, H. Theoretical and technological solutions of the striation problem. *Journal of Crystal Growth* **287**, 214–223 (2006).

[35] Hofmeister, R., Yariv, A., Yagi, S. & Agranat, A. New Photorefractive Mechanism in Centrosymmetric Crystals: A Strain-Coordinated Jahn-Teller Relaxation. *Physical Review Letters* **69**, 1459–1462 (1992).

[36] Agranat, A. J., Kaner, R., Perpelitsa, G. & Garcia, Y. Stable electro-optic striation grating produced by programed periodic modulation of the growth temperature. *Applied Physics Letters* **90**, 192902 (2007).

[37] Nakamura, K. *et al.* Space-charge-controlled electro-optic effect: Optical beam deflection by electro-optic effect and space-charge-controlled electrical conduction. *Journal of Applied Physics* **104**, 013105–1 (2008).

[38] Toyoda, S. *et al.* Low-driving-voltage electro-optic modulator with novel $KTa_{1-x}Nb_xO_3$ crystal waveguides. *Japanese Journal of Applied Physics, Part 1: Regular Papers and Short Notes and Review Papers* **43**, 5862–5866 (2004).

[39] Imai, T. *et al.* Fast response varifocal lenses using $KTa_{1-x}Nb_xO_3$ crystals and a simulation method with electrostrictive calculations. *Appl. Opt.* **51**, 1532–1539 (2012).

[40] Takenaka, T., Nagata, H. & Hiruma, Y. Phase transition temperatures and piezoelectric properties of $(Bi_{\frac{1}{2}}Na_{\frac{1}{2}})TiO_3$-and $(Bi_{\frac{1}{2}}K_{\frac{1}{2}})TiO_3$-based bismuth perovskite lead-free ferroelectric ceramics. *Ultrasonics, Ferroelectrics and Frequency Control, IEEE Transactions on* **56**, 1595 –1612 (2009).

[41] Sheets, S. A., Soukhojak, A. N., Ohashi, N. & Chiang, Y.-M. Relaxor single crystals in the $(Bi_{\frac{1}{2}}Na_{\frac{1}{2}})_{1-x}Ba_xZr_yTi_{1-y}O_3$ system exhibiting high electrostrictive strain. *Journal of Applied Physics* **90**, 5287 (2001).

[42] Ge, W. *et al.* Growth, optical and electrical properties of pure and Mn-doped $Na_{0.5}Bi_{0.5}TiO_3$ lead-free piezoelectric crystals. *Journal of Alloys and Compounds* **462**, 256 – 261 (2008).

[43] Zhang, R., Jiang, B., Jiang, W. & Cao, W. Complete set of properties of 0.92pb(zn1/3nb2/3)o30.08pbtio3 single crystal with engineered domains. *Materials Letters* **57**, 1305 – 1308 (2003).

[44] Bradley, C. & Cracknell, A. *The Mathematical Theory of Symmetry in Solids* (Claredon Press, 2010).

[45] Ashcroft, N. W. & Mermin, N. D. *Solid State Physics* (Thompson Learning, Inc., 1976), first edn.

[46] Salje, E. K. *Phase transitions in Ferroelastic and Co-Elastic Crystals* (Cambridge University Press, 1990), first edn.

[47] Glazer, A. M. Simple ways of determining perovskite structures. *Acta Crystallographica Section A* **31**, 756–762 (1975).

[48] Vakhrushev, S. *et al.* Phase transition study on the ferroelectric crystal $Na_{0.5}Bi_{0.5}TiO_3$ by the neutron scattering method. *Kristallografiya* **34**, 154–158 (1989).

[49] Smyth, D. *The defect chemistry of metal oxides* (Oxford University Press, 2000).

[50] Nowick, A. & Berry, B. *Anelastic Relaxation in Crystalline Solids* (Academic Press, 1972), first edn.

[51] Fowler, W. B. (ed.) *Physics of Color Centers* (Academic Press Inc., 1968), first edn.

[52] Dvoř*á*k, V. Color centre in $BaTiO_3$ single crystals. *Czech J. Phys.* **11** (1961).

[53] Glinchuk, M., Jastrabik, L. & Stephanovich, V. The sequence of structural phase transitions in $KTa_{l-x}Nb_xO_3$. *Physica B* **222**, 182–190 (1996).

[54] Toulouse, J., Wang, X., Knauss, L. & Boatner, L. Dielectric nonlinearity and spontaneous polarization of $KTa_{1-x}Nb_xO_3$ in the diffuse transition range. *Phys. Rev. B* **43**, 8297–8302 (1991).

[55] Taylor, J. R. *Classical Mechanics* (University Science Books, 2005).

[56] Blinc, R. & Žekš, B. *Soft modes in ferroelectrics and antiferroelectrics* (North Holland Publishing Company, 1974).

[57] Narasimhamurty, T. *Photoelastic and Electro-Optic Properties of Crystals* (Plenum Press, 1981), first edn.

[58] Aizu, K. Possible species of ferromagnetic, ferroelectric, and ferroelastic crystals. *Phys. Rev. B* **2**, 754–772 (1970).

[59] Chelkowski, A. *Dielectric physics* (Elsevier Scientific Publishing Company, 1980), first edn.

[60] Roleder, K., Suchanicz, J. & Kania, A. Time dependence of electric permittivity in $Na_{0.5}Bi_{0.5}TiO_3$ single crystals. *Ferroelectrics* **89**, 1–5 (1989).

[61] Suchanicz, J. Time evolution of the phase transformation in $Na0.5Bi_{0.5}TiO_3$. *Ferroelectrics* **200**, 319–325 (1997).

[62] Samara, G. A. *Solid State Physics: Advances in research and applications*, vol. 56, chap. Ferroelectricity revisited-Advances in materials and physics, 240–457 (Academic Press, 2001).

[63] Cross, L. E. & Newham, R. E. History of ferroelectrics. *Ceramics and Civilization vol. III: High Technology Ceramics Past, Present, and Future* **III**, 289–305 (1987).

[64] Haertling, G. H. Ferroelectric ceramics: History and technology. *Journal of the American Ceramic Society* **82**, 797–818 (1999).

[65] Burns, G. & Dacol, F. The index of refraction of $BaTiO_3$ above T_c. *Ferroelectrics* **37**, 661–664 (1981).

[66] Kleemann, W. Random fields in relaxor ferroelectrics: A jubilee review. *Journal of Advanced Dielectrics* **02**, 1241001 (2012).

[67] Scott, J. F. Soft-mode spectroscopy: Experimental studies of structural phase transitions. *Rev. Mod. Phys.* **46**, 83–128 (1974).

[68] Cochran, W. Crystal stability and the theory of ferroelectricity. *Phys. Rev. Lett.* **3**, 412–414 (1959).

[69] Kugel, G., Vogt, H., Kress, W. & Rytz, D. Study of the ferroelectric soft mode in solid solutions of $KTa_{1-x}Nb_xO_3$ by hyper-Raman scattering. *Phys. Rev. B* **30**, 985–991 (1984).

[70] Sievers, A. J. & Page, J. B. Generalized Lyddane-Sachs-Teller relation and disordered solids. *Phys. Rev. B* **41**, 3455–3459 (1990).

[71] Wesselinowa, J. M. & Apostolov, A. T. A microscopic theory for the central peak in hydrogen-bonded ferroelectrics. *physica status solidi (b)* **201**, 529–550 (1997).

[72] Vakhrushev, S., Kvyatkovskii, B., Okuneva, N., Plachenova, E. & Syrnikov, P. The soft mode and the central peak in $Na_{0.5}Bi_{0.5}TiO_3$. *Fiz. Teverd. Tela.* **25**, 2529–2531 (1983).

[73] Matsuura, M. *et al.* Damped soft phonons and diffuse scattering in $(Bi_{1/2}Na_{1/2})TiO_3$. *Phys. Rev. B* **87**, 064109 (2013).

[74] Fleury, P. & Lyons, K. *Light scattering near phase transitions*, 449–502. No. v. 5 in Modern problems in condensed matter sciences (North-Holland Pub. Co., 1983).

[75] Bruce, A. D. & Cowley, R. Structural phase transitions III. Critical dynamics and quasi-elastic scattering. *Advances in Physics* **29**, 219–321 (1980).

[76] Collins, M. A., Blumen, A., Currie, J. F. & Ross, J. Dynamics of domain walls in ferrodistortive materials. I. Theory. *Phys. Rev. B* **19**, 3630–3644 (1979).

[77] Halperin, B. I. & Varma, C. M. Defects and the central peak near structural phase transitions. *Phys. Rev. B* **14**, 4030–4044 (1976).

[78] Schneider, T. & Stoll, E. Molecular-dynamics study of structural-phase transitions. I. One-component displacement models. *Phys. Rev. B* **13**, 1216–1237 (1976).

[79] Shirane, G. & Axe, J. D. Acoustic-phonon instability and critical scattering in Nb_3Sb. *Phys. Rev. Lett.* **27**, 1803–1806 (1971).

[80] Sokoloff, J. P., Chase, L. L. & Boatner, L. A. Low-frequency relaxation modes and structural disorder in $KTa_{1-x}Nb_xO_3$. *Phys. Rev. B* **41**, 2398–2408 (1990).

[81] Pirc, R. & Blinc, R. Vogel-fulcher freezing in relaxor ferroelectrics. *Phys. Rev. B* **76**, 020101 (2007).

[82] Siny, I. G. *et al.* Raman scattering in the relaxor-type ferroelectric $Na_{0.5}Bi_{0.5}TiO_3$. *Ferroelectrics* **248**, 57–78 (2000).

[83] Siny, I. *et al.* A central peak in light scattering from the relaxor-type ferroelectric $Na_{\frac{1}{2}}Bi_{\frac{1}{2}}TiO_3$. *Physica B: Condensed Matter* **293**, 382 – 389 (2001).

[84] F.S.Chen. A laser-induced inhomogeneity of refractive indices in KTN. *Journal of Applied Physics* **38**, 3418–3420 (1967).

[85] Kogelnik, H. Coupled wave theory for thick hologram gratings. *Bell System Technical Journal* **48**, 2909–2947 (1969).

[86] Neumann, J., Röwe, M., Veenhuis, H., Pankrath, R. & Krätzig, E. Linear electrooptic coefficient r_{42} of tetragonal potassium-tantalate-niobate and barium-calcium-titanate. *Physica Status Solidi B* **215**, R9–R10 (1999).

[87] Born, M. & Wolf, E. *Principles of Optics* (Pergamon Press, 1980), sixth edn.

[88] Wemple, S. H. Optical oscillator strengths and excitation energies in solids, liquids, and molecules. *The Journal of Chemical Physics* **67**, 2151–2168 (1977).

[89] Jackson, J. D. *Classical Electrodynamics* (John Wiley & Sons, 1999), third edn.

[90] Ishai, P. B., de Oliveira, C., Ryabov, Y., Agranat, A. & Feldman, Y. Unusual glass-like systems - relaxation dynamics of Cu^+ ions in ferroelectric KTN crystals. *Journal of Non-Crystalline Solids* **351**, 2786 – 2792 (2005). Proceedings

of 3rd International Conference on Broadband Dielectric Spectroscopy and its Applications.

[91] Moharam, M. G. & Gaylord, T. K. Analysis and applications of optical diffraction by gratings. *Proceedings of the IEEE* **73**, 894–937 (1985).

[92] Yeh, P., Yariv, A. & Hong, C.-S. Electromagnetic propagation in periodic stratified media. i. general theory. *J. Opt. Soc. Am.* **67**, 423–437 (1977).

[93] Nye, J. *Physical properties of crystals, their representation by tensors and matrices.* (Clarendon Press, 1957), first edn.

[94] Zgonik, M. *et al.* Materials constants of knbo[sub 3] relevant for electro- and acousto-optics. *Journal of Applied Physics* **74**, 1287–1297 (1993).

[95] Geusic, J. *et al.* Electro-Optic Properties of Some ABO_3 Perovskites in the Paraelectric Phase. *Applied Physics Letters* **4**, 141–143 (1964).

[96] Röwe, M., Neumann, J., Krätzig, E. & Odoulov, S. Holographic scattering in photorefractive potassium tantalateniobate crystals. *Optics Communications* **170**, 121–127 (1999).

[97] Hewat, A. W. Soft modes and the structure, spontaneous polarization and curie constants of perovskite ferroelectrics: tetragonal potassium niobate. *Journal of Physics C: Solid State Physics* **6**, 1074 (1973).

[98] Knauss, L. A., Pattnaik, R. & Toulouse, J. Polarization dynamics in the mixed ferroelectric $KTa_{1-x}Nb_xO_3$. *Phys. Rev. B* **55**, 3472–3479 (1997).

[99] Samara, G. A. Nature of the phase transition in $KTaO_3$ with random site impurities. *Japanese Journal of Applied Physics* **24S2**, 80–84 (1985).

[100] Toulouse, J. & Pattnaik, R. Pretransitional condensation in mixed ferroelectrics. *Journal of Physics and Chemistry of Solids* **57**, 1473–1477 (1996).

[101] R.K.Pattnaik & Toulouse, J. Polar properties of a mesoscopic ferroelectric. *Ferroelectrics* **194**, 239–248 (1997).

[102] J. Toulouse and P. DiAntonio and B.E. Vugmeister and X.M. Wang and L.A. Knauss. Precursor effects and ferroelectric macroregions in $KTa_{1-x}Nb_xO_3$ and $K_{1-y}Li_yTaO_3$. *Phys. Rev. Lett.* **68**, 232–235 (1992).

[103] Kleemann, W., Schafer, F. J. & Rytz, D. Diffuse ferroelectric phase transition and long-range order of dilute $KTa_{1-x}Nb_xO_3$. *Phys. Rev. Lett.* **54**, 2038–2041 (1985).

[104] Bouziane, E., Fontana, M. & Kleemann, W. A study of the successive phase transitions in $KTa_{0.93}Nb_{0.07}O_3$ by light scattering, dielectric permittivity and light diffraction measurement. *Journal of Physics: Condensed Matter* **6**, 1965–1984 (1994).

[105] Bouziane, E. & Fontana, M. Precursor effects and successive phasetransitions in a dilute crystal of KTN. *Journal of Physics: Condensed matter* **9**, 10249–10260 (1997).

[106] Klink, J. V. D., Rod, S. & Chatelain, A. Local properties, long range order, and quantum ferroelectricity in $KTa_{1-x}Nb_xO_3$. *Physical Review B (Condensed Matter and Materials Physics)* **33**, 2084 – 2087 (1986).

[107] Boyd, R. W. *Nonlinear Optics* (Academic Press, 2002), second edn.

[108] Rod, S. & van der Klink, J. J. Evidence from pressure-dependent NMR for a percolative phase transition in $kta_{1-x}nb_xo_3$. *Phys. Rev. B* **49**, 15470–15474 (1994).

[109] Svitelskiy, O. & Toulouse, J. Translational and rotational mode coupling in disordered ferroelectric $KTa_{(1-x)}Nb_xO_3$ studied by Raman spectroscopy. *Journal of Physics and Chemistry of Solids* **64**, 665 – 676 (2003).

[110] Uwe, H., Lyons, K. B., Carter, H. L. & Fleury, P. A. Ferroelectric microregions and Raman scattering in $KTaO_3$. *Phys. Rev. B* **33**, 6436–6440 (1986).

[111] Svitelskiy, O. *et al.* Resonant ultrasound spectroscopy of $KTa_{1-x}Nb_xO_3$ ferroelectric relaxor crystals. *Phys. Rev. B* **78**, 064113 (2008).

[112] Guan, Q. *et al.* The influence of domain state on thermal-mechanical properties of KTN crystal. *Journal of Crystal Growth* **125**, 568–70 (1992).

[113] Gehring, P. M. *et al.* Dipole-glass behavior of lightly doped $KTa_{1-x}Nb_xO_3$. *Phys. Rev. B* **46**, 5116–5121 (1992).

[114] Huang, X. R. *et al.* Ferroelectric domain structures and phase transitions in $KTa_{1-x}Nb_xO_3$ crystals. *physica status solidi (a)* **148**, 611–618 (1995).

[115] Moharam, M. G. & Gaylord, T. K. Three-dimensional vector coupled-wave analysis of planar-grating diffraction. *J. Opt. Soc. Am.* **73**, 1105–1112 (1983).

[116] Ishai, P. B., de Oliveira, C. E. M., Ryabov, Y., Feldman, Y. & Agranat, A. J. Glass-forming liquid kinetics manifested in a KTN:Cu crystal. *Phys. Rev. B* **70**, 132104 (2004).

[117] Toulouse, J. & Pattnaik, R. K. Nonlinear electrostriction in the mixed ferroelectric $KTa_{1-x}Nb_xO_3$. *Phys. Rev. B* **65**, 024107 (2001).

[118] Wang, X. P. *et al.* Thermal properties of cubic $KTa_{1-x}Nb_xO_3$ crystals. *Journal of Applied Physics* **103**, 033513 (2008).

[119] Leyva, V., Agranat, A. & Yariv, A. Determination of the physical parameters controlling the photorefractive effect in $KTa_{1-x}Nb_xO_3$:Cu,V. *J. Opt. Soc. Am. B* **8**, 701–707 (1991).

[120] DiDomenico, M. & Wemple, S. Optical properties of perovskite oxides in their paraelectric and ferroelectric phases. *Physical Review* **166**, 565–576 (1968).

[121] Scott, J. F. Absence of true critical exponents in relaxor ferroelectrics: the case for defect dynamics. *Journal of Physics: Condensed Matter* **18**, 7123 (2006).

[122] van der Klink, J. J., Rytz, D., Borsa, F. & Höchli, U. T. Collective effects in a random-site electric dipole system: $KTaO_3$: Li. *Phys. Rev. B* **27**, 89–101 (1983).

[123] Parravicini, J., Conti, C., Agranat, A. & DelRe, E. Rejuvenation in scale-free optics and enhanced diffraction cancellation life-time. *Opt. Express* **20**, 27382–27387 (2012).

[124] Bitton, G., Razvag, M. & Agranat, A. J. Formation of metastable ferroelectric clusters in $K_{1-x}Li_xTa_{1-y}Nb_yO_3$:Cu,V at the paraelectric phase. *Phys. Rev. B* **58**, 5282–5286 (1998).

[125] Cowley, R. Structural phase transitions I. Landau theory. *Advances in Physics* **29**, 1–110 (1980).

[126] Berne, B. J. & Pecora, R. *Dynamic light scattering with applications to chemistry, biology and physics* (John Wiley & Sons, Inc., 1976), first edn.

[127] Hayes, W. & Loudon, R. *Scattering of light by crystals* (John Wiley & Sons, Inc., 1978).

[128] Reif, F. *Fundamentals of statistical and thermal physics* (McGraw-Hill Book co., 1965), first edn.

[129] Kreisel, J. *et al.* An X-ray diffraction and Raman spectroscopy investigation of A-site substituted perovskite compounds: the $(Na_{1-x}K_x)_{0.5}Bi_{0.5}TiO_3$ ($0 \leq x \leq 1$) solid solution. *Journal of Physics: Condensed Matter* **12**, 3267 (2000).

[130] Petzelt, J. *et al.* Infrared, Raman and high-frequency dielectric spectroscopy and the phase transitions in $Na_{\frac{1}{2}}Bi_{\frac{1}{2}}TiO_3$. *Journal of Physics: Condensed Matter* **16**, 2719 (2004).

[131] Yao, J. *et al.* Hierarchical domains in $Na_{\frac{1}{2}}Bi_{\frac{1}{2}}TiO_3$ single crystals: Ferroelectric phase transformations within the geometrical restrictions of a ferroelastic inheritance. *Applied Physics Letters* **96**, 222905 (2010).

[132] Dorcet, V. & Trolliard, G. A transmission electron microscopy study of the a-site disordered perovskite $Na_{0.5}Bi_{0.5}TiO_3$. *Acta Materialia* **56**, 1753 – 1761 (2008).

[133] Dorcet, V., Trolliard, G. & Boullay, P. The structural origin of the antiferroelectric properties and relaxor behavior of $Na_{\frac{1}{2}}Bi_{\frac{1}{2}}TiO_3$. *Journal of Magnetism and Magnetic Solids* **321**, 1758–61 (2009).

[134] Fateley, W. G., Dollish, F. R., McDevitt, N. T. & Bentley, F. F. *Infrared and Raman selection rules for molecular and lattice vibrations* (John Wiley & Sons, Inc., 1972).

[135] Porporati, A. A., Tsuji, K., Valant, M., Axelsson, A.-K. & Pezzotti, G. Raman tensor elements for multiferroic $BiFeO_3$ with rhombohedral R3c symmetry. *Journal of Raman Spectroscopy* **41**, 84–87 (2010).

[136] Zvirgzds, J. A., Kapostin, P. P., Zvirgzde, J. V. & Kruzina, T. V. X-ray study of phase transitions in ferroelectric $Na_{0.5}Bi_{0.5}TiO_3$. *Ferroelectrics* **40**, 75–77 (1982).

[137] Liu, Y. *et al.* Local microstructure evolution of bismuth sodium titanate-based lead-free piezoelectric systems accross the morphotropic phase boundary region. *Journal of Advanced Dielectrics* **02**, 1230012 (2012).

[138] Daniel, P., Rousseau, M. & Toulouse, J. Vibrational investigation of the antiferrodistortive structural instabilities in the perovskite crystal $RbCaF_3$. *Physical Review B* **55**, 6222–6231 (1997).

[139] Ratuszna, A. & Kachel, A. Intrinsic chaotization model for a perovskite $KMnF_3$ crystal. *Acta Crystallographica Section B* **48**, 118–122 (1992).

[140] Unoki, H. & Sakudo, T. Electron spin resonance of Fe^{3+} in $SrTiO_3$ with special reference to the 110°K phase transition. *Journal of the Physical Society of Japan* **23**, 546–552 (1967).

[141] Tu, C.-S., Siny, I. G. & Schmidt, V. H. Sequence of dielectric anomalies and high-temperature relaxation behavior in $Na_{\frac{1}{2}}Bi_{\frac{1}{2}}TiO_3$. *Phys. Rev. B* **49**, 11550–11559 (1994).

[142] Lufaso, M. W., Barnes, P. W. & Woodward, P. M. Structure prediction of ordered and disordered multiple octahedral cation perovskites using *SPuDS*. *Acta Crystallographica Section B* **62**, 397–410 (2006).

[143] Howard, C. J. & Stokes, H. T. Group-Theoretical Analysis of Octahedral Tilting in Perovskites. *Acta Crystallographica Section B* **54**, 782–789 (1998).

[144] Kreisel, J., Glazer, A. M., Bouvier, P. & Lucazeau, G. High-pressure Raman study of a relaxor ferroelectric: The $Na_{0.5}Bi_{0.5}TiO_3$ perovskite. *Phys. Rev. B* **63**, 174106 (2001).

[145] Gorfman, S. & Thomas, P. A. Evidence for a non-rhombohedral average structure in the lead-free piezoelectric material $Na_{0.5}Bi_{0.5}TiO_3$. *Journal of Applied Crystallography* **43**, 1409–1414 (2010).

[146] Aksel, E. *et al.* Monoclinic crystal structure of polycrystalline $Na_{0.5}Bi_{0.5}TiO_3$. *Applied Physics Letters* **98**, 152901 (2011).

[147] Balashova, E. V. & Tagantsev, A. K. Polarization response of crystals with structural and ferroelectric instabilities. *Phys. Rev. B* **48**, 9979–9986 (1993).

[148] Carpenter, M. A. & Salje, E. K. H. Elastic anomalies in minerals due to structural phase transitions. *European Journal of Mineralogy* **10**, 693–812 (1998).

[149] Toulouse, J. Understanding $NaBiTiO_3$ through a comparison with $KTaNbO_3$ and $KLiTaO_3$. In *Proceedings of the International Workshop on Lead-free Relaxor Ferroelectrics (IWLFF)* (2010).

[150] Isupov, V. Ferroelectric $Na_{0.5}Bi_{0.5}TiO_3$ and $K_{0.5}Bi_{0.5}TiO_3$ and their solid solutions. *Ferroelectrics* **315**, 127 (2005).

[151] Cordero, F., Craciun, F., Trequattrini, F., Mercadelli, E. & Galassi, C. Phase transitions and phase diagram of the ferroelectric perovskite $(Na_{0.5}Bi_{0.5})_{1-x}Ba_xTiO_3$ by anelastic and dielectric measurements. *Phys. Rev. B* **81**, 144124 (2010).

[152] East, J. & Sinclair, D. Characterization of $(Bi_{\frac{1}{2}}Na_{\frac{1}{2}})TiO_3$ using electric modulus spectroscopy. *Journal of Materials Science Letters* **16**, 422–425 (1997).

[153] Suchanicz, J., Roleder, K., Kwapuliński, J. & Jankowska-Sumara, I. Dielectric and structural relaxation phenomena in $Na_{0.5}Bi_{0.5}TiO_3$ single crystal. *Phase Transitions* **57**, 173–182 (1996).

[154] Garg, R., Rao, B. N., Senyshyn, A., Krishna, P. S. R. & Ranjan, R. Lead-free piezoelectric system $(Na_{0.5}Bi_{0.5})TiO_3$-$BaTiO_3$: Equilibrium structures and irreversible structural transformations driven by electric field and mechanical impact. *Phys. Rev. B* **88**, 014103 (2013).

[155] Tilak, B. Ferroelectric relaxor behavior and spectroscopic properties of Ba2+ and Zr4+ modified sodium bismuth titanate. *American Journal of Materials Science* **2**, 110–118 (2012).

[156] Zhang, M.-S., Scott, J. F. & Zvirgzds, J. A. Raman spectroscopy of $Na_{0.5}Bi_{0.5}TiO_3$. *Ferroelectrics Letters Section* **6**, 147–152 (1986).

[157] Luo, L. *et al.* Raman spectroscopic study of $Na_{\frac{1}{2}}Bi_{\frac{1}{2}}TiO_3$-x%$BaTiO_3$ single crystals as a function of temperature and composition. *Journal of Applied Physics* **109**, 113507 (2011).

[158] Niranjan, M. K., Karthik, T., Asthana, S., Pan, J. & Waghmare, U. V. Theoretical and experimental investigation of raman modes, ferroelectric and dielectric properties of relaxor na[sub 0.5]bi[sub 0.5]tio[sub 3]. *Journal of Applied Physics* **113**, 194106 (2013).

[159] Trujillo, S. *et al.* The high-pressure behaviour of Ba-doped $Na_{\frac{1}{2}}Bi_{\frac{1}{2}}TiO_3$ investigated by Raman spectroscopy. *Journal of Physics: Condensed Matter* **17**, 6587 (2005).

[160] Rout, D., Moon, K.-S., Rao, V. S. & Kang, S.-J. L. Study of the morphotropic phase boundary in the lead-free $Na_{1/2}Bi_{1/2}TiO_3$-$BaTiO_3$ system by Raman spectroscopy. *Journal of the Ceramic Society of Japan* **117**, 797–800 (2009).

[161] Fedoseev, A. I., Lushnikov, S. G., Gvasaliya, S. N., Syrnikov, P. P. & Kojima, S. Study of phase transformation dynamics in $Na_{\frac{1}{2}}Bi_{\frac{1}{2}}TiO_3$ by Mandelstam-Brillouin scattering. *Physics of the Solid State* **51**, 1399–1403 (2009).

[162] Fano, U. Effects of configuration interaction on intensities and phase shifts. *Phys. Rev.* **124**, 1866–1878 (1961).

[163] Lima, R. C. *et al.* Photoluminescence in disordered Sm-doped $PbTiO_3$: Experimental and theoretical approach. *Journal of Applied Physics* **100**, 034917 (2006).

[164] Wang, X. *et al.* Oxygen-vacancy-related high-temperature dielectric relaxation in $SrTiO_3$ ceramics. *Journal of Applied Physics* **107**, 114101 (2010).

[165] Milanez, J. *et al.* The role of oxygen vacancy in the photoluminescence property at room temperature of the $CaTiO_3$. *Journal of Applied Physics* **106**, 043526 (2009).

[166] Avramenko, V. P., Kruzina, T. V., Kudzin, A. Y. & Sokolyanskii, G. C. Peculiarities of electrophysical properties of $Na_{0.5}Bi_{0.5}TiO_3$ single crystals. *Ferroelectrics* **174**, 71–75 (1995).

[167] Siny, T. G., Smirnova, T. A. & Kruzina, T. V. Symmetry of the paraelectric phase and dynamics of phase transitions in $Na_{\frac{1}{2}}Bi_{\frac{1}{2}}TiO_3$. *Soviet Physics: Solid State* **33**, 110 (1991).

[168] Long, D. A. *The Raman Effect: A Unified Treatment of the Theory of Raman Scattering by Molecules* (John Wiley & Sons, Ltd., 2001).

[169] Fontana, A. *et al.* The Raman coupling function in disordered solids: a light and neutron scattering study on glasses of different fragility. *Journal of Physics: Condensed Matter* **19**, 205145 (2007).

[170] Kaminow, I. P. & Damen, T. C. Temperature dependence of the ferroelectric mode in KH_2PO_4. *Phys. Rev. Lett.* **20**, 1105–1108 (1968).

[171] Daniel, P., Toulouse, J. & Rousseau, M. Phase transitions in mixed disordered crystals $Rb_{1-x}K_xCaF_3$ ($0 < x < 1$) investigated by Raman spectroscopy. *The European Physical Journal Applied Physics* **5**, 33–44 (1999).

[172] Toulouse, J., Jiang, F., Svitelskiy, O., Chen, W. & Ye, Z.-G. Temperature evolution of the relaxor dynamics in $Pb(Zn)\frac{1}{3}Nb\frac{2}{3})O_3$: A critical Raman analysis. *Phys. Rev. B* **72**, 184106 (2005).

[173] Rousseau, D. L. & Porto, S. P. S. Auger-like resonant interference in Raman scattering from one- and two-phonon states of $BaTiO_3$. *Phys. Rev. Lett.* **20**, 1354–1357 (1968).

[174] Bruce, A. D., Taylor, W. & Murray, A. F. Precursor order and Raman scattering near displacive phase transitions. *Journal of Physics C: Solid State Physics* **13**, 483 (1980).

[175] Lynden-Bell, R. M. & Michel, K. H. Translation-rotation coupling, phase transitions, and elastic phenomena in orientationally disordered crystals. *Rev. Mod. Phys.* **66**, 721–762 (1994).

[176] Keeble, D. S. *et al.* Piezoelectric materials: Bifurcated polarization rotation in bismuth-based piezoelectrics. *Advanced Functional Materials* **23**, 184–184 (2013).

[177] Aksel, E. *et al.* Local atomic structure deviation from average structure of $Na_{0.5}Bi_{0.5}TiO_3$: Combined X-ray and neutron total scattering study. *Phys. Rev. B* **87**, 104113 (2013).

[178] Lockwood, D. J. & Torrie, B. H. Raman scattering study of the three structural phases of $KMnF_3$. *Journal of Physics C: Solid State Physics* **7**, 2729 (1974).

[179] Leal, S. *et al.* Ferroelectric phase transition in $Pb_{0.60}Sr_{0.40}TiO_3$ thin films. *Materials Chemistry and Physics* **87**, 353 – 356 (2004).

[180] Tenne, D. A. *et al.* Lattice dynamics in $Ba_xSr_{1-x}TiO_3$ single crystals: A Raman study. *Phys. Rev. B* **70**, 174302 (2004).

[181] Kim, T. H., Kojima, S., Park, K., Kim, S. B. & Ko, J.-H. Precursor polar clusters in the paraelectric phase of ferroelectric $Ba_{0.80}Ca_{0.20}TiO_3$ single crystals studied by Brillouin light scattering. *Journal of Physics: Condensed Matter* **22**, 225904 (2010).

[182] Burns, G. & Scott, B. A. Raman scattering in the ferroelectric system $Pb_{1-x}Ba_xTiO_3$. *Solid State Communications* **9**, 813 – 817 (1971).

[183] Taniguchi, H., Itoh, M. & Fu, D. Raman scattering study of the soft mode in $Pb(Mg_{\frac{1}{3}}Nb_{\frac{2}{3}})O_3$. *Journal of Raman Spectroscopy* **42**, 706–714 (2011).

[184] Lushnikov, F., S.G. Jiang & Kojima, S. Central peak in the vibrational spectrum of the relaxor ferroelectric lead scandotantalate. *Solid State Communications* **122**, 129–133 (2002).

[185] Toulouse, J., Vugmeister, B. E. & Pattnaik, R. Collective dynamics of off-center ions in $K_{1-x}Li_xTaO_3$: A model of relaxor behavior. *Phys. Rev. Lett.* **73**, 3467–3470 (1994).

[186] Schwabl, F. & Täuber, U. C. Defect-induced condensation and central peak at structural transitions. *Phys. Rev. B* **43**, 11112–11135 (1991).

[187] Ge, W. *et al.* Influence of dc-bias on phase stability in Mn-doped $Na_{0.5}Bi_{0.5}TiO_3$-5.6%$BaTiO_3$ single crystals. *Applied Physics Letters* **95** (2009).

[188] Yamamoto, K., Suzuki, M., Noguchi, Y. & Miyayama, M. High-performance $Bi_{0.5}Na_{0.5}TiO_3$ single crystals grown by high-oxygen-pressure flux method. *Japanese Journal of Applied Physics* **47**, 7623–7629 (2008).

[189] Babu, J. B., Madeswaran, G., Chen, X. & Dhanasekaran, R. Effect of oxygen vacancies on ferroelectric behavior of $Na_{\frac{1}{2}}Bi_{\frac{1}{2}}TiO_3$-$BaTiO_3$ single crystals. *Materials Science and Engineering: B* **156**, 36 – 41 (2009).

[190] Meng, X.-d., Wang, D.-z., Liu, J.-h. & Zhang, S.-y. Preparation and characterization of sodium titanate nanowires from brookite nanocrystallites. *Materials Research Bulletin* **39**, 2163 – 2170 (2004).

[191] Lin, S. J. *et al.* Raman scattering investigations of the low-temperature phase transition of $NaNbO_3$. *Journal of Raman Spectroscopy* **37**, 1442–1446 (2006).

[192] Sathe, V. G. & Dubey, A. Broken symmetry in $LaAlO_3$ single crystal probed by resonant Raman spectroscopy. *Journal of Physics: Condensed Matter* **19**, 382201 (2007).

[193] Ishikawa, A., Nohara, J. & Sugai, S. Raman study of the orbital-phonon coupling in $LaCoO_3$. *Phys. Rev. Lett.* **93**, 136401 (2004).

[194] Solanki, R. S. *et al.* Confirmation of the monoclinic Cc space group for the ground state phase of $Pb(Zr_{0.525}Ti_{0.475})O_3$: A combined synchrotron X-ray and neutron powder diffraction study. *Applied Physics Letters* **102**, 052903 (2013).

[195] Souza Filho, A. G. *et al.* Monoclinic phase of $PbZr_{0.52}Ti_{0.48}O_3$ ceramics: Raman and phenomenological thermodynamic studies. *Phys. Rev. B* **61**, 14283–14286 (2000).

[196] Lima, K. C. V. *et al.* Raman study of morphotropic phase boundary in $PbZr_{1-x}Ti_xO_3$ at low temperatures. *Phys. Rev. B* **63**, 184105 (2001).

[197] Prosandeev, S., Kornev, I. A. & Bellaiche, L. Phase transitions in epitaxial (-110) $BiFeO_3$ films from first principles. *Phys. Rev. Lett.* **107**, 117602 (2011).

Vita

Daniel K. Jackson was born in Buffalo, NY and graduated from the University at Buffalo, The State University of New York in 1995 with a B.S. in Social Sciences Interdisciplinary/Environmental Studies. He was a student leader with the environmental studies group, interacting with local, regional and state wide organizations. He later worked for at Houseworks for three years as a home improvement contractor site foreman before starting at the Jack J. Kolberg Co. Inc. as an inside sales representative in 1999. He sold industrial pneumatic and hydraulic equipment and converted the computer systems during the Y2K crisis to modern PC's with Businessworks software. He was promoted to outside sales in 2000 and marketed the company to the upstate NY regions. In 2002 the Kolberg Co. closed and he left to work for the Ralph A. Hiller Co Inc. of Export PA to continue his career in sales until June of 2004. He returned to school to obtain a Bachelors in physics from the University at Buffalo and went on to Lehigh University in 2007. He worked for a summer at Georgia Tech under the direction of Dr. James Gole through the NSF research experience for undergraduates (REU) Program. At Lehigh, Dan worked with Jean Toulouse on various projects involving the structural phase transitions of perovskite crystals. He gained valuable laboratory experience working with lasers, optics, Raman and dielectric spectroscopy, absorbance, luminescence and birefringence experiments. He was awarded two fellowships while at Lehigh, the Sherman-Fairchild Fellowship in Solid State Studies from 2009 to 2011 and the College of Arts and Sciences Summer Fellowship during the summer of 2012.

PRESENTATIONS AND CONFERENCES

4. Daniel K. Jackson, Radha Pattnaik, Haosu Luo, Dwight Viehland and Jean Toulouse, *Comparison of the Raman low frequency spectra of NBT and KLT*, **APS March Meeting 2011**, Dallas TX

3. Daniel K. Jackson, Radha Pattnaik, Aharon J. Agranat and Jean Toulouse

Temperature evolution of the linear birefringence in striated single crystals of $KTa_{(1-x)}Nb_xO_3$ *(KTN)*, **APS March 2012 Meeting**, Boston MA

2. Daniel K. Jackson, Radha Pattnaik, and Jean Toulouse, *Temperature evolution of the linear birefringence in striated single crystals of* $KTa_{(1-x)}Nb_xO_3$ *(KTN)*, **Ferroelectrics Workshop 2012**, Argonne National Laboratory January 30-February 2, 2012

1. Daniel K. Jackson and Jean Toulouse *Investigation of relaxations and central peaks in the Raman spectra of NBT*, **APS March Meeting 2013**, Baltimore MD, March 18-22 2013

ARTICLES IN PREPARATION

Submitted to Physical Review B: *Phonon Modes and Central Peaks in an A-site Relaxor: a comprehensive Raman study of sodium bismuth titanate.* Daniel K. Jackson, Haosu Luo, and Jean Toulouse.

Submitted to Physical Review B: *Temperature evolution of the birefringence in striated single crystals of* $KTa_{(1-x)}Nb_xO_3$ *(KTN)*, Daniel K. Jackson, Radha Pattnaik, and Jean Toulouse